UNIVERSITY OF CALIFORNIA
RIVERSIDE

Low-Cost, Label-Free Single-Walled Carbon Nanotube-Based Chemiresistive Biosensors on Paper Microfluidics for Detection of Disease Biomarkers

A Dissertation submitted in partial satisfaction
of the requirements for the degree of

Doctor of Philosophy

in

Chemical and Environmental Engineering

by

Yu Shen

December 2021

Dissertation Committee:
Dr. Ashok Mulchandani, Chairperson
Dr. Hideaki Tsutsui
Dr. Juchen Guo

The Dissertation of Yu Shen is approved:

_____

_____

_____

Committee Chairperson

University of California, Riverside

ACKNOWLEDGMENTS

The past few years have been a valuable experience in my life to pursue a Ph.D. degree at University of California Riverside. I have the deepest and sincerest appreciation and gratitude to my advisor Professor Ashok Mulchandani for his great mentorship. I am grateful for his professional, patient, and constructive feedbacks and advice on the research. He always explained the complicated concepts and research results with his solid and extensive knowledge and made it clear and understandable. He was always available for us for discussions, and he has guided and taught me on how to clarify the problem statements, design experiments, find the root-cause, analyze the results, and communicate with peers. I significantly benefited from his diligence and scientific passion to the research. Without his continuous support and motivation, my work and skills in this project would hardly be possible.

I would like to express my gratitude to my co-advisor Dr. Hideaki Tsutsui for his valuable, professional, and constructive input to my research. I greatly thank the precious cooperation opportunity with him and his clever and hard-working student Sidharth Modha on the research projects. Dr. Tsutsui has always been a great source of help for the microfluidic aspects of this research, and I have been enjoying working with him and Sidharth in the past few years. I also want to thank Dr. Juchen Guo for being a great help during my time at UCR before and after he became a member of my committee. Dr. Guo was always a nice advisor to consult with, and he has always been a great help for my research and career development.

I owe special thanks to my parents and my husband, Changxu Ren, for their unconditional, continuous, and unfailing love that supported me throughout the years during my pursuit of the Ph.D. degree. My family has always stood by me with mental companion during my hardest time. We shared the amazing journey of earning the Ph.D. degree and they have been always my best friends and the most enthusiastic cheerleaders for me.

My friends, classmates, and colleagues have been super inspiring and joyous to work with. The time spent with my dear friends and colleagues was unforgettable as it shaped me to who I am today. Thank you to Thien-Toan Huu Tran, Sidharth Modha, Mohammed Sedki, Ying Chen, Touhid Bin Anwar, Tung Pham, Gongde Chen, Guo Zhao, Jingfang Hu, Dan Yan, Mika Hadada, Kenta Nakama, Shanhui Xu, Xiaoyu Wen, Jia Jiang, Anqi Yu, Libby Xu, Le Chen, Wangxiang Li, Taifeng Wang, Claudia C Villarreal, Snow, Sara Zachariah, and Linh Nguyen for the time we spent together.

Lastly, I would like to thank the Department of Chemical and Environmental Engineering for their time and help. I would also like to thank the funding agency, the National Science Foundation, for making this research possible.

Part of this dissertation has used paragraphs, sentences, figures, and tables from the following publications:

(1) Shen, Y., Anwar, T. B., & Mulchandani, A. (2021). Current status, advances, challenges and perspectives on biosensors for COVID-19 diagnosis in resource-limited settings. *Sensors and Actuators Reports*, 100025.

(2) Sedki, M., Shen, Y., & Mulchandani, A. (2020). Nano-FET-enabled biosensors: Materials perspective and recent advances in North America. *Biosensors and Bioelectronics*, 112941.

(3) Shen, Y., Tran, T. T., Modha, S., Tsutsui, H., & Mulchandani, A. (2019). A paper-based chemiresistive biosensor employing single-walled carbon nanotubes for low-cost, point-of-care detection. *Biosensors and Bioelectronics*, **130**, 367-373.

(4) Shen, Y., Modha, S., Tsutsui, H., & Mulchandani, A. (2021). An origami electrical biosensor for multiplexed analyte detection in body fluids. *Biosensors and Bioelectronics*, **171**, 112721.

(5) Modha, S., Shen, Y., Chamouni, H., Mulchandani, A., & Tsutsui, H. (2021). Laser-etched grooves for rapid fluid delivery for a paper-based chemiresistive biosensor. *Biosensors and Bioelectronics*, **180**, 113090.

ABSTRACT OF THE DISSERTATION

Low-Cost, Label-Free Single-Walled Carbon Nanotube-Based Chemiresistive Biosensors on Paper Microfluidics for Detection of Disease Biomarkers

by

Yu Shen

Doctor of Philosophy, Graduate Program in Chemical and Environmental Engineering
University of California, Riverside, December 2021
Dr. Ashok Mulchandani, Chairperson

The affordable, rapid, sensitive, specific biosensors are critical to prompt disease diagnosis, especially in developing areas with low resources. However, traditional technologies to detect disease biomarkers such as colorimetric lateral flow assays and polymerase chain reaction tests, suffer from low sensing performance, high operation complexity, high cost, and long assay time. Therefore, it is imperative to develop an affordable biosensing platform with high sensing performances and high user-friendliness to meet the ASSURED criteria (affordable, sensitive, specific, user-friendly, rapid and robust, equipment-free, and deliverable to end-users) for diagnostic tools in resource-limited areas. Hence, this research developed the paper-based microfluidic chemiresistive biosensors employing single-walled carbon nanotubes (SWCNTs) and specific bioreceptors for the detection of important biomarkers in various biological samples.

By synthesizing the pyrene carboxylic acid (PCA) modified SWCNTs and characterizing PCA/SWCNTs, we successfully fabricate the chemiresistors via facile methods of vacuum filtration and inkjet printing. Both fabrication methods enabled the

control of PCA/SWNTs networks density on paper substrate. We optimized the biosensing performance by optimizing the sensitivity, assay time, and balanced material cost. With the final goal of developing the fully assembled devices for biomarker detections, we have also worked on the wax printing-patterned paper-based microfluidics with proper sealing materials to manipulate the microflows of samples and buffers for the controlled sample delivery during the test. We have investigated the paper-based microflows in both vertical and lateral directions and integrated with the chemiresistive biosensor arrays to achieve the fully assembled devices for the rapid and easy electrical measurements. Using the PCA/SWCNTs, specific bioreceptors, and paper-based microfluidics, the developed biosensors were able to detect important biomarkers of human serum albumin, human immunoglobin G, and micro RNAs, in various biological matrices with great sensitivity and specificity. This work shows the great potential of paper-based microfluidics chemiresistive biosensor in future applications such as medical diagnosis, environmental hazard monitoring and food safety.

TABLE OF CONTENTS

LIST OF FIGURES

LIST OF TABLES

Chapter 1. Introduction: Paper-based Diagnostic Biosensor Platforms for Affordable, Sensitive, and Rapid Detections of Biomolecules

1.1 Overview and Significance

More than 95 % of deaths in developing countries are due to major infectious diseases and cancers, of which the majority can be prevented with adequate diagnosis and treatment[1,2]. It is reported that merely 3 – 5 % of the healthcare spending will impact 70 % of the healthcare decisions[3]. Therefore, sensitive, specific, and affordable diagnostic devices are critical to achieve the prompt diagnosis of diseases at the point-of-care (POC), yet the traditional techniques, such as ELISA, western blotting, flow cytometry and polymerase chain reaction (PCR), are restrained in centralized laboratories due to their long assay time, high cost, and demanding requirement of professional instruments and personnel. Therefore, developing low-cost and POC diagnostic tools have become a prominent task for delivering the timely diagnosis and consequent medical treatment of the patients. The World Health Organization has provided a "ASSURED" criteria as a guideline for researchers that the diagnostic tools for resource-limited settings should be **a**ffordable, **s**ensitive, **s**pecific, **u**ser-friendly, **r**apid & robust, **e**quipment-free, and **d**eliverable-to-end-users[4–6].

Paper-based biosensors provide a suitable platform to meet the ASSURED criteria due to their intriguing properties: low-cost, built-in microfluidics, disposability, wide availability, and recyclability, which make paper-based biosensors easy to fabricate, distribute, and dispose of. However, the applications of colorimetric/chemiluminescence

and electrochemical paper-based sensors are limited by their poor limit of detection[7], low sensitivity[8], variation in analytical tools (for example, image capturing tools for optical biosensors) from case to case[9,10], and requirement of bulk reservoirs for the redox reactions. In addition, these biosensors often require employment of multiple antibodies and labeling techniques with complicated handling and operation, which also limits their POC uses[11].

Since the advent of the single-walled carbon nanotube (SWCNT)-based field-effect transistor (FET) biosensors, the SWCNTs have attracted tremendous attention in the biosensor research community. SWCNTs show unique physical, chemical, mechanical, and electronic properties for fabricating the FET biosensors for highly sensitive, specific, and label-free detections of biomolecules. However, the fabrication of the traditional FET biosensor on the silicon wafer relied on the use of lithographic patterning/etching, clean-room infrastructures, bulky instruments, large volumes of organics, and costly silicon wafers. These add up the cost and make it unaffordable in resource-limited situations. Furthermore, the biosensors fabricated on silicon wafer substrate were not easily disposable and were usually buried in the landfill, which could aggravate the environmental burdens[12,13]. On the other hand, there are many non-lithography methods to pattern the nano-/micro-biosensors on the paper substrates, such as microcontact printing, screen printing, flexographic printing, and inkjet printing[14–18]. Among all, the non-contact piezoelectric inkjet printing stands out due to its distinctive advantages, such as low-cost, mass fabrication, and rapid fabrication. This research focused on the development of aqueous SWCNTs ink for fabricating the highly sensitive SWCNTs FET biosensors in more cost-effective ways of filtration and printing, and their integration with controlled

paper-based microfluidics to achieve full device assembly for POC use. By fabricating and functionalizing the SWCNT-based chemiresistors (FETs without a gate electrode) and optimizing the protocols, this research investigated the low-cost fabrication of inkjet-printed FET biosensors on paper-based microfluidics and demonstrated sensitive and specific detections of protein and micro RNA biomarkers for promising application for POC diagnosis of diseases.

1.2 Scope of the Research

The goal of this research is to develop SWCNTs chemiresistive biosensors in paper-based microfluidics in a low-cost and facile manner for the affordable detection of important biomarkers for POC disease diagnosis. This research has the following aims:

Aim 1 Functionalize and characterize the SWCNTs with improved chemical properties for aqueous suspension.

Aim 2 Develop the vacuum-filtered SWCNT chemiresistive biosensors in paper-based vertical-flow microfluidics and demonstrate the detection of protein biomarker.

Aim 3 Develop the inkjet-printed SWCNT chemiresistive biosensors in 3-dimensional paper-based origami microfluidics and demonstrate the multiplexed detection of multiple protein biomarkers.

Aim 4 Develop the inkjet-printed SWCNT chemiresistive biosensors in paper-based substrate for rapid and ultrasensitive detection of micro RNA biomarkers in biological samples.

This research included various aspects of the paper-based SWCNT FET/chemiresistive biosensor development. **Aim 1** focused on the synthesis and material characterization of the SWCNT nanomaterials. The nanomaterial served as the basic semiconductor transducer in the subsequent chemiresistor fabrications. **Aim 2**, **3**, and **4** utilized the modified SWCNTs from Aim 1 to fabricate the chemiresistors with specific bioreceptors immobilized for the sensitive detections of various biomarkers. As discussed in Chapter 3, 4, and 5, mixed tactics were investigated in corporation with Dr. Hideaki Tsutsui and Sidharth Modha for designing, optimizing, and integrating the paper-based microfluidics with the SWCNT chemiresistors to achieve the fully assembled biosensor devices.

1.3 References

1. Su, W., Gao, X., Jiang, L. & Qin, J. Microfluidic platform towards point-of-care diagnostics in infectious diseases. *J. Chromatogr. A* **1377**, 13–26 (2015).

2. Yager, P. *et al.* Microfluidic diagnostic technologies for global public health. *Nature* **442**, 412 (2006).

3. Lee, W. G., Kim, Y.-G., Chung, B. G., Demirci, U. & Khademhosseini, A. Nano/Microfluidics for diagnosis of infectious diseases in developing countries. *Adv. Drug Deliv. Rev.* **62**, 449–457 (2010).

4. Drain, P. K. *et al.* Diagnostic point-of-care tests in resource-limited settings. *Lancet Infect. Dis.* **14**, 239–249 (2014).

5. Smith, S., Korvink, J. G., Mager, D. & Land, K. The potential of paper-based diagnostics to meet the ASSURED criteria. *RSC Adv.* **8**, 34012–34034 (2018).

6. Wu, G. & Zaman, M. H. Low-cost tools for diagnosing and monitoring HIV infection in low-resource settings. *Bull. World Health Organ.* **90**, 914–920 (2012).

7. Martinez, A. W., Phillips, S. T., Butte, M. J. & Whitesides, G. M. Patterned paper as a platform for inexpensive, low-volume, portable bioassays. *Angew. Chemie Int. Ed.* **46**, 1318–1320 (2007).

8. Hossain, S. M. Z. & Brennan, J. D. β-Galactosidase-based colorimetric paper sensor for determination of heavy metals. *Anal. Chem.* **83**, 8772–8778 (2011).

9. Ge, L., Wang, S., Song, X., Ge, S. & Yu, J. 3D origami-based multifunction-integrated immunodevice: Low-cost and multiplexed sandwich chemiluminescence immunoassay on microfluidic paper-based analytical device. *Lab Chip* **12**, 3150–3158 (2012).

10. Hu, J. *et al.* Advances in paper-based point-of-care diagnostics. *Biosens. Bioelectron.* **54**, 585–597 (2014).

11. Cheng, C. *et al.* Paper-based ELISA. *Angew. Chemie Int. Ed.* **49**, 4771–4774 (2010).

12. Deng, R., Chang, N. L., Ouyang, Z. & Chong, C. M. A techno-economic review of silicon photovoltaic module recycling. *Renew. Sustain. Energy Rev.* **109**, 532–550 (2019).

13. Kiddee, P., Pradhan, J. K., Mandal, S., Biswas, J. K. & Sarkar, B. An overview of treatment technologies of E-waste. *Handb. Electron. Waste Manag.* 1–18 (2020).

14. Dilfer, S., Hoffmann, R. C. & Dörsam, E. Characteristics of flexographic printed indium–zinc-oxide thin films as an active semiconductor layer in thin film field-effect transistors. *Appl. Surf. Sci.* **320**, 634–642 (2014).

15. Hambsch, M. *et al.* Uniformity of fully gravure printed organic field-effect transistors. *Mater. Sci. Eng. B* **170**, 93–98 (2010).

16. Härting, M., Zhang, J., Gamota, D. R. & Britton, D. T. Fully printed silicon field effect transistors. *Appl. Phys. Lett.* **94**, 193509 (2009).

17. Hossain, R. F. & Kaul, A. B. Inkjet-printed MoS2-based field-effect transistors with graphene and hexagonal boron nitride inks. *J. Vac. Sci. Technol. B, Nanotechnol. Microelectron. Mater. Process. Meas. Phenom.* **38**, 42206 (2020).

18. Mehlich, J., Miyata, Y., Shinohara, H. & Ravoo, B. J. Fabrication of a Carbon-Nanotube-Based Field-Effect Transistor by Microcontact Printing. *Small* **8**, 2258–2263 (2012).

Chapter 2. Review of Paper-Based Microfluidics and SWCNTs-Based Field-Effect Transistor Biosensors

The text of this chapter is based on, or in part a reprint of the material as it appears in Shen, Y., Anwar, T. B., & Mulchandani, A. (2021). Current status, advances, challenges and perspectives on biosensors for COVID-19 diagnosis in resource-limited settings. *Sensors and Actuators Reports*, 100025., Sedki, M., Shen, Y., & Mulchandani, A. (2020). Nano-FET-enabled biosensors: Materials perspective and recent advances in North America. *Biosensors and Bioelectronics*, 112941., Shen, Y., Tran, T. T., Modha, S., Tsutsui, H., & Mulchandani, A. (2019). A paper-based chemiresistive biosensor employing single-walled carbon nanotubes for low-cost, point-of-care detection. *Biosensors and Bioelectronics*, **130**, 367-373., Shen, Y., Modha, S., Tsutsui, H., & Mulchandani, A. (2021). An origami electrical biosensor for multiplexed analyte detection in body fluids. *Biosensors and Bioelectronics*, **171**, 112721., and Modha, S., Shen, Y., Chamouni, H., Mulchandani, A., & Tsutsui, H. (2021). Laser-etched grooves for rapid fluid delivery for a paper-based chemiresistive biosensor. *Biosensors and Bioelectronics*, **180**, 113090.

2.1 Abstract

Prompt diagnostic tests are becoming an essential part of the social activities. However, the expensive and time-consuming laboratory-based traditional methods do not suffice the enormous needs for massive number of tests, especially in resource-limited settings. Therefore, more affordable, rapid, sensitive, and specific field-practical diagnostic

devices meeting the ASSURED criteria would play an important role in the fight against the disease. Paper-based microfluidic biosensing devices are suitable for developing the prompt diagnostic tools. On the other hand, Field-effect transistor (FET) is a very promising platform for biosensor applications due to its magnificent properties, including label-free detection, high sensitivity, fast response, real-time measurement capability, low running power, and the feasibility to miniaturize to a portable device. SWCNTs with their unique structural and electronic properties that are unavailable in bulk materials, have helped improve the sensitivity of FET biosensors and enabled detection down to single molecule. This chapter reviews the emerging strategies for fabricating the paper-based microfluidics to manipulate the sequential delivery of microflows with valves, delays, and accelerations. Secondly, this chapter reviews the physical, chemical, and electrical properties of SWCNTs, followed by the working principles and applications of FET biosensors employing SWCNTs.

2.2 Introduction

The ideal diagnostic devices for a highly transmissible disease, such as COVID-19, demand the sensing technologies be **a**ffordable (low cost and low requirement for personnel and instrument), **s**ensitive, **s**pecific (low rates of false positives and false negatives), **r**apid (preferably in minutes or an hour), **e**quipment-free (no expensive equipment or with a portable device) and **d**eliverable (accessible to the end-users)—summarized as the ASSURED criteria[1,2] for POC use. Many efforts have been made towards developing diagnostic devices that meet the ASSURED criteria[3]. Paper-based

biosensors provide a suitable platform to meet the ASSURED criteria due to their intriguing properties: low-cost, built-in microfluidics, disposability, wide availability, and recyclability, which make paper-based biosensors easy to fabricate, distribute, and dispose of. The porous structure of paper-based materials enables the pump-free capillary transport of biological samples and buffers for the biorecognition and reaction that can be transduced to signal via optical and electrical changes. Therefore, there are numerous detection principles have employed in paper-based biosensors, such as optical/colorimetric, electro-chemiluminescent and electrochemical[4]. To achieve complicated or multiplexed detections of the paper-based biosensors, paper-based microfluidics are critical to deliver the reagents in a controlled manner. This chapter firstly reviews the recently developed strategies and tactics in paper-based microfluidics for biosensing applications. On the other hand, SWCNTs-based FET biosensor is a very promising platform for biosensor applications due to its magnificent properties, including label-free detection, high sensitivity, fast response, real-time measurement capability, low power consumption, and the feasibility to miniaturize as portable devices. This chapter reviews the characteristic properties of SWCNTs and summarizes the advantages of using SWCNTs for the FET biosensors for the sensitive and specific detection of biomarkers of interest.

2.3 Paper-Based Microfluidics

Paper is defined as the hydrophilic porous membrane made of cellulose fibers or related derivatives. Paper substrates have large surface-to-volume ratio to accommodate reagents and sensor materials. Another distinct advantage of paper-based microfluidics is the capillary action due to the micro pores in the substrate that enables the pump-free microfluidics, which have been studied in recent years to achieve vertical and lateral microflow controls of various reagents. Many patterning techniques can pattern the micro channels in paper substrate and enable the bioassays. The traditional paper-based microfluidic biosensors for POC diagnostics are dipstick assays and lateral-flow assays (LFAs) and have been reviewed elsewhere[5–7]. Here, this section focuses on the recent advancements in the microfluidic strategies in the recently developed paper-based analytical devices, especially on the applications in medical diagnostics.

2.3.1 Fabrication Methods of Paper-Based Microfluidics

Numerous methods have been developed for fabricating microfluidic features in paper-based substrates, such as paper-cutting[8,9], hydrophobic writings[10], photolithography[11], screen-printing[12], lacquer spraying with iron masks[13], vacuum filtration with metal stencils[14], inkjet printing[15,16], and wax printing[17–20]. The key to fabricate paper microfluidics is to form the hydrophobic barriers in paper substrate and thus create hydrophilic channels for channeling the microflows[21]. Each method shows unique advantages and disadvantages regarding the pattern resolutions, instrumentation requirements, compatibility of hydrophobic barriers with reagent, and cost-effectiveness.

Paper cutting is probably the most straightforward method to fabricate channels out of paper. Networks of paper channels can be fabricated using laser cutter (such as CO_2 laser cutter) or mechanical knife cutter. Since paper substrate is soft, tape, glass, and plastic materials are often used as solid support or holders for the paper channels. Paper cutting does not require complicated instruments, instead, a blade or a pair of scissors would be sufficient to make paper channels with various geometries[8,22–24].

Hydrophobic ink can be patterned to fabricate the hydrophobic barriers to form the microfluidic channels by direct plotting of the hydrophobic materials, such as PDMS polymers[25], acrylate resin[26,27], permanent marker pens[10], ballpoint pens[28], and customized inks[28,29]. Using XY plotters or direct pen drawing, hydrophobic walls can be drawn on paper substrates. By controlling the viscosity of the ink and the pressure of the plotter head, the hydrophobic material can penetrate the paper matrix and form the hydrophobic walls throughout the thickness of the substrate. However, such plotting and drawing methods are limited by the low resolutions and can be time-consuming for larger scale device fabrications.

Patterning techniques with masks, stencils, and templates enable the selective patterning of the hydrophobic and hydrophilic regions in paper substrates. Photolithography has been employed very early for fabricating paper-based microfluidics due to its high resolution and high precision[30–34]. Generally, the paper substrate is firstly coated or impregnated with negative photoresist, then followed by selective exposure to UV light with a photomask. The non-exposed photoresist is then removed by solvent washing to develop the hydrophilic patterns in paper[17,30,33,35]. This process is very similar

to the traditional photolithography for nanofabrication on silicon wafers. Fabrications of paper-based microfluidics can therefore be easily prepared with traditional photolithography equipment. However, the equipment and materials (e.g., photoresist and organic solvents) can be expensive. For those without adequate resources, the traditional photolithography can be unaffordable. Thus, customized photoresist can be prepared based on the formulation of the commercial ones to lower the materials cost, and UV light source can be simplified as a UV lamp or even sunlight[31]. Furthermore, low-cost water-based polyurethane acrylate photoresist (~ $8 per 500 grams) can be selectively cured with UV light to fabricate paper microfluidics with high resistance to many commonly used organic solvents (methanol, isopropanol, DMF, DMSO, etc.) and surfactant solutions (10 wt%, CTAB, SDS, and Triton X-100), as shown in **Figure 2.1**. This method can efficiently avoid damages to the hydrophobic barriers from solutions containing aggressive components[36]. Although photolithographic methods provide high pattern resolution, they are still more expensive, complicated, and laborious than the printing methods.

Plasma etching have been employed for fabricating paper microfluidics by firstly coating or impregnated with hydrophobic materials such as octadecyltrichlorosilane (OTS) and alkyl ketene dimer (AKD)[37–39], followed by selective etching to ctrate the hydrophobic patterns in paper. Chemical vapor deposition (CVD) can also selectively deposit hydrophobic materials on paper through a mask[40–43]. For instance, with a metal mask placed on the paper substrate, radical monomer of the hydrophobic polymer, such as dichloro-[2,2]-paracyclophane, can be evaporated to pattern the paper. Then the local polymerization occurs in paper to fabricate the hydrophobic barriers[40].

Unlike masks, stamping methods can pattern the paper by direct stamping transfer (contact printing) of the hydrophobic materials[44–47]. The hydrophobic ink patterned on paper form the microfluidic barriers through drying, cooling or curing, depending on the ink properties. Rubber stamps can transfer the hydrophobic materials, such as liquid PDMS polymer and indelible ink, by contact-printing on the chromatography paper or filter paper[48,49]. For example, the solution of PDMS and hexane was patterned on paper by ~ 30-second contact and cured at 70 ˚C for 30 min to form the hydrophobic barriers (**Figure 2.2**). The resolutions of the hydrophobic barriers and hydrophilic channels were optimized down to 949 ± 88 μm and 771 ± 90 μm, respectively[49]. Other stamps include flash foam stamp[47], atom stamp[46], heated PCB stamp for paraffin[50], heated metal stamps for wax[51] and parafilm[45]. Stamping methods are easy and rapid to perform. The stamps are low-cost and can be customized for every pattern. However, the pattern resolution is usually poor compared to the photolithographic methods, mask-assisted methods, and printing methods. Moreover, the hydrophobic ink formulation is critical to avoid blurring of the pattern before cured.

Printing technologies, such as flexographic printing, wax printing, inkjet printing, and screen printing, are emerging techniques for patterning paper with hydrophobic barriers. Flexographic printing is a contact-printing that uses roll-to-roll set-ups to transfer the pattern from one roll to the other[52,53]. For example, polystyrene in toluene is a hydrophobic ink for flexographic printing[54]. This technique is simple and low-cost, but not practical for most lab settings since it requires the set-up of the roll-to-roll instruments and the print units. Screen printing squeezes the hydrophobic ink or wax over a mask or a

stencil to let the hydrophobic material selectively deposit on the paper substrate[12]. Recently, there have been many screen-printed microfluidic patterns on paper for biosensing developed and have been reported widely[12,55–59]. Screen printing is low-cost, fast, and compatible with many inks, including wax[12], water-based[60–62] and organic inks[62,63], yet the mask or stencil needs to be updated for every new pattern. As shown in **Figure 2.3**, wax printing uses the solid wax ink in wax printers by melting the wax as liquid for wax droplets deposition on paper[20,64–66]. The wax droplets deposit on the surface of paper and cool down as solid wax circles. To form the hydrophobic barriers, the wax droplets need to be re-melted (usually > 120 ˚C) to penetrate the paper thickness[64,67–69]. Wax printing is fast, simple, and cost-effective. However, since the re-melting process allows wax to wick both laterally and vertically in paper, the pattern resolution can be compromised and must be considered during the design process. Inkjet printing is another useful method to pattern the microfluidics in paper[70–72]. By replacing the regular ink with polymer solution, solvents, or other hydrophobic solutions, the inkjet printing performs the non-contact deposition of picoliter-sized ink droplets in a user-defined manner (**Figure 2.4**). Commercial inkjet printers can be adapted with user-defined inks for printing the microfluidic pattern in paper[70,73,74]. Unlike photolithography and stamping, which expose the entire substrate to the photoresist, inkjet printing is maskless, cost-effective, adaptable-for-mass fabrication, and simple. Another advantage of inkjet printing is that other reagents can also be patterned on paper to achieve the remaining biosensing functions. Therefore, the inkjet-printing is promising for simple and fast fabrication of the biosensing devices. However, the user-

defined ink needs to be carefully optimized with proper fluidic properties to be compatible with the printing process[71].

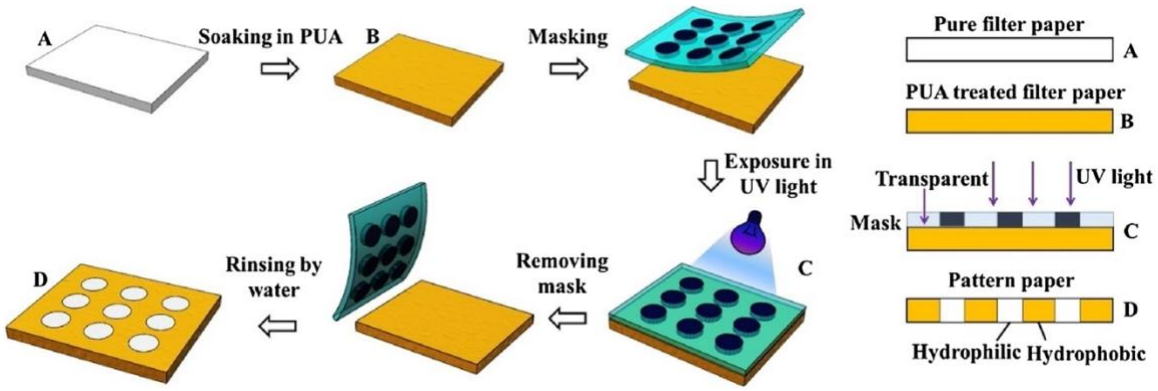

Figure 2.1 Photolithography method to fabricate patterns on paper substrate using water-based polyurethane acrylate (PUA) through UV light curing. Adapted with permission from Lin et al.[36]

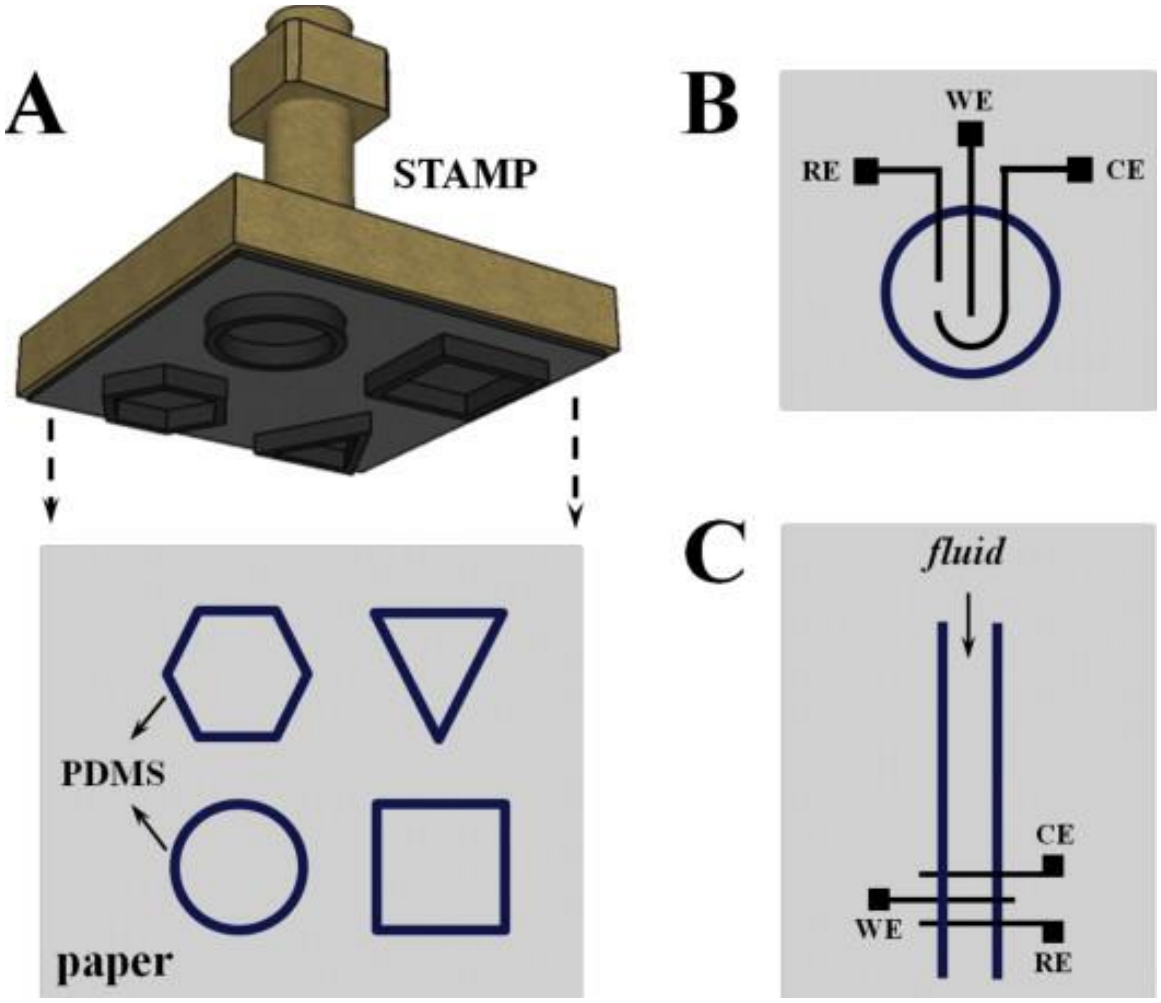

Figure 2.2 Stamping method to fabricate microfluidic patterns on paper. (A) Schematic representation of the contact-printing method for fabricating μPADs with PDMS as hydrophobic barriers. (B) Paper-based electrochemical device (PED) with pencil-drawn electrodes utilized in cyclic voltammetry experiments. (C) PED with fluidic channel with pencil-drawn electrodes utilized in flow injection analysis with amperometric detection. Adapted with permission Dornelas et al.[49]

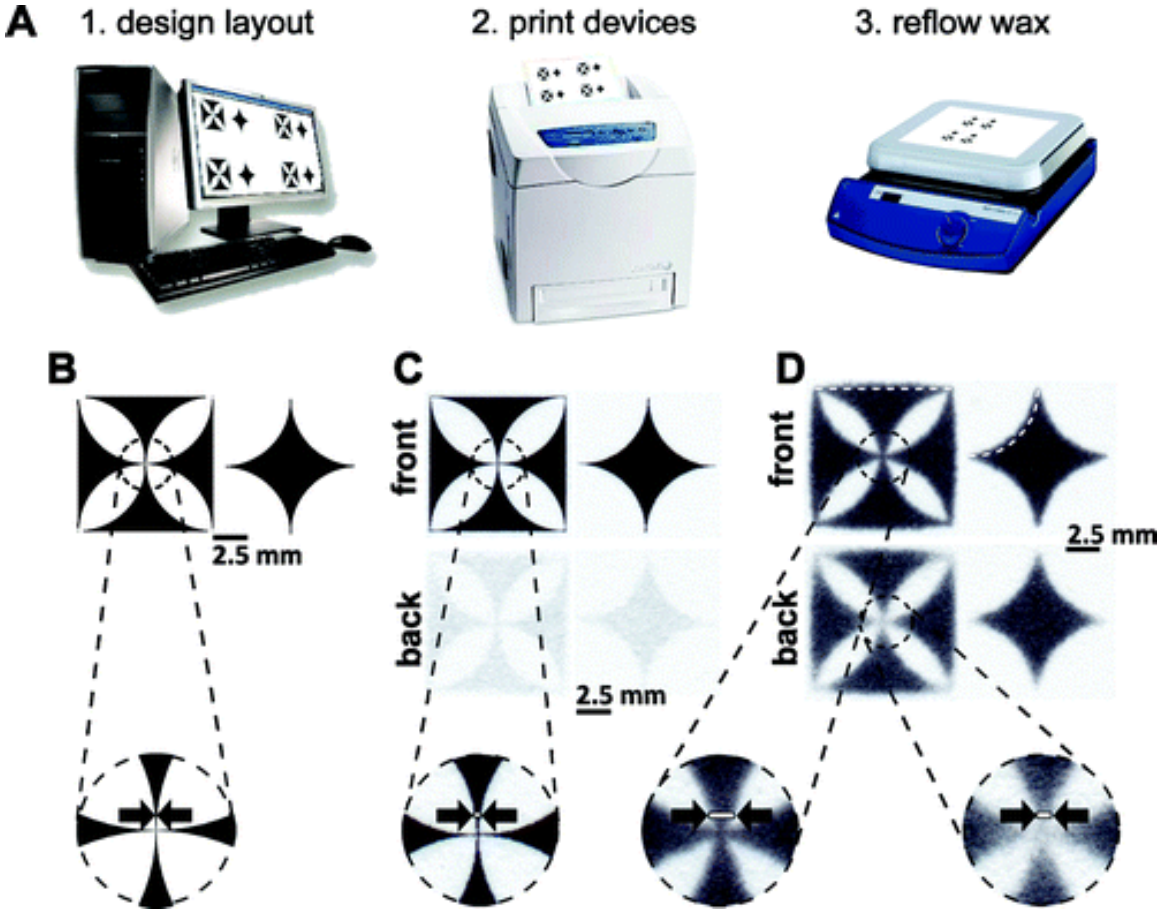

Figure 2.3 Wax printing method to fabricate hydrophobic wax patterns on paper. Adapted with permission from Carrilho et al.[64]

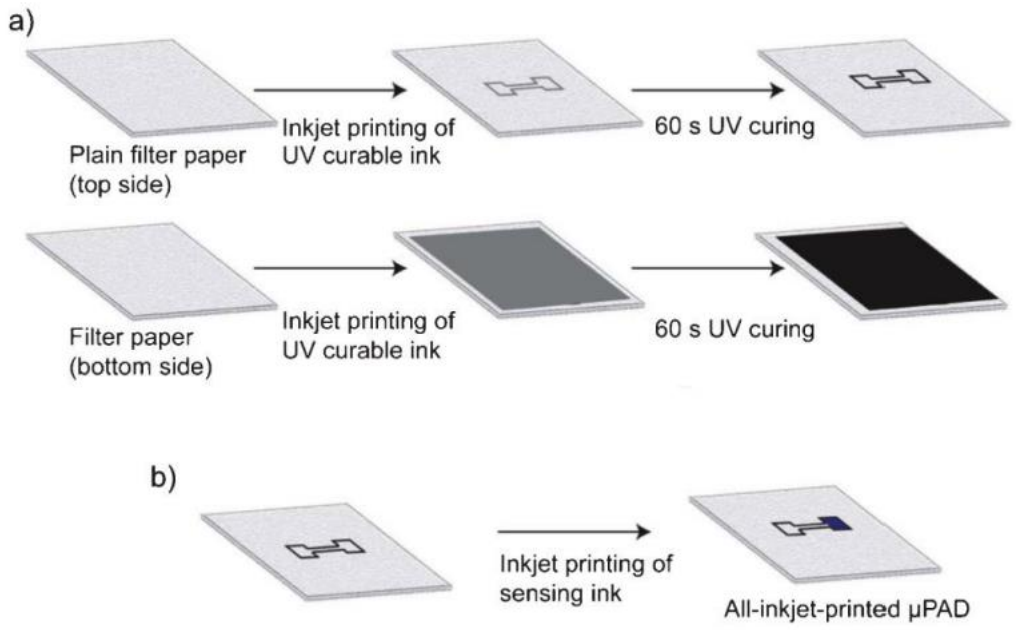

Figure 2.4 Inkjet printing method to fabricate hydrophilic channels on paper. (a) patterning of the filter paper by a double-sided printing process (grey and black colours indicate the printed hydrophobic features before and after UV curing, respectively); (b) inkjet printing of H_2O_2 sensing ink. Adapted with permission from Maejima et al.[70]

2.3.2 Strategies for Controlled Microfluidics for Paper-Based Biosensing Platform

By using various technologies to pattern the paper-based microfluidics, fluid transport in lateral and vertical flow can be achieved. In fact, controlling the capillary wicking in paper channels are critical to deliver complicated microfluidic functions for the paper-based biosensing device. Common functions include sample transportation, incubation, splitting, mixing, dilution, and washing. Therefore, this section reviews the recent developments in the methods to control the capillary wicking in paper-based microfluidic biosensors. The modeling of the paper-based microfluidics are reported and reviewed elsewhere[75–79].

Sample transportation occurs in paper mainly due to the capillary action driving force. In porous paper substrate, fluid flow usually follows the Washburn equation. It shows the distance travelled by the fluid is proportional to the square root of time and is dependent on the channel width and temperature:

$$l = \sqrt{\frac{\gamma \cos\theta}{2\eta} rt}$$

where l is the fluid travel distance, γ is the surface tension of the fluid, θ is the contact angle, η is the viscosity of the fluid, r is the average pore radius, and t is the time[80,81]. To control the fluid wicking in paper, the simplest methods are to select a paper with different pore sizes and porosities or change the dimensions of the channel (e.g., channel length, width, and depth)[82]. Other minor parameters also affect the fluid wicking in paper, such as surrounding temperature and humidity[82]. However, most of the paper-based microfluidics biosensors in research maintain a constant ambient environment during the test. Therefore, these parameters usually have minor effect on the fluid wicking in paper.

To develop the sequential and timed microfluidics, fluid valve, delay, and acceleration have been reported. Valves in paper microfluidics decide the direction and the timing of the flow by turning "on" or "off" the channel[83]. The working principle is to connect multiple channel segments or separate channels into several. The tactics usually involve the use of folding/unfolding, temporary barriers, fluid diodes, and dissolvable bridges to control the fluidic valves[84–93]. For example, Fu et al. reported a smart fluid manipulation using shape-memory-polymer (SMP) actuated fluid valves for multi-step ELISA immunoassays. The actuation of the valve was controlled by the thermally

responsive, duel-state shape transformation of SMP attached to the root of paper cantilever beam to turn on/off the channels[86]. In addition, as shown in **Figure 2.5**, Chen et al. developed a wax valve near the incubation reservoir to stop the flow of sample into the hydrophilic channel for the incubation. After the reaction was complete, a manual organic solvent drop casting (0.1 μL toluene or isopropanol) can open the valve by dissolving wax in seconds. The wax valve was employed for the distance-based detection for potassium iodate and glucose[84]. Other surfactant-dissolvable, and therefore disposable, valves employ surfactants to overcome the hydrophobic barriers. For instance, a fluid valve employed pre-deposit surfactants right before the wax barriers. After the fluid reached and dissolved the surfactants, it penetrated the wax barriers due to reduced surface tension. By controlling the amount of pre-deposited surfactants, various delays for minutes in various directions can be controlled for multiplexed biosensing such as a competitive ELISA[94]. As shown in **Figure 2.6**, another interesting fluidic diode was developed for sequential delivery of liquid samples. The valve was fabricated by creating "virtual walls" based on the UV-activated "click chemistry" between vinyl-terminated trichlorosilane primed paper fibers and the hydroxyl-terminated thiol to form the hydrophilic pattern in paper. Tween-20 was pre-deposited as the surfactants to be dissolved by the sample for overcoming the hydrophobic barriers (i.e., opening the valve). By integrating the fluidic diodes with a delay valve, complicated fluidic circuit can be fabricated for enzymatic bioassays for alkaline phosphate[87].

In addition to valve systems, delay, and accelerations of fluids in paper are critical to achieve sequential and multiplexed microfluidics[83,89,92,95–99]. For instance, as shown in

Figure 2.7, Toley et al. developed a method to delay the flow through a porous channel by diverting the fluid into an absorbent pad (paper shunt) parallel to the microfluidic channels. The capillary force and fluidic resistance can be tuned by varying its length and thickness to achieve a range of delay time from 3 to 20 minutes. This method does not require additional chemicals or patterning tool and is therefore more compatible to the biological components in the downstream sensing process. However, due to the extra fluidic path into the paper shunt, assays with small sample volume may suffer from loss of the reagents[96]. Additionally, wax pillars have been employed on a lateral flow assay to delay lateral flows as well as introduce pseudo turbulences into the microcapillary flow. The wax pillars printed in paper act as delay barriers due to their hydrophobic nature and improved the sensitivity for detecting HIgG by three folds compared to conventional lateral flow assays[97]. Another strategy to delay the fluid flow in paper is to incorporate dissolvable barriers in the channel. Sugars have been added to the paper-based channels as dissolvable barriers to slow the capillary flow. For instance, by dipping the paper channels into stock sucrose solutions with different concentrations and drying, sugar barriers with various delaying time can be fabricated. The aqueous flow front dissolved the barrier at different rates to achieve different delays[98]. Another strategy is to fabricate sugar bridges of sucrose, trehalose, and mannose to manipulate fluid volume in paper-based devices. By controlling the sugar materials and the bridge dimensions, the shut-off volume can be tuned from 10 to 80 μL[92].

Accelerations are also important in the fabrication of paper-based microfluidics. Manipulations of channel width and length are reported to slow down or speed up the

microflows in paper[95]. For instance, the downstream channel with increasing cross-sectional area of pores can increase the capillary force and stabilize the flow velocity[100]. The geometry-based manipulation of microflow velocity is straightforward but only useful for small accelerations. For larger accelerations, other methods have been developed such as laser-etching modification[85], enclosing paper channels[101,102], macro-capillary[102], and open channels in paper[103–105]. According to the Washburn equation, for the paper microfluidics with constant channel dimensions, only two parameters are available for variation: the effective pore size and the contact angle. Since the contact angle of the wetted channel very close, or taken as, zero, it leaves the modification of effective pore size as the most promising option to accelerate the microflow[85]. For instance, laser-etching is an effective tool to quantitatively remove the cellulose-based paper fibers to introduce higher microflow rates. As shown in **Figure 2.8**, Kalish et al. reported a laser-etching method of uniformly etching the surface of the paper to increase the effective pore size of the paper. By optimizing the gray scale of the design, the etching resulted in the desired wicking in paper. With sealing of the channels in packing tapes, the etched channel achieved thirteen fold faster wicking than the unmodified[85]. Laser-etching is also useful to create micro-capillary (grooves) in paper. Modha et al. recently reported the use of laser-etched grooves to accelerate the microflows. With optimized groove design (etching speed, groove pitch, and groove width) with proper tape sealing, the microfluidics were able to deliver the sample and wash sequentially[102]. Open channels in paper microfluidics can largely accelerate the microfluids since they behave as straight capillary channels with less fluidic resistance compared to the tortuous fibrous network of the unmodified paper[102–105]. Giokas

et al. created razor-crafted narrow trenches in the paper-based substrate to provide additional microflow pathways. Trenches parallel or perpendicular to the direction of flow can accelerate or delay the microflow, respectively[103]. Another open channel in paper was developed by Glavan et al., in which the blade was used to create the slits. With the remaining paper components treated to be omni-phobic, the open channel had hydrophobic walls which retained its permeability and mechanical properties. This method is inexpensive with cardstock and a craft-cutter, however, since the modified paper channel became omni-phobic, it requires an external syringe pump to drive the flow, which may cancel the benefit of the capillary action and may not be suitable for low-resource settings[105]. In addition, enclosing paper channels can also increase the flow rate by reducing evaporation[101] and increasing contact surfaces between fluid and channel[102]. For instance, Jahanshahi-Anbuhi et al. developed a sandwiched porous channel with flexible films to support the fluid flow in the channel space. This method can increase the flow rate by tenfold than the unmodified one[106].

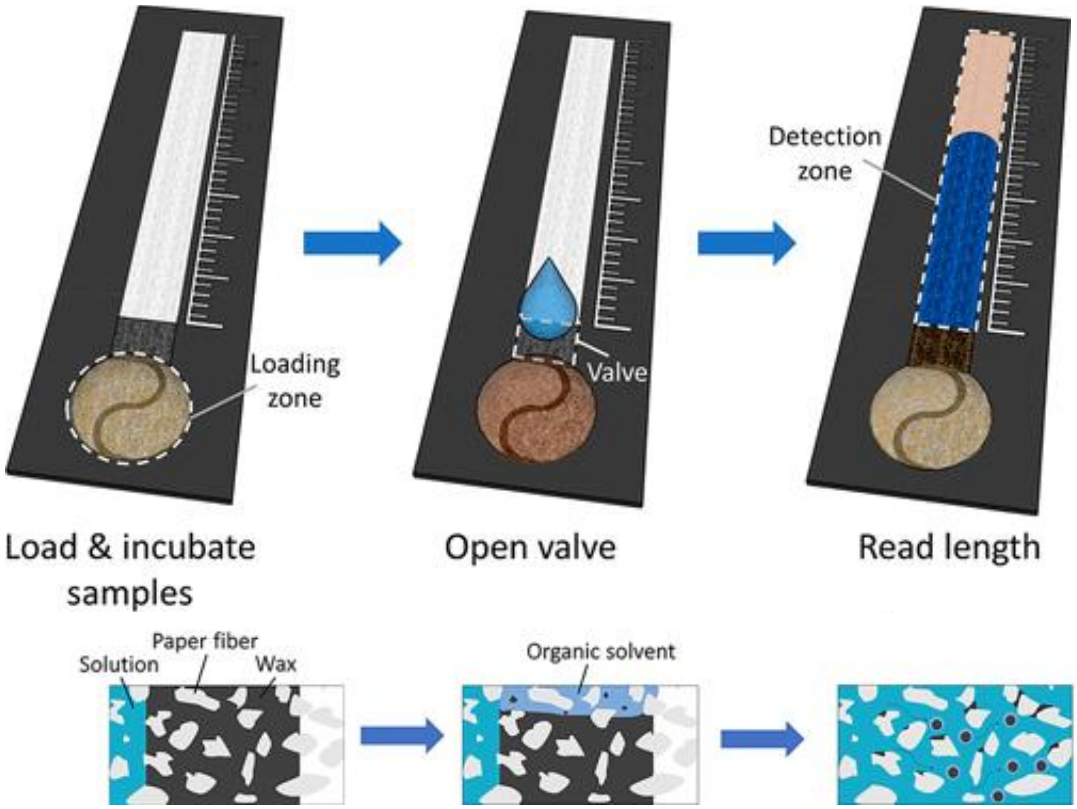

Figure 2.5 Working principle of wax valves (cross-section) in paper-based microfluidics. Liquid solution is retained inside the loading zone by the wax valve. After introduction of solvents, the wax is dissolved, and the solution can flow. Adapted with permission from Chen et al.[84]

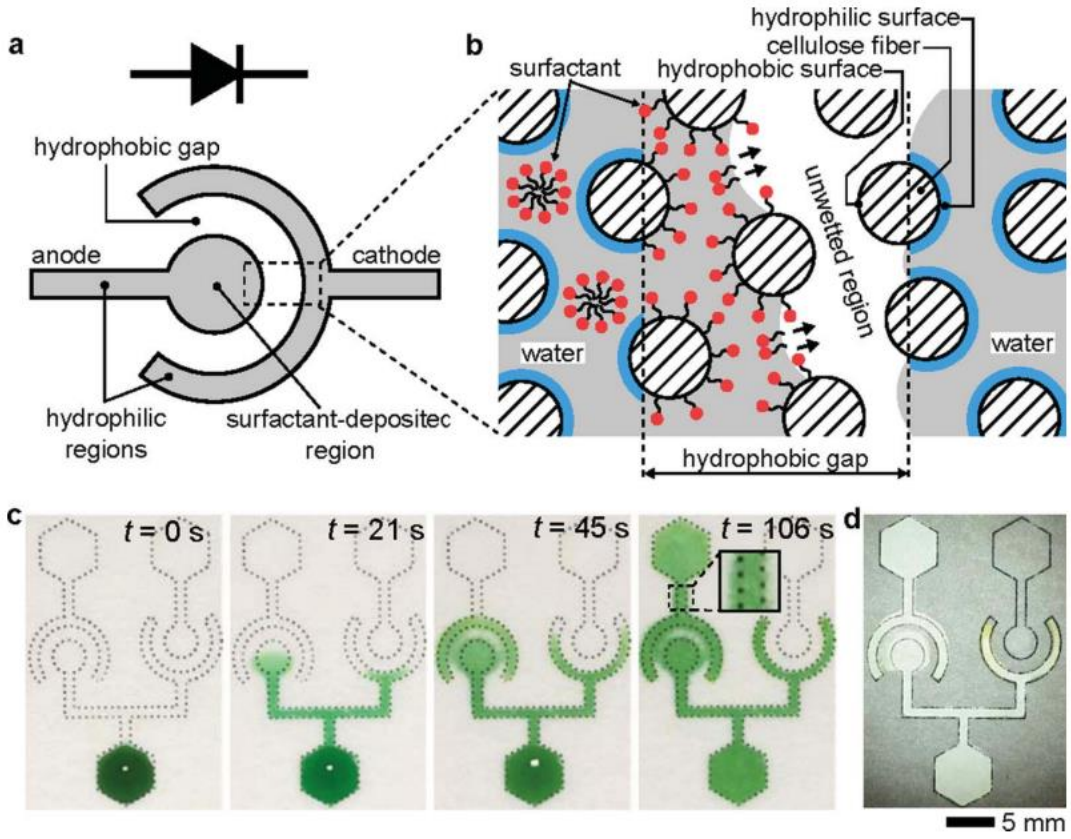

Figure 2.6 A fluid diode in paper-based microfluidics to control the valve and delay of the microflows. (a) Symbol and schematic of a single-use fluidic diode. (b) Microscopic schematic (enlarged from the dashed area in (a) illustrating the working mechanism of the fluidic diode. Arrows close to the water–air interface indicate the proceeding of the meniscus. (c) Time-sequential photographs showing the fluid (green) wicking towards two oppositely-configured diodes. d Photograph of the regulation of human blood serum by the diodes. Dotted lines or solid lines were printed on paper to highlight hydrophilic regions. Inset is the image enlarged from the dashed area. Adapted with permission from Chen et al.[87]

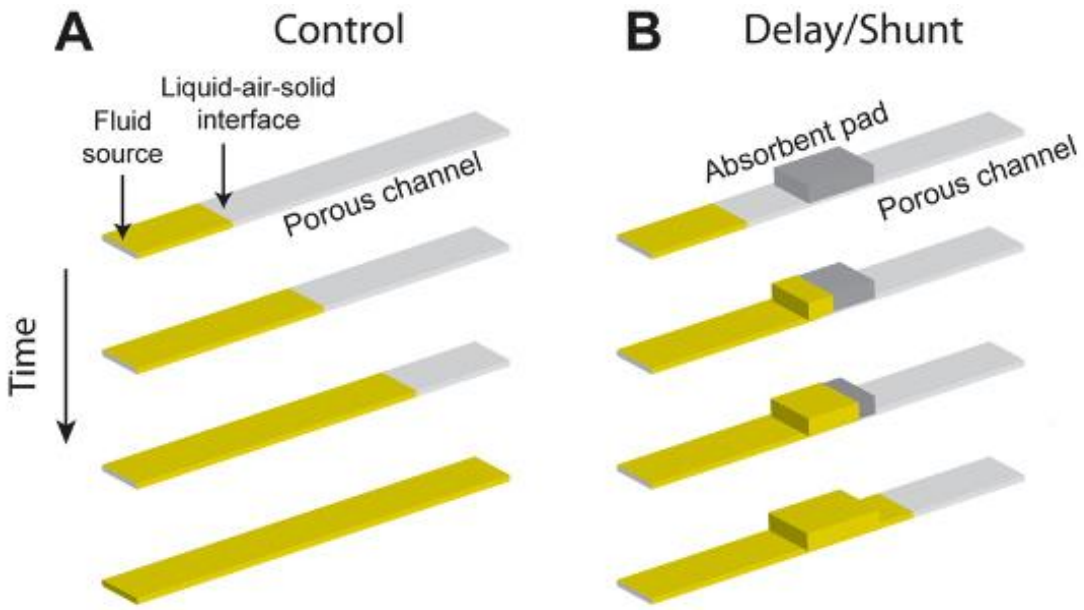

Figure 2.7 A tunable paper shunt to delay the microflows in paper. Delays using absorbent pads as shunts: concept and electrical circuit analogy: (A,B) flow of fluid through a channel of a porous membrane in the absence (control; A) and in the presence (B) of a shunt. Adapted with permission from Toley et al.[96]

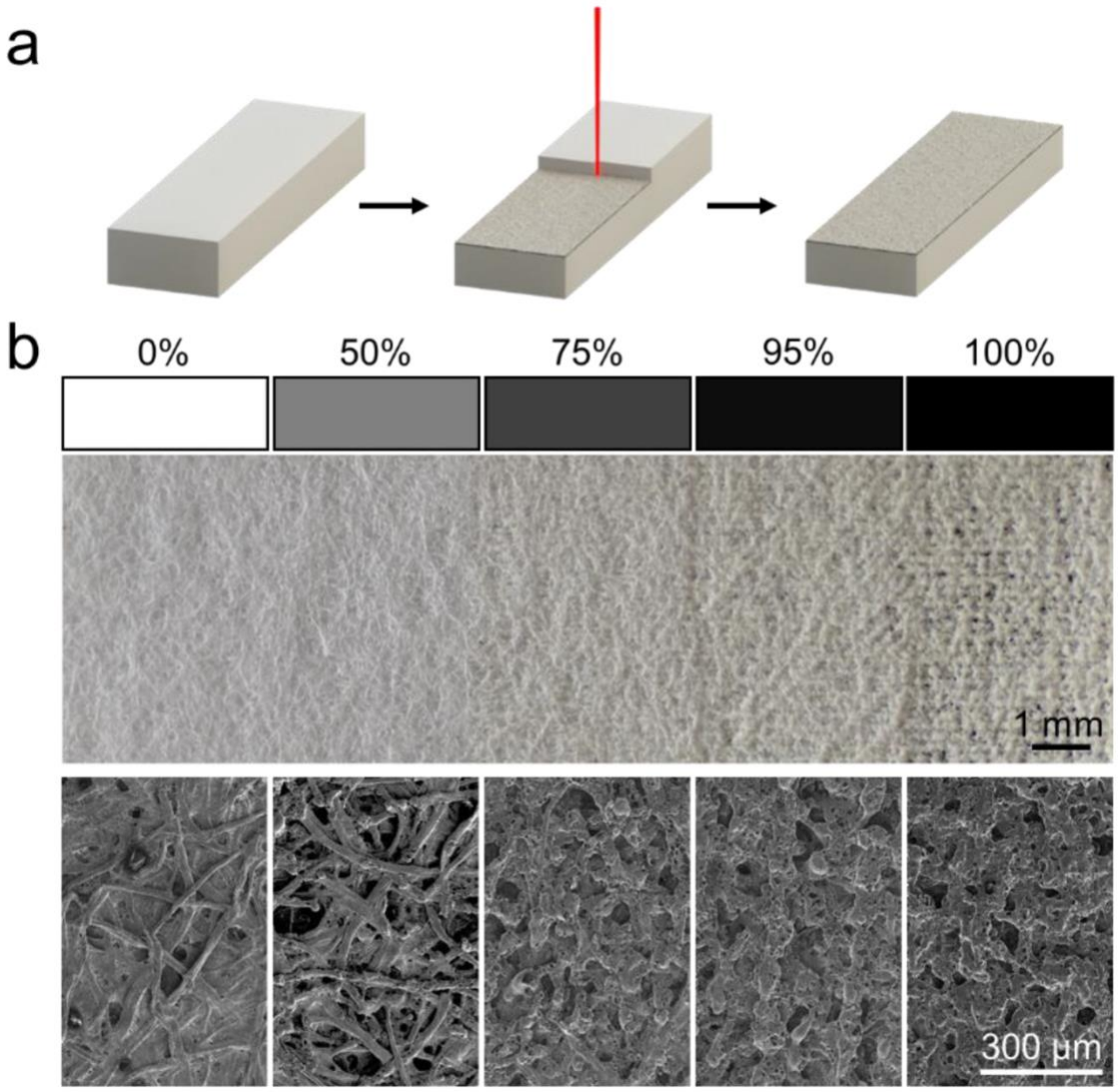

Figure 2.8 Laser etching-modified paper for modified wicking speed in paper-based microfluidics. (a) Schematic of the etching process. The etching process removes material from the top surface the paper. (b) Macro and SEM images of the etched paper surface. At the macro level, surface modification is not visible until 75%, but even at 50%, it is apparent that material has been removed from the surface in the SEM images. Adapted with permission from Kalish et al.[85]

2.4 Single-Walled Carbon Nanotube-Based Field-Effect Transistor Biosensors

2.4.1 Carbon Nanotubes

Carbon nanotubes (CNTs) can be regarded as one or more graphene sheets that are "rolled-up" into seamless tubes of nanometer diameter and are divided into single-walled carbon nanotubes (SWCNTs) and multi-walled carbon nanotubes (MWCNTs). In graphite, sp^2 hybridization occurred in the x-y plane where each carbon atom is connected to three carbons at 120˚ with a bond length of 1.42 Å; whereas the π-bond exist in the z axis with free electrons moving in the P_z orbital to give high conductivity. Similarly, the concentric layers of CNTs have an interlayer spacings of ~ 3.4 Å (close to the that of graphite: 3.35 Å)[107,108]. As shown in **Figure 2.9a**, the different rolling angles result in different chirality of SWCNTs: two vectors ($n \underset{a_1}{\rightarrow}$ and $m \underset{a_2}{\rightarrow}$) describe the chirality of CNTs based on the orientation of the tube axis versus the hexagonal lattice: chiral (n≠m), armchair (n = m), and zigzag (m = 0). The electronic properties of CNTs are governed by their structures (i.e., the chiral indices). The different structures of CNTs results in different electronic properties due to the quantum confinements of electrons in the radial direction between CNTs. Depending on chiral indices, the electronic structures of the CNTs can be metallic (n-m = 3k, where k is an integer) or semiconducting (n-m≠3k). MWCNTs are usually considered as metallic since they are highly prone to have at least one metallic shell (**Figure 2.9b**)[109]. The typical diameter of SWCNTs is in nanometers. For MWCNTs, the typical inner diameter is sub-nm to a few nanometers, while the outer diameter varies from 2 to 30 nm[110]. The length of CNTs varies from 100 nm to a few centimeters[111]. Therefore, CNTs have a very high aspect ratio and expose large surface areas (50 – 1315 m^2/g) to the

environment[112]. Other superior physical properties include high electrical conductivity (~ 10^7 S/m), high thermal conductivity (~3500 W/mK), ampacity up to 10^{13} A/m^2, and high elastic modulus (> 1 Tpa)[113]. Taken together, these interesting properties make CNTs a very suitable nanomaterial for building nano-FETs.

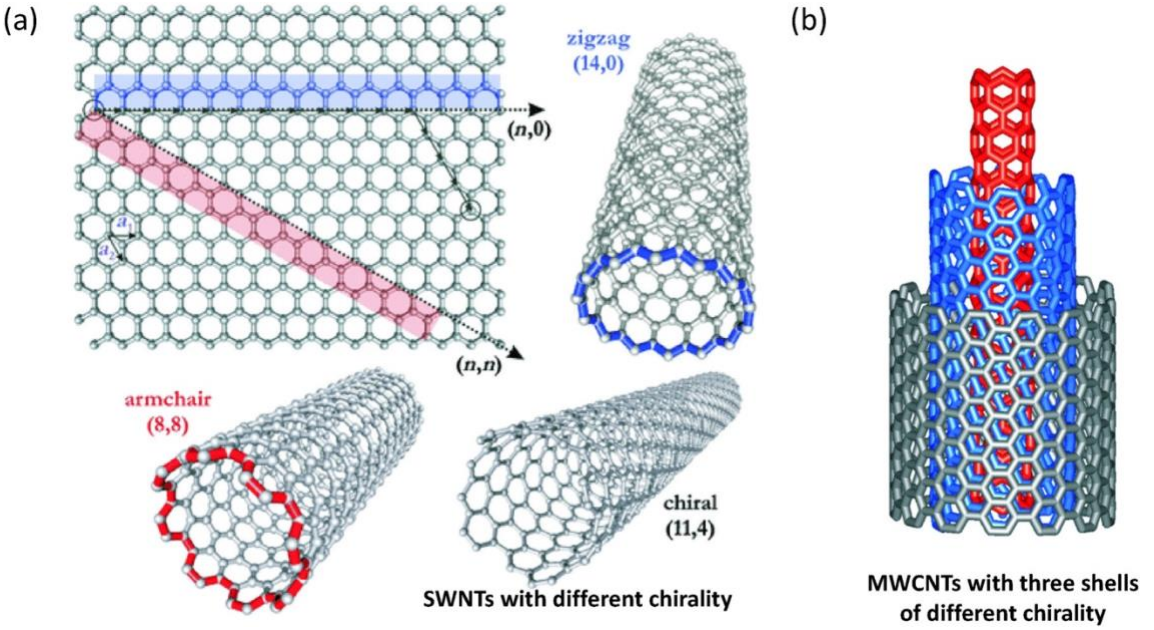

Figure 2.9 Structure of CNTs with various chirality. (a) Molecular models of SWCNTs exhibiting different chirality: armchair, zig-zag, and chiral conformations. (b) Structure of an MWCNT made up of three shells of differing chirality. Adapted with permission from Balasubramanian and Burghard[114].

2.4.2 Fabrication and Functionalization of Carbon Nanotubes

Common methods of CNTs production include arc-discharge (AD), laser ablation (LA), and chemical vapor deposition (CVD). AD was first reported by Iijima in 1991 and is one of the most widely used methods to grow CNTs[115] AD requires a high temperature (> 1700 ˚C) and utilizes metal catalysts between high-purity graphite electrodes in a pressurized chamber with evaporated carbon molecules. Currents pass through the chamber during arching as the carbon deposits at the cathode tip and chamber wall to form

carbon soot. SWCNTs and MWCNTs are synthesized in the inner core of the soot. The proper choices of catalyst precursor-graphite mixture enhance the selective yield of SWCNTs, such as Ni–Y-graphite mixtures[110]. However, AD has less control on the purity and uniformity of the CNTs. Thus, it requires further purifications, which uses strong acids that may shorten CNT length and introduce more surface defects and eventually affect the electronic properties[116]. LA was first introduced as an alternative to the AD[117]. It uses a high-power laser to vaporize the graphite at high temperature (1200 ˚C). Similar to AD, LA requires metal catalysts, such as cobalt and nickel. LA method produces CNTs with high purity and quality, how- ever, the high energy consumption and expensive instrument limit its commercialization. The CVD method uses a metal catalyst, usually nickel or cobalt. In a CVD method, a carbon-containing gas, such as ethylene or acetylene, and a carrier gas, such as nitrogen, are loaded to the reactor, where the silicon substrate is templated with implantation for CNTs growth. The carbon-containing gas is believed to be broken into carbon atoms at the surface of the catalyst to generate CNTs[118]. CVD has gained more popularity for high-volume production with high structural control at lower temperature (< 800 ˚C), although with more defects than AD and LA production. However, CVD is advantageous in allowing direct CNTs growth on substrates and mass production that requires low cost and simple instrument[119]. The as-synthesized CNTs are usually mixtures of carbonaceous impurities, metal catalysts, semiconducting and metallic CNTs with varying dimensions and morphologies, which require further purification before their use in FET biosensors. Typically, the purification involves the removal of bulk graphite particles and aggregates by harsh treatments, dissolution of metal catalysts, removal of

carbon clusters, and separation of semi-metallic and metallic CNTs. In addition, to avoid CNT bundle formation due to the van der Waals (vdW) forces, chemical oxidation, surfactants, and sonication are employed to suspend CNTs in solution. The Hersam group employed density gradient ultracentrifugation for separating SWCNTs on the basis of diameter, electrical property, (n, m) structures, enantiomer sorting and even handedness[120–123]. Purified CNTs, such as purified semiconducting SWCNTs, show superior properties suitable for FET biosensors, including high field-effect mobility, high intrinsic carrier mobility, and high on/off ratios[116,124].

2.4.3 Working Principles of Field-Effect Transistor Biosensors

Figure 2.10a depicts the simplest configuration of the FET biosensors that have three electrodes: a source, a drain, and a top/liquid-ion gate electrode. FET biosensors can be top/liquid-, back-, or double-gated. The source- drain conductance of the semiconducting channel can be switched on or off by the gate electrode[125]. For instance, applying a positive gate voltage on a p-type semiconductor leads to a depletion of carriers and a decrease in conductance, whereas a negative gate voltage leads to an accumulation of carriers and an increase in conductance[126]. On the other hand, chemiresistor bio- sensors are a variation of FETs in which the physical gate is replaced with the modulation due to charge adsorbed on the transducer surface. The charged analytes recognized by the bioreceptors near the surface of the semiconductor directly interact with the transducer and impact its electrical characteristics. Electrostatic gating, modulation in carrier mobility, changes in gate coupling and Schottky barrier effects are potential mechanisms for the

sensor response. Based on a systematic analysis of each of these mechanisms in the case of SWCNT-based FET biosensors, Heller et al. concluded electrostatic gating effect and Schottky barrier modulation were the two dominant mechanisms (**Figure 2.10b**). Electrostatic gating refers to the effect that the charges of adsorbed analytes produce upon adsorption on a semiconductor leading to a horizontal shift of the transfer curve (I_{SD}-V_G) due to the Fermi level shifting. Differently, Schottky barrier modulation refers to electrical changes brought by the adsorption of analytes at the contact region between the metal source/drain electrodes and semiconductor, which modulates the metal work function and thus the band alignment. Consequently, the current/resistance of the semiconductor is influenced. Since the Schottky barrier heights changes in opposite direction for different charge carriers, i.e., holes (p) and electron (n), the Schottky barrier modulation can be observed by the asymmetric change in the slope of the p- and n-branches of the transfer curve[127,128].

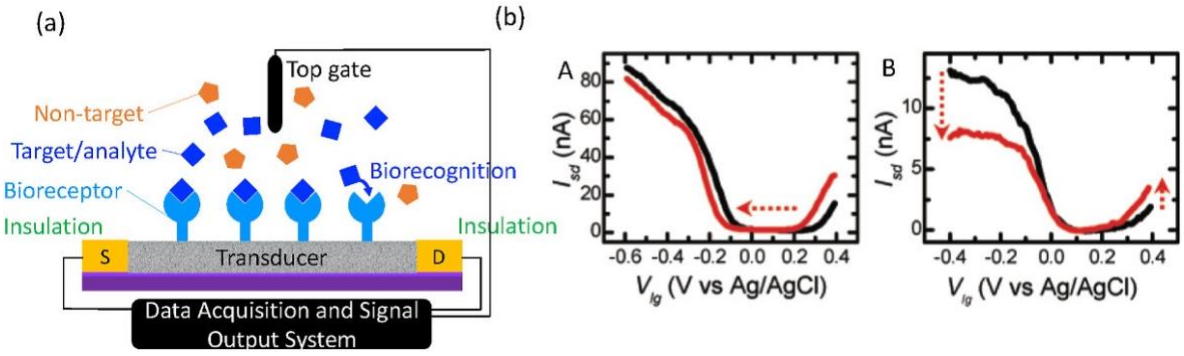

Figure 2.10 Schematic diagrams of the FET biosensors structure, functionalization strategies and mechanism (not to scale). (a) A schematic illustration of the top-gated FET biosensor structure. (b) Modulation of SWCNT-FET transfer curve due to (A) electrostatic gating and (B) Schottky barrier effect. Adapted with permission from Heller et al.[127]

2.4.4 Biofunctionalization and Applications to SWCNT-Based FET Biosensors

SWCNTs can be functionalized with bioreceptors via different functional groups (carboxyl, hydroxyl, aldehyde, amine, thiol, etc.). Bioreceptors can bind to SWCNTs through covalent bonding by targeting the C–C bonds of SWCNTs using 1,3 dipolar cycloaddition of azomethine ylide. SWCNTs containing carboxyl groups can be directly bonded to the bioreceptor using carbodiimide crosslinking chemistry[129,130]. In addition, non-covalent aromatic-like linker functionalization includes wrapping with surfactant[131–133], polymer[134–137] and DNA[138,139]. In addition, direct adsorption is also employed for straightforward functionalization[140,141]. Among all, the non-covalent functionalization of linkers on SWCNTs is of a great interest since it does not introduce defects and maintains their electrical and mechanical properties, while providing active moieties for bioconjugation[142–144].

The fabrication of SWCNT-based FET biosensors evolves from single SWCNT patterning between source and drain electrodes[145], to dielectrophoretic aligning on pre-fabricated microelectrodes[146], to self-assembled monolayer of SWCNT network on pre-fabricated microelectrodes[116,147], and bulk deposition of SWCNT networks by vacuum filtration, screen printing, and inkjet printing[14,65,148–150]. Furthermore, SWCNT-based composites with metal nanoparticles are drawing attention in the FET biosensors community[151,152]. **Table 2.1** summarized the development of employing SWCNTs in FET biosensors in North America in the past decade. These ultrasensitive and selective FET biosensors based on functionalized SWCNTs have been widely applied to various

scenarios, such as disease diagnosis, environmental monitoring, food safety, and agriculture.

CNTs	Bioreceptor	Analyte	LOD	Linker	Ref.
Single SWCNT	Antibody	Horse radish peroxide	~ 10^{-6} mol/L	Linker-free adsorption	[141]
SWCNTs	Antibodies	*E. coli O157:H7* and bacteriophage T7	10^5 CFU-*E. coli O157:H7*/mL; 10^2 PFU-T7 phage/mL	PBASE	[153]
SWCNTs	Oligonucleotide probe-anti-ATP aptamer hybrid	ATP	1 pM	PBASE	[154]
SWCNTs	Porphyrin-based glycoconjugates	Lectins (PA-IL, PA-IIL and Concanavalin A)	2 nM	Linker-free adsorption	[155]
SWCNTs	Antibody	Cortisol	0.11 pg/mL	1-Pyrenemethylamine hydrochloride	[146]
DNA/SWCNT NWs	DNA probe	DNA	10 fM	Covalent bond with SWCNTs	[156]
CNTs	Antibody fragment	Prostate cancer biomarker OPN	30 pM	Covalent bond with SWCNTs	[157]
CNTs	DNA probe	E. coli *O157* DNA	1 pg/mL	Covalent thiolation	[158]
SWCNTs	Antibody	Lyme flagellar antigen	0.1 ng/mL	Covalent bond with SWCNTs	[159]

SWCNTs/ GO	Biotin	Avidin	-	AuNP decoration	[160]
SWCNTs	MicroRNA probe	miRNA-122a	1 aM	PBASE	[161]
AuNP decorated SWCNTs	Pyrene-biotin	CaptAvidin	-	Pyrene-biotin	[162]
SWCNTs	Antibody	Microcystin-L	0.6 ng/L	PBASE	[163]
SWCNTs	polyT:polyA duplex	Salivary mercury	1 nM	PBASE	[164]
SWCNTs	Heparin	Dengue virus	8.4×10^2 $TCID_{50}$/mL	1-Pyrenemethylamine	[165]
SWCNTs	Dodecanethiol lipoic acid	Murine tissue cells	-	AuNP decoration	[152]
SWCNTs	Concanavalin A lectin	*Escherichia coli K12*, *Enterococcus faecalis*, *Streptococcus mutans*, and *Salmonella typh*	4.7×10^3 cfu/mL, 25 cfu/mL, 7.4×10^4 cfu/mL, and 6.3×10^2 cfu/mL, respectively.	PBASE	[166]
SWCNTs	Antibody	Dengur virus NS1 protein	1 ng/mL	PBASE	[167]
SWCNTs	Calmodulin	Ca^{2+}	10^{-15} M	AuNP decoration	[151]
SWCNTs	SocA	Fructosyl valine	1.2 nM	PBASE	[168]
SWCNTs	Antibody	Human serum albumin	1 pM	1-pyrene carboxylic acid	[65]

SWCNTs	red blood cell membrane	Broad-Spectrum Hemolytic Toxins; acterial Whole Secreted Proteins	fM range	Linker-free adsorption	[140]
SWCNTs	Antibody	Huanglongbing biomarker SDE1	5 nM	PBASE	[169]

Table 2.1 Summary of recently developed CNT-based FET biosensors by North American institutes since 2010.

2.5 Conclusions

Tremendous efforts have been made to both fields of research for paper-based microfluidics and SWCNT-based FET biosensors. As reviewed in the previous examples, designs and fabrications of paper-based microfluidics can manipulate the microfluids to achieve complicated sensing functions for the detections of biomolecules. Challenges exist for paper-based microfluidic biosensors. One of the major challenges is the inherent variability of paper substrate that introduces intrinsic errors in the applications. For instance, the porous structures of paper fibers are different from inch to inch, which means the pattern precision of the hydrophobic barriers can vary and affect the wicking property of the microfluidics, which can influence the assay quality. Paper with more uniform porosity may overcome this challenge. Another limiting factor is the coffee ring effect that the droplets of solution on paper tend to accumulate more solute near the stain circumference after solution dries out. Such uneven distribution of materials can be potentially overcome by employing surfactants, optimizing test zone dimensions, and optimizing drying process, etc. Nevertheless, paper-based microfluidics still shows great potential in the diagnostic devices and healthcare industry. The recent pandemic events, such as COVID-19, has

strengthened the importance and increasing need for the rapid, affordable, sensitive, and specific diagnostic tools for easy disease diagnosis, and paper-based biosensing devices can fulfill the needs.

SWCNTs with the nanometer-scale diameters show high aspect ratios, and have 1D quantum confinement, hence the charge carriers do not shunt around the interaction zone, leading to significantly larger depletion/accumulation of the charge carriers deep into the entire 1D semiconductor, compared to the planar sensors[126]. SWCNTs have been materials of choice in FET biosensors, due to their high current switching characteristics (on/off ratio), high surface-to-volume ratio and similarity of λ_D to the sensing material's diameter[169]. Furthermore, SWCNTs have fascinating physicochemical properties of tunable conductivity, from insulative to exceptionally conductive, high thermal and chemical stability, and the ease to immobilize bioreceptors, as well as their high surface area and high current on/off ratio. However, there are some limitations in the application of these 1D SWCNTs nanomaterials to FET biosensors, such as inconsistent contacts with S-D electrodes, the difficulty to get pure conductive or semiconductive SWCNTs instead of getting a mixture of semiconductive/conductive SWCNTs that impacts their electronic properties, as well as their low carrier mobility[170]. In summary, the tremendous progress in the field of SWCNTs has helped develop FET biosensors for label-free sensing with higher sensitivity and lower limits of detection, down to a single molecule. The enhancement in FET sensor sensitivity can be attributed to the unique structural, physicochemical, and electronic properties of SWCNTs materials (e.g., ultrahigh surface areas, high on/off ratios, and high carrier mobilities).

2.6 References

1. Kosack, C. S., Page, A.-L. & Klatser, P. R. A guide to aid the selection of diagnostic tests. *Bull. World Health Organ.* **95**, 639–645 (2017).

2. Mabey, D., Peeling, R. W., Ustianowski, A. & Perkins, M. D. Diagnostics for the developing world. *Nat. Rev. Microbiol.* **2**, 231–240 (2004).

3. Smith, S., Korvink, J. G., Mager, D. & Land, K. The potential of paper-based diagnostics to meet the ASSURED criteria. *RSC Adv.* **8**, 34012–34034 (2018).

4. Nery, E. W. & Kubota, L. T. Sensing approaches on paper-based devices: a review. *Anal. Bioanal. Chem.* **405**, 7573–7595 (2013).

5. Nishat, S., Jafry, A. T., Martinez, A. W. & Awan, F. R. Paper-based microfluidics: simplified fabrication and assay methods. *Sensors Actuators B Chem.* 129681 (2021).

6. Carrell, C. *et al.* Beyond the lateral flow assay: A review of paper-based microfluidics. *Microelectron. Eng.* **206**, 45–54 (2019).

7. Li, X., Ballerini, D. R. & Shen, W. A perspective on paper-based microfluidics: Current status and future trends. *Biomicrofluidics* **6**, 11301 (2012).

8. Thuo, M. M. *et al.* Fabrication of low-cost paper-based microfluidic devices by embossing or cut-and-stack methods. *Chem. Mater.* **26**, 4230–4237 (2014).

9. Mahmud, M., Blondeel, E. J. M., Kaddoura, M. & MacDonald, B. D. Features in microfluidic paper-based devices made by laser cutting: How small can they be? *Micromachines* **9**, 220 (2018).

10. Gallibu, C., Gallibu, C., Avoundjian, A. & Gomez, F. A. Easily fabricated microfluidic devices using permanent marker inks for enzyme assays. *Micromachines* **7**, 6 (2016).

11. Martinez, A. W., Phillips, S. T., Whitesides, G. M. & Carrilho, E. Diagnostics for the developing world: microfluidic paper-based analytical devices. *Anal. Chem.* **82**, 3–10 (2009).

12. Dungchai, W., Chailapakul, O. & Henry, C. S. A low-cost, simple, and rapid fabrication method for paper-based microfluidics using wax screen-printing. *Analyst* **136**, 77–82 (2011).

13. Nurak, T., Praphairaksit, N. & Chailapakul, O. Fabrication of paper-based devices by lacquer spraying method for the determination of nickel (II) ion in waste water. *Talanta* **114**, 291–296 (2013).

14. Lei, K. F., Yang, S.-I., Tsai, S.-W. & Hsu, H.-T. Paper-based microfluidic sensing device for label-free immunoassay demonstrated by biotin–avidin binding interaction. *Talanta* **134**, 264–270 (2015).

15. Abe, K., Suzuki, K. & Citterio, D. Inkjet-printed microfluidic multianalyte chemical sensing paper. *Anal. Chem.* **80**, 6928–6934 (2008).

16. Tortorich, R., Shamkhalichenar, H. & Choi, J.-W. Inkjet-Printed and Paper-Based Electrochemical Sensors. *Appl. Sci.* **8**, 288 (2018).

17. Martinez, A. W., Phillips, S. T. & Whitesides, G. M. Three-dimensional microfluidic devices fabricated in layered paper and tape. *Proc. Natl. Acad. Sci.* **105**, 19606–19611 (2008).

18. Tenda, K. *et al.* High-resolution microfluidic paper-based analytical devices for sub-microliter sample analysis. *Micromachines* **7**, 80 (2016).

19. Martinez, A. W. Microfluidic paper-based analytical devices: from POCKET to paper-based ELISA. *Bioanalysis* **3**, 2589–2592 (2011).

20. Lu, Y., Shi, W., Qin, J. & Lin, B. Fabrication and characterization of paper-based microfluidics prepared in nitrocellulose membrane by wax printing. *Anal. Chem.* **82**, 329–335 (2009).

21. Jeong, S.-G., Ganguly, R. & Lee, C.-S. Novel Materials and Fabrication Techniques for Paper-Based Devices. in *Paper-Based Medical Diagnostic Devices* 41–68 (Springer, 2021).

22. Mahmud, M. A., Blondeel, E. J. M., Kaddoura, M. & MacDonald, B. D. Creating compact and microscale features in paper-based devices by laser cutting. *Analyst* **141**, 6449–6454 (2016).

23. Nie, J. *et al.* One-step patterning of hollow microstructures in paper by laser cutting to create microfluidic analytical devices. *Analyst* **138**, 671–676 (2013).

24. Fenton, E. M., Mascarenas, M. R., López, G. P. & Sibbett, S. S. Multiplex lateral-flow test strips fabricated by two-dimensional shaping. *ACS Appl. Mater. Interfaces* **1**, 124–129 (2009).

25. Bruzewicz, D. A., Reches, M. & Whitesides, G. M. Low-cost printing of poly (dimethylsiloxane) barriers to define microchannels in paper. *Anal. Chem.* **80**, 3387–3392 (2008).

26. Sousa, L. R., Duarte, L. C. & Coltro, W. K. T. Instrument-free fabrication of microfluidic paper-based analytical devices through 3D pen drawing. *Sensors Actuators B Chem.* **312**, 128018 (2020).

27. Aguilar, L. G., Petroni, J. M., Ferreira, V. S. & Lucca, B. G. Easy and rapid pen-on-paper protocol for fabrication of paper analytical devices using inexpensive acrylate-based plastic welding repair kit. *Talanta* **219**, 121246 (2020).

28. Oyola-Reynoso, S. *et al.* Draw your assay: Fabrication of low-cost paper-based diagnostic and multi-well test zones by drawing on a paper. *Talanta* **144**, 289–293 (2015).

29. Nuchtavorn, N. & Macka, M. A novel highly flexible, simple, rapid and low-cost fabrication tool for paper-based microfluidic devices (μPADs) using technical drawing pens and in-house formulated aqueous inks. *Anal. Chim. Acta* **919**, 70–77 (2016).

30. Martinez, A. W., Phillips, S. T., Butte, M. J. & Whitesides, G. M. Patterned paper as a platform for inexpensive, low-volume, portable bioassays. *Angew. Chemie Int. Ed.* **46**, 1318–1320 (2007).

31. Martinez, A. W., Phillips, S. T., Wiley, B. J., Gupta, M. & Whitesides, G. M. FLASH: a rapid method for prototyping paper-based microfluidic devices. *Lab Chip* **8**, 2146–2150 (2008).

32. OuYang, L., Wang, C., Du, F., Zheng, T. & Liang, H. Electrochromatographic separations of multi-component metal complexes on a microfluidic paper-based device with a simplified photolithography. *RSC Adv.* **4**, 1093–1101 (2014).

33. He, Q., Ma, C., Hu, X. & Chen, H. Method for fabrication of paper-based microfluidic devices by alkylsilane self-assembling and UV/O3-patterning. *Anal. Chem.* **85**, 1327–1331 (2013).

34. He, Y., Wu, W. & Fu, J. Rapid fabrication of paper-based microfluidic analytical devices with desktop stereolithography 3D printer. *Rsc Adv.* **5**, 2694–2701 (2015).

35. Asano, H. & Shiraishi, Y. Development of paper-based microfluidic analytical device for iron assay using photomask printed with 3D printer for fabrication of hydrophilic and hydrophobic zones on paper by photolithography. *Anal. Chim. Acta* **883**, 55–60 (2015).

36. Lin, D. *et al.* Low cost fabrication of microfluidic paper-based analytical devices with water-based polyurethane acrylate and their application for bacterial detection. *Sensors Actuators B Chem.* **303**, 127213 (2020).

37. Li, X., Tian, J., Nguyen, T. & Shen, W. Paper-based microfluidic devices by plasma treatment. *Anal. Chem.* **80**, 9131–9134 (2008).

38. He, Y., Wu, Y., Fu, J.-Z. & Wu, W.-B. Fabrication of paper-based microfluidic analysis devices: a review. *Rsc Adv.* **5**, 78109–78127 (2015).

39. Kao, P.-K. & Hsu, C.-C. One-step rapid fabrication of paper-based microfluidic devices using fluorocarbon plasma polymerization. *Microfluid. Nanofluidics* **16**, 811–818 (2014).

40. Demirel, G. & Babur, E. Vapor-phase deposition of polymers as a simple and versatile technique to generate paper-based microfluidic platforms for bioassay applications. *Analyst* **139**, 2326–2331 (2014).

41. Kwong, P. & Gupta, M. Vapor phase deposition of functional polymers onto paper-based microfluidic devices for advanced unit operations. *Anal. Chem.* **84**, 10129–10135 (2012).

42. Haller, P. D., Flowers, C. A. & Gupta, M. Three-dimensional patterning of porous materials using vapor phase polymerization. *Soft Matter* **7**, 2428–2432 (2011).

43. Lam, T., Devadhasan, J. P., Howse, R. & Kim, J. A chemically patterned microfluidic paper-based analytical device (C-µPAD) for point-of-care diagnostics. *Sci. Rep.* **7**, 1–10 (2017).

44. Curto, V. F. *et al.* Fast prototyping of paper-based microfluidic devices by contact stamping using indelible ink. *Rsc Adv.* **3**, 18811–18816 (2013).

45. de Tarso Garcia, P., Cardoso, T. M. G., Garcia, C. D., Carrilho, E. & Coltro, W. K. T. A handheld stamping process to fabricate microfluidic paper-based analytical devices with chemically modified surface for clinical assays. *Rsc Adv.* **4**, 37637–37644 (2014).

46. Guan, Y. & Sun, B. Detection and extraction of heavy metal ions using paper-based analytical devices fabricated via atom stamp printing. *Microsystems Nanoeng.* **6**, 1–12 (2020).

47. He, Y., Wu, Y., Xiao, X., Fu, J. & Xue, G. A low-cost and rapid microfluidic paper-based analytical device fabrication method: flash foam stamp lithography. *RSC Adv.* **4**, 63860–63865 (2014).

48. Mathaweesansurn, A. *et al.* Simple and fast fabrication of microfluidic paper-based analytical device by contact stamping for multiple-point standard addition assay: Application to direct analysis of urinary creatinine. *Talanta* **210**, 120675 (2020).

49. Dornelas, K. L., Dossi, N. & Piccin, E. A simple method for patterning poly (dimethylsiloxane) barriers in paper using contact-printing with low-cost rubber stamps. *Anal. Chim. Acta* **858**, 82–90 (2015).

50. Zhang, A. & Zha, Y. Fabrication of paper-based microfluidic device using printed circuit technology. *Aip Adv.* **2**, 22171 (2012).

51. Zhang, Y. *et al.* Equipment-Free Quantitative Measurement for Microfluidic Paper-Based Analytical Devices Fabricated Using the Principles of Movable-Type Printing. *Anal. Chem.* **86**, 2005–2012 (2014).

52. Gonzalez-Macia, L., Morrin, A., Smyth, M. R. & Killard, A. J. Advanced printing and deposition methodologies for the fabrication of biosensors and biodevices. *Analyst* **135**, 845–867 (2010).

53. Ihalainen, P., Määttänen, A. & Sandler, N. Printing technologies for biomolecule and cell-based applications. *Int. J. Pharm.* **494**, 585–592 (2015).

54. Olkkonen, J., Lehtinen, K. & Erho, T. Flexographically printed fluidic structures in paper. *Anal. Chem.* **82**, 10246–10250 (2010).

55. Dungchai, W., Chailapakul, O. & Henry, C. S. Electrochemical detection for paper-based microfluidics. *Anal. Chem.* **81**, 5821–5826 (2009).

56. Lamas-Ardisana, P. J., Martínez-Paredes, G., Añorga, L. & Grande, H. J. Glucose biosensor based on disposable electrochemical paper-based transducers fully fabricated by screen-printing. *Biosens. Bioelectron.* **109**, 8–12 (2018).

57. Lamas-Ardisana, P. J. *et al.* Disposable electrochemical paper-based devices fully fabricated by screen-printing technique. *Electrochem. commun.* **75**, 25–28 (2017).

58. Sameenoi, Y., Nongkai, P. N., Nouanthavong, S., Henry, C. S. & Nacapricha, D. One-step polymer screen-printing for microfluidic paper-based analytical device (μPAD) fabrication. *Analyst* **139**, 6580–6588 (2014).

59. Liu, M., Zhang, C. & Liu, F. Understanding wax screen-printing: a novel patterning process for microfluidic cloth-based analytical devices. *Anal. Chim. Acta* **891**, 234–246 (2015).

60. Hughes, G., Pemberton, R. M., Nicholas, P. & Hart, J. P. Fabrication of Miniaturised Screen-printed Glucose Biosensors, Using a Water-based Ink, and the Evaluation of their Electrochemical Behaviour. *Electroanalysis* **30**, 1616–1620 (2018).

61. Pemberton, R. M., Pittson, R., Biddle, N. & Hart, J. P. Fabrication of microband glucose biosensors using a screen-printing water-based carbon ink and their application in serum analysis. *Biosens. Bioelectron.* **24**, 1246–1252 (2009).

62. Sitanurak, J. *et al.* T-shirt ink for one-step screen-printing of hydrophobic barriers for 2D-and 3D-microfluidic paper-based analytical devices. *Talanta* **205**, 120113 (2019).

63. Sun, J.-Y., Cheng, C.-M. & Liao, Y.-C. Screen printed paper-based diagnostic devices with polymeric inks. *Anal. Sci.* **31**, 145–151 (2015).

64. Carrilho, E., Martinez, A. W. & Whitesides, G. M. Understanding wax printing: a simple micropatterning process for paper-based microfluidics. *Anal. Chem.* **81**, 7091–7095 (2009).

65. Shen, Y., Tran, T.-T., Modha, S., Tsutsui, H. & Mulchandani, A. A paper-based chemiresistive biosensor employing single-walled carbon nanotubes for low-cost, point-of-care detection. *Biosens. Bioelectron.* **130**, 367–373 (2019).

66. Shen, Y., Modha, S., Tsutsui, H. & Mulchandani, A. An origami electrical biosensor for multiplexed analyte detection in body fluids. *Biosens. Bioelectron.* **171**, 112721 (2021).

67. Songjaroen, T., Dungchai, W., Chailapakul, O. & Laiwattanapaisal, W. Novel, simple and low-cost alternative method for fabrication of paper-based microfluidics by wax dipping. *Talanta* **85**, 2587–2593 (2011).

68. Lu, Y., Shi, W., Jiang, L., Qin, J. & Lin, B. Rapid prototyping of paper-based microfluidics with wax for low-cost, portable bioassay. *Electrophoresis* **30**, 1497–1500 (2009).

69. Altundemir, S., Uguz, A. K. & Ulgen, K. A review on wax printed microfluidic paper-based devices for international health. *Biomicrofluidics* **11**, 41501 (2017).

70. Maejima, K., Tomikawa, S., Suzuki, K. & Citterio, D. Inkjet printing: an integrated and green chemical approach to microfluidic paper-based analytical devices. *RSC Adv.* **3**, 9258–9263 (2013).

71. Yamada, K., Henares, T. G., Suzuki, K. & Citterio, D. Paper-based inkjet-printed microfluidic analytical devices. *Angew. Chemie Int. Ed.* **54**, 5294–5310 (2015).

72. Li, J., Rossignol, F. & Macdonald, J. Inkjet printing for biosensor fabrication: combining chemistry and technology for advanced manufacturing. *Lab Chip* **15**, 2538–2558 (2015).

73. Li, X., Tian, J., Garnier, G. & Shen, W. Fabrication of paper-based microfluidic sensors by printing. *Colloids surfaces B Biointerfaces* **76**, 564–570 (2010).

74. Shibata, H., Hiruta, Y. & Citterio, D. Fully inkjet-printed distance-based paper microfluidic devices for colorimetric calcium determination using ion-selective optodes. *Analyst* **144**, 1178–1186 (2019).

75. Garnier, G. & Then, W. L. PAPER MICROFLUIDICS: APPLICATIONS AND PERSPECTIVES. in *Advances in Pulp and Paper Research, Oxford 2017: Transactions of the 16th Fundamental Research Symposium Held in Oxford: September 2017, in Three Volumes, Pulp & Paper Fundamental Research Society, 2017* 541–583 (2018).

76. Channon, R. B., Nguyen, M. P., Henry, C. S. & Dandy, D. S. Multilayered microfluidic paper-based devices: characterization, modeling, and perspectives. *Anal. Chem.* **91**, 8966–8972 (2019).

77. Mora, M. F. *et al.* Patterning and modeling three-dimensional microfluidic devices fabricated on a single sheet of paper. *Anal. Chem.* **91**, 8298–8303 (2019).

78. Rath, D. & Toley, B. J. Modeling-Guided Design of Paper Microfluidic Networks: A Case Study of Sequential Fluid Delivery. *ACS sensors* **6**, 91–99 (2020).

79. Modha, S., Castro, C. & Tsutsui, H. Recent developments in flow modeling and fluid control for paper-based microfluidic biosensors. *Biosens. Bioelectron.* 113026 (2021).

80. Washburn, E. W. The dynamics of capillary flow. *Phys. Rev.* **17**, 273 (1921).

81. Alsaeed, B. & Mansour, F. R. Distance-based paper microfluidics; principle, technical aspects and applications. *Microchem. J.* **155**, 104664 (2020).

82. Walji, N. & MacDonald, B. D. Influence of geometry and surrounding conditions on fluid flow in paper-based devices. *Micromachines* **7**, 73 (2016).

83. Fu, E. & Downs, C. Progress in the development and integration of fluid flow control tools in paper microfluidics. *Lab Chip* **17**, 614–628 (2017).

84. Chen, C. *et al.* Novel wax valves to improve distance-based analyte detection in paper microfluidics. *Anal. Chem.* **91**, 5169–5175 (2019).

85. Kalish, B., Tan, M. K. & Tsutsui, H. Modifying wicking speeds in paper-based microfluidic devices by laser-etching. *Micromachines* **11**, 773 (2020).

86. Fu, H. *et al.* A paper-based microfluidic platform with shape-memory-polymer-actuated fluid valves for automated multi-step immunoassays. *Microsystems Nanoeng.* **5**, 1–12 (2019).

87. Chen, H., Cogswell, J., Anagnostopoulos, C. & Faghri, M. A fluidic diode, valves, and a sequential-loading circuit fabricated on layered paper. *Lab Chip* **12**, 2909–2913 (2012).

88. Li, B. *et al.* Controlling capillary-driven fluid transport in paper-based microfluidic devices using a movable valve. *Anal. Chem.* **89**, 5707–5712 (2017).

89. Toley, B. J. *et al.* A versatile valving toolkit for automating fluidic operations in paper microfluidic devices. *Lab Chip* **15**, 1432–1444 (2015).

90. Jia, Y. *et al.* Scalable and parallelized biochemical assays in paper devices integrated with a programmable binary valve matrix. *Sensors Actuators B Chem.* **321**, 128466 (2020).

91. Jahanshahi-Anbuhi, S. *et al.* Paper-based microfluidics with an erodible polymeric bridge giving controlled release and timed flow shutoff. *Lab Chip* **14**, 229–236 (2014).

92. Houghtaling, J., Liang, T., Thiessen, G. & Fu, E. Dissolvable bridges for manipulating fluid volumes in paper networks. *Anal. Chem.* **85**, 11201–11204 (2013).

93. Biswas, G. C., Watanabe, T., Carlen, E. T., Yokokawa, M. & Suzuki, H. Switchable hydrophobic valve for controlled microfluidic processing. *ChemPhysChem* **17**, 817–821 (2016).

94. Lai, Y.-T., Tsai, C.-H., Hsu, J.-C. & Lu, Y.-W. Microfluidic Time-Delay Valve Mechanism on Paper-Based Devices for Automated Competitive ELISA. *Micromachines* **10**, 837 (2019).

95. Fu, E., Lutz, B., Kauffman, P. & Yager, P. Controlled reagent transport in disposable 2D paper networks. *Lab Chip* **10**, 918–920 (2010).

96. Toley, B. J. *et al.* Tunable-Delay Shunts for Paper Microfluidic Devices. *Anal. Chem.* **85**, 11545–11552 (2013).

97. Rivas, L., Medina-Sánchez, M., De La Escosura-Muñiz, A. & Merkoçi, A. Improving sensitivity of gold nanoparticle-based lateral flow assays by using wax-printed pillars as delay barriers of microfluidics. *Lab Chip* **14**, 4406–4414 (2014).

98. Lutz, B. *et al.* Dissolvable fluidic time delays for programming multi-step assays in instrument-free paper diagnostics. *Lab Chip* **13**, 2840–2847 (2013).

99. Strong, E. B. *et al.* Wax-printed fluidic time delays for automating multi-step assays in paper-based microfluidic devices (MicroPADs). *Inventions* **4**, 20 (2019).

100. Mendez, S. *et al.* Imbibition in porous membranes of complex shape: quasi-stationary flow in thin rectangular segments. *Langmuir* **26**, 1380–1385 (2010).

101. Schilling, K. M., Lepore, A. L., Kurian, J. A. & Martinez, A. W. Fully enclosed microfluidic paper-based analytical devices. *Anal. Chem.* **84**, 1579–1585 (2012).

102. Modha, S., Shen, Y., Chamouni, H., Mulchandani, A. & Tsutsui, H. Laser-etched grooves for rapid fluid delivery for a paper-based chemiresistive biosensor. *Biosens. Bioelectron.* **180**, 113090 (2021).

103. Giokas, D. L., Tsogas, G. Z. & Vlessidis, A. G. Programming fluid transport in paper-based microfluidic devices using razor-crafted open channels. *Anal. Chem.* **86**, 6202–6207 (2014).

104. Renault, C., Li, X., Fosdick, S. E. & Crooks, R. M. Hollow-channel paper analytical devices. *Anal. Chem.* **85**, 7976–7979 (2013).

105. Glavan, A. C. *et al.* Rapid fabrication of pressure-driven open-channel microfluidic devices in omniphobic RF paper. *Lab Chip* **13**, 2922–2930 (2013).

106. Jahanshahi-Anbuhi, S. *et al.* Creating fast flow channels in paper fluidic devices to control timing of sequential reactions. *Lab Chip* **12**, 5079–5085 (2012).

107. Jariwala, D., Sangwan, V. K., Lauhon, L. J., Marks, T. J. & Hersam, M. C. Carbon nanomaterials for electronics, optoelectronics, photovoltaics, and sensing. *Chem. Soc. Rev.* **42**, 2824–2860 (2013).

108. Lan, Y., Wang, Y. & Ren, Z. F. Physics and applications of aligned carbon nanotubes. *Adv. Phys.* **60**, 553–678 (2011).

109. Nessim, G. D. Properties, synthesis, and growth mechanisms of carbon nanotubes with special focus on thermal chemical vapor deposition. *Nanoscale* **2**, 1306–1323 (2010).

110. Eatemadi, A. *et al.* Carbon nanotubes: Properties, synthesis, purification, and medical applications. *Nanoscale Res. Lett.* **9**, 393 (2014).

111. De Volder, M. F. L., Tawfick, S. H., Baughman, R. H. & Hart, A. J. Carbon nanotubes: Present and future commercial applications. *Science (80-.).* **339**, 535–539 (2013).

112. Peigney, A., Laurent, C., Flahaut, E., Bacsa, R. R. & Rousset, A. Specific surface area of carbon nanotubes and bundles of carbon nanotubes. *Carbon N. Y.* **39**, 507–514 (2001).

113. Zhang, X., Lu, W., Zhou, G. & Li, Q. Understanding the Mechanical and Conductive Properties of Carbon Nanotube Fibers for Smart Electronics. *Adv. Mater.* **32**, 1902028 (2020).

114. Balasubramanian, K. & Burghard, M. Chemically functionalized carbon nanotubes. *Small* **1**, 180–192 (2005).

115. Iijima, S. Helical microtubules of graphitic carbon. *Nature* **354**, 56–58 (1991).

116. Ramnani, P., Saucedo, N. M. & Mulchandani, A. Carbon nanomaterial-based electrochemical biosensors for label-free sensing of environmental pollutants. *Chemosphere* **143**, 85–98 (2016).

117. Guo, T., Nikolaev, P., Thess, A., Colbert, D. T. & Smalley, R. E. Catalytic growth of single-walled manotubes by laser vaporization. *Chem. Phys. Lett.* **243**, 49–54 (1995).

118. Bhushan, B., Luo, D., Schricker, S. R., Sigmund, W. & Zauscher, S. *Handbook of nanomaterials properties*. (Springer Science & Business Media, 2014).

119. Rashid, M. H. O. & Ralph, S. F. Carbon nanotube membranes: Synthesis, properties, and future filtration applications. *Nanomaterials* **7**, 99 (2017).

120. Arnold, M. S., Green, A. A., Hulvat, J. F., Stupp, S. I. & Hersam, M. C. Sorting carbon nanotubes by electronic structure using density differentiation. *Nat. Nanotechnol.* **1**, 60–65 (2006).

121. Arnold, M. S., Stupp, S. I. & Hersam, M. C. Enrichment of single-walled carbon nanotubes by diameter in density gradients. *Nano Lett.* **5**, 713–718 (2005).

122. Green, A. A., Duch, M. C. & Hersam, M. C. Isolation of single-walled carbon nanotube enantiomers by density differentiation. *Nano Res.* **2**, 69–77 (2009).

123. Green, A. A. & Hersam, M. C. Processing and properties of highly enriched double-wall carbon nanotubes. *Nat. Nanotechnol.* **4**, 64–70 (2009).

124. Bati, A. S. R., Yu, L., Batmunkh, M. & Shapter, J. G. Synthesis, purification, properties and characterization of sorted single-walled carbon nanotubes. *Nanoscale* **10**, 22087–22139 (2018).

125. Kaisti, M. Detection principles of biological and chemical FET sensors. *Biosens. Bioelectron.* **98**, 437–448 (2017).

126. Chartuprayoon, N., Zhang, M., Bosze, W., Choa, Y. H. & Myung, N. V. One-dimensional nanostructures based bio-detection. *Biosens. Bioelectron.* **63**, 432–443 (2015).

127. Heller, I. *et al.* Identifying the mechanism of biosensing with carbon nanotube transistors. *Nano Lett.* **8**, 591–595 (2008).

128. Heller, I. *et al.* Influence of electrolyte composition on liquid-gated carbon nanotube and graphene transistors. *J. Am. Chem. Soc.* **132**, 17149–17156 (2010).

129. Krishnan, S. K., Singh, E., Singh, P., Meyyappan, M. & Nalwa, H. S. A review on graphene-based nanocomposites for electrochemical and fluorescent biosensors. *RSC Adv.* **9**, 8778–8881 (2019).

130. Zaid, M. H. M. *et al.* PNA biosensor based on reduced graphene oxide/water soluble quantum dots for the detection of Mycobacterium tuberculosis. *Sensors Actuators B Chem.* **241**, 1024–1034 (2017).

131. Karajanagi, S. S., Vertegel, A. A., Kane, R. S. & Dordick, J. S. Structure and function of enzymes adsorbed onto single-walled carbon nanotubes. *Langmuir* **20**, 11594–11599 (2004).

132. Kwon, O. S. *et al.* Fabrication and characterization of inkjet-printed carbon nanotube electrode patterns on paper. *Carbon N. Y.* **58**, 116–127 (2013).

133. Moore, V. C. *et al.* Individually Suspended Single-Walled Carbon Nanotubes in Various Surfactants. *Nano Lett.* **3**, 1379–1382 (2003).

134. Fennell, J. F., Hamaguchi, H., Yoon, B. & Swager, T. M. Chemiresistor devices for chemical warfare agent detection based on polymer wrapped Single-Walled carbon nanotubes. *Sensors (Switzerland)* **17**, 982 (2017).

135. Mago, G., Kalyon, D. M. & Fisher, F. T. Polymer crystallization and precipitation-induced wrapping of carbon nanofibers with PBT. *J. Appl. Polym. Sci.* **114**, 1312–1319 (2009).

136. O'Connell, M. J. *et al.* Reversible water-solubilization of single-walled carbon nanotubes by polymer wrapping. *Chem. Phys. Lett.* **342**, 265–271 (2001).

137. Star, A. *et al.* Preparation and properties of polymer- wrapped single-walled carbon nanotubes. *Angew. Chemie - Int. Ed.* **113**, 1771–1775 (2001).

138. Xu, Y., Pehrsson, P. E., Chen, L., Zhang, R. & Zhao, W. Double-stranded DNA single-walled carbon nanotube hybrids for optical hydrogen peroxide and glucose sensing. *J. Phys. Chem. C* **111**, 8638–8643 (2007).

139. Zheng, M. *et al.* DNA-assisted dispersion and separation of carbon nanotubes. *Nat. Mater.* **2**, 338–342 (2003).

140. Gong, H. *et al.* Biomembrane-Modified Field Effect Transistors for Sensitive and Quantitative Detection of Biological Toxins and Pathogens. *ACS Nano* **13**, 3714–3722 (2019).

141. Mao, S., Lu, G., Yu, K. & Chen, J. Specific biosensing using carbon nanotubes functionalized with gold nanoparticle–antibody conjugates. *Carbon N. Y.* **48**, 479–486 (2010).

142. Chen, R. J., Zhang, Y., Wang, D. & Dai, H. Noncovalent sidewall functionalization of single-walled carbon nanotubes for protein immobilization. *J. Am. Chem. Soc.* **123**, 3838–3839 (2001).

143. Simmons, T. J., Bult, J., Hashim, D. P., Linhardt, R. J. & Ajayan, P. M. Noncovalent functionalization as an alternative to oxidative acid treatment of single wall carbon nanotubes with applications for polymer composites. *ACS Nano* **3**, 865–870 (2009).

144. Zhou, Y., Fang, Y. & Ramasamy, R. P. Non-covalent functionalization of carbon nanotubes for electrochemical biosensor development. *Sensors (Switzerland)* **19**, 392 (2019).

145. Kong, J. *et al.* Nanotube molecular wires as chemical sensors. *Science (80-.).* **287**, 622–625 (2000).

146. Tlili, C., Myung, N. V., Shetty, V. & Mulchandani, A. Label-free, chemiresistor immunosensor for stress biomarker cortisol in saliva. *Biosens. Bioelectron.* **26**, 4382–4386 (2011).

147. Wang, C. *et al.* Wafer-scale fabrication of separated carbon nanotube thin-film transistors for display applications. *Nano Lett.* **9**, 4285–4291 (2009).

148. Kholghi Eshkalak, S. *et al.* A review on inkjet printing of CNT composites for smart applications. *Appl. Mater. Today* **9**, 372–386 (2017).

149. Medina-Sánchez, M., Martínez-Domingo, C., Ramon, E. & Merkoçi, A. An Inkjet-Printed Field-Effect Transistor for Label-Free Biosensing. *Adv. Funct. Mater.* **24**, 6291–6302 (2014).

150. Taleat, Z., Khoshroo, A. & Mazloum-Ardakani, M. Screen-printed electrodes for biosensing: A review (2008-2013). *Microchim. Acta* **181**, 865–891 (2014).

151. Shao, W. *et al.* Probing Ca2+-induced conformational change of calmodulin with gold nanoparticle-decorated single-walled carbon nanotube field-effect transistors. *Nanoscale* **11**, 13397–13406 (2019).

152. Silva, G. O. *et al.* Nanoelectronic Discrimination of Nonmalignant and Malignant Cells Using Nanotube Field-Effect Transistors. *ACS Sensors* **2**, 1128–1132 (2017).

153. García-Aljaro, C. *et al.* Carbon nanotubes-based chemiresistive biosensors for detection of microorganisms. *Biosens. Bioelectron.* **26**, 1437–1441 (2010).

154. Das, B. K. *et al.* Single-walled carbon nanotubes chemiresistor aptasensors for small molecules: Picomolar level detection of adenosine triphosphate. *Chem. Commun.* **47**, 3793–3795 (2011).

155. Vedala, H. *et al.* Nanoelectronic detection of lectin-carbohydrate interactions using carbon nanotubes. *Nano Lett.* **11**, 170–175 (2011).

156. Weizmann, Y., Chenoweth, D. M. & Swager, T. M. DNA-CNT nanowire networks for DNA detection. *J. Am. Chem. Soc.* **133**, 3238–3241 (2011).

157. Lerner, M. B. *et al.* Hybrids of a genetically engineered antibody and a carbon nanotube transistor for detection of prostate cancer biomarkers. *ACS Nano* **6**, 5143–5149 (2012).

158. Subramanian, S. *et al.* Rapid, sensitive and label-free detection of Shiga-toxin producing Escherichia coli O157 using carbon nanotube biosensors. *Biosens. Bioelectron.* **32**, 69–75 (2012).

159. Lerner, M. B., Dailey, J., Goldsmith, B. R., Brisson, D. & Charlie Johnson, A. T. Detecting Lyme disease using antibody-functionalized single-walled carbon nanotube transistors. *Biosens. Bioelectron.* **45**, 163–167 (2013).

160. Chang, J. *et al.* Single-walled carbon nanotube field-effect transistors with graphene oxide passivation for fast, sensitive, and selective protein detection. *Biosens. Bioelectron.* **42**, 186–192 (2013).

161. Ramnani, P., Gao, Y., Ozsoz, M. & Mulchandani, A. Electronic detection of microRNA at attomolar level with high specificity. *Anal. Chem.* **85**, 8061–8064 (2013).

162. Münzer, A. M. *et al.* Sensing reversible protein-ligand interactions with single-walled carbon nanotube field-effect transistors. *J. Phys. Chem. C* **118**, 17193–17199 (2014).

163. Tan, F., Saucedo, N. M., Ramnani, P. & Mulchandani, A. Label-free electrical immunosensor for highly sensitive and specific detection of microcystin-LR in water samples. *Environ. Sci. Technol.* **49**, 9256–9263 (2015).

164. Wordofa, D. N., Ramnani, P., Tran, T. T. & Mulchandani, A. An oligonucleotide-functionalized carbon nanotube chemiresistor for sensitive detection of mercury in saliva. *Analyst* **141**, 2756–2760 (2016).

165. Wasik, D., Mulchandani, A. & Yates, M. V. A heparin-functionalized carbon nanotube-based affinity biosensor for dengue virus. *Biosens. Bioelectron.* **91**, 811–816 (2017).

166. Saucedo, N. M., Gao, Y., Pham, T. & Mulchandani, A. Lectin- and saccharide-functionalized nano-chemiresistor arrays for detection and identification of pathogenic bacteria infection. *Biosensors* **8**, 63 (2018).

167. Wasik, D., Mulchandani, A. & Yates, M. V. Salivary detection of dengue virus NS1 protein with a label-free Immunosensor for early dengue diagnosis. *Sensors* **18**, 2641 (2018).

168. Hatada, M., Tran, T. T., Tsugawa, W., Sode, K. & Mulchandani, A. Affinity sensor for haemoglobin A1c based on single-walled carbon nanotube field-effect transistor and fructosyl amino acid binding protein. *Biosens. Bioelectron.* **129**, 254–259 (2019).

169. Tran, T. T., Clark, K., Ma, W. & Mulchandani, A. Detection of a secreted protein biomarker for citrus Huanglongbing using a single-walled carbon nanotubes-based chemiresistive biosensor. *Biosens. Bioelectron.* **147**, 111776 (2020).

170. Sedki, M., Shen, Y. & Mulchandani, A. Nano-FET-enabled biosensors: Materials perspective and recent advances in North America. *Biosens. Bioelectron.* 112941 (2020).

Chapter 3. Development of Ultrasensitive Single-Walled Carbon Nanotubes Chemiresistive Biosensors on Vertical-Flowed Paper-Based Microfluidics.

This chapter is based on, or in part a reprint of the material as it appears in Shen, Y., Tran, T. T., Modha, S., Tsutsui, H., & Mulchandani, A. (2019). A paper-based chemiresistive biosensor employing single-walled carbon nanotubes for low-cost, point-of-care detection. *Biosensors and Bioelectronics*, **130**, 367-373., and Modha, S., Shen, Y., Chamouni, H., Mulchandani, A., & Tsutsui, H. (2021). Laser-etched grooves for rapid fluid delivery for a paper-based chemiresistive biosensor. *Biosensors and Bioelectronics*, **180**, 113090.

3.1 Abstract

Paper-based biosensors are promising for low-cost diagnostics. However, its widespread use has been hampered due to a lack of sensitive detection methods that can be easily implemented on paper substrates. On the other hand, single-walled carbon nanotubes (SWCNTs) -based chemiresistive biosensors are gaining popularity as label-free, highly sensitive and specific biosensors. However, traditional SWCNT-based chemiresistors need to be more affordable for use in resource-limited settings. In this study, we report fabrication, optimization, and analytical characterization of a chemiresistive biosensor on paper for label-free immunosensing. We synthesized a water-based ink using pyrene carboxylic acid (PCA) through non-covalent π-π stacking interaction between PCA and SWCNTs. The PCA/SWCNTs ink concentration can reach ~ 4 mg/mL and was stable at

room temperature for one month. We introduced a combination of wax printing and vacuum filtration to fabricate the hydrophilic channels and the well-defined PCA/SWCNTs ink deposition on paper in a facile manner requiring no additional masks or stencils. Specific antibodies were then functionalized on the PCA/SWCNTs. Quantitative and selective detection of human serum albumin (HSA) is demonstrated with a limit of detection (LOD) of 1 pM. This low LOD is attributed to the porous structure of the paper surface, which can accommodate more SWCNTs. Furthermore, the hydroxyl group-containing cellulose fibers help connect the SWCNTs into an electrical network.

To incorporate more complex assays into paper, these devices must become more sophisticated, through the sequential delivery of different liquids or reagents without user intervention. Many flow control strategies focus on slowing the fluid down. However, this can lead to increased assay times and sample loss due to evaporation. We report the use of a CO_2 laser to create etched grooves on paper to accelerate wicking speeds in paper-based microfluidic devices. Our findings showed that simply cutting a slit into the paper created the fastest wicking channels. Laser-etched grooves were successfully used to design a fluid-handling architecture for a chemiresistive paper-based biosensor. The grooves facilitated rapid, sequential delivery of HSA sample and wash buffer. HSA spiked in phosphate buffer, artificial urine, and artificial saliva was successfully detected at as low as 15 pM. The developed paper-based chemiresistive biosensor is easy to fabricate for rapid, sensitive, and selective detection of HSA. This work provides a potential platform for automated, disposable paper-based biosensors with multiplexed detection capability and microfluidic controls.

3.2 Introduction

More than 95% of deaths in developing countries are due to the lack of cost-effective medical interventions[1]. Accurate and affordable diagnostics are important in the medical care systems, especially in developing areas[2]. Paper-based microfluidics is an emerging field of low-cost miniaturized analytical assays. Although there are some commercial paper-based analytical tools such as home pregnancy tests[3] and pH test strips[4], it is only recently that paper has received increasing attention as a promising substrate for analytical uses in the laboratory[5–7]. Paper-based sensors have notable advantages: (1) easy fabrication; (2) minimum instrument requirements; (3) possible low-power mode due to its intrinsic wicking capability; (4) portability; (5) biocompatibility and biodegradability; and (6) low cost. Paper is also favorable in reducing the liquids convection effect[8]. In addition, the surface roughness and porosity of paper substrate leads to an increased surface area for depositing electrical material, resulting in improved sensor performance[9]. These features make paper a suitable substrate for disposable sensors with potential microfluidic controls.

Numerous detection principles are employed in paper-based biosensors such as optical/colorimetric, electro-chemiluminescent and electrochemical[10]. However, the majority of paper-based sensors are limited by a poor limit of detection (LOD)[5], low sensitivity[11], and variation in analytical imaging tools from lab to lab[12]. In addition, sensors with labeling require complicated handling and operation[6]. Electrochemical biosensors are advantageous for being insensitive to light and dust while providing high sensitivity and selectivity[13].

SWCNTs are almost entirely composed of surface atoms, which enable them to be highly sensitive to chemical changes on the surface of the nanomaterial. The ultrahigh surface-to-volume ratio renders SWCNTs a Debye length that is comparable to the size of the nanostructures, which causes significant modulation of their electronic properties upon exposure to analytes[14]. Furthermore, the high charge mobility of SWCNTs enables low-power operations. These properties enable label-free detection of analytes with higher sensitivities and lower LODs[15–17]. Therefore, the integration of paper-based chemiresistive biosensor employing SWCNTs benefits from using both paper and SWCNTs materials.

Technologies to fabricate paper-based channels include photolithography[18], screen-printing[19], lacquer spraying with iron masks[20], vacuum filtration with metal stencils[21], inkjet printing[22] and wax printing[23]. Photolithography is the most precise technology to define hydrophilic channels at a high resolution of 186 ± 13 μm[18]. However, it requires expensive equipment and organic solvents. Abe et al.[22] developed an inkjet printing method to deposit customized materials onto paper substrates. However, hydrophilic channels formation involved the use of highly hydrophobic polymers dissolved in organic solvent and a toluene etching agent. Screen-printing is a relatively simple method, but the resolution is limited to hundreds of micrometers and the inability to reuse the screens is environmentally unfriendly[24]. Other cost-effective methods such as polydimethylsiloxane (PDMS) plotting[25] involve no organic solvents and photoresist but require customized plotters. The paraffin pen has also been employed to define paper-based hydrophobic barriers with low resolution in the centimeter range[26]. Vacuum filtration is also employed where carbon ink is pre-functionalized with specific biorecognition element and deposited

onto paper with small pore sizes using laser-cut metal masks followed by the formation of PDMS hydrophobic barriers[21]. However, this method needs special and brittle paper materials with pore sizes of 200 nm[26] and 800 nm[21], limiting its robustness and wide application beyond the laboratory. Wax printing, on the other hand, has several merits[23] such as (1) simple fabrication process of printing and baking with adequate resolutions; (2) rapid fabrication (5–10 min); (3) low cost (paper and wax printer are easy to obtain) and (4) environmentally-friendliness (no organic solvent in the wax printing and disposability by incineration). These merits make the wax printing method widely compatible with various aqueous solutions of various pH values, acids, bases, and glycerol[27]. Hence, to overcome the aforementioned obstacles with other methods, a SWCNT-based highly sensitive, label-free chemiresistive biosensors on paper using wax printing and vacuum filtration techniques were explored in this study. Selective and quantitative detection of a target analyte (HSA) demonstrated the excellent sensing ability of the proposed paper-based chemiresistor biosensor platform.

Furthermore, to enable the complex procedures that sequentially deliveries of multiple reagents, we developed laser-etched grooves in paper for rapid fluid delivery[28]. Untreated paper wicks very slowly because its fibrous network presents narrow and tortuous paths which the fluid must follow along[29,30]. Efforts to accelerate wicking in paper channels have included either sandwiching the paper between polymer films[31,32], creating a two-ply structure[33,34], physically modifying pore sizes by laser ablation[35], or by removing regions of the paper to create ‘macro capillaries’ for the liquid to flow through[36–39]. Of interest is the work of Giokas et al.[37] and Liu et al.[39], who demonstrated that creating

parallel grooves onto paper channels using either a plotter or a CO_2 laser can lead to much faster wicking speeds. In this study, we build upon the work of Giokas et al. and Liu et al.[37,39] by conducting a more thorough analysis of laser-etched grooves on paper. In addition to finding optimum groove parameters, we demonstrated the use of laser-etched grooves on paper for sequential delivery for the chemiresistive biosensor.

3.3 Materials and Methods

3.3.1 Materials and Instruments

Pyrene carboxylic acid (PCA) was purchased from Tokyo Chemical Industry Co., Ltd. (Portland, OR, USA). SWCNTs (grade P3) was purchased from Carbon Solutions, Inc. (Riverside, CA, USA). N, N-Dimethylformamide (DMF), acetone, (1-ethyl-3-(3-dimethylaminopropyl)carbodiimide hydrochloride) (EDC), N-hydroxysulfosuccinimide (NHS), and ethanolamine were purchased from Fisher Scientific (Chino, CA, USA). Methanol, Whatman 5 qualitative filter paper, human serum albumin (HSA), and bovine serum albumin (BSA) were purchased from Sigma-Aldrich Corp. (St. Louis, MO, USA). Tween 20 (100%) was purchased from Bio-Rad (Hercules, CA, USA). Monoclonal anti-HSA antibody was purchased from BiosPacific, Inc. (Emeryville, CA, USA). N2 and NO2 gas cylinders were obtained from Airgas (Riverside, CA, USA). Silver paste was purchased from Ted Pella, Inc. (Redding, CA, USA). Polytetrafluoroethylene (PTFE) membranes were obtained from Millipore Corp. (Burlington, MA, USA). Ultra-sonication was done using a Branson m1800 (Danbury, CT, USA). Wax printing was done using a Xerox ColorQube 8880 (Norwalk, CT, USA). Electrochemical workstation CH Instrument 6005E

(Austin, TX, USA) and Keithley 2636 system source meter (Tektronix, Beaverton, OR, USA) were used to collect electrical signals.

3.3.2 Synthesis and Characterization of Aqueous Single-Walled Carbon Nanotubes

A schematic flowchart of the water-based PCA/SWCNTs ink is shown in **Figure 3.1**. In brief, 50 mg SWCNTs powder and 25 mg PCA were dispersed in 25 mL DMF individually. Twenty minutes of ultra-sonication ensured good dispersion of SWCNTs in DMF. SWCNTs/DMF and PCA/DMF were well mixed with stirring for 12 h to achieve complete π-π stacking interaction. The mixture was then vacuum filtered by PTFE membranes to accumulate a wet cake of PCA/SWCNTs. Consecutive washes with methanol and DI water removed excessive solvent and PCA. The PCA/SWCNTs was collected and weighted carefully before re-dispersion in Milli-Q water to obtain a desired concentration.

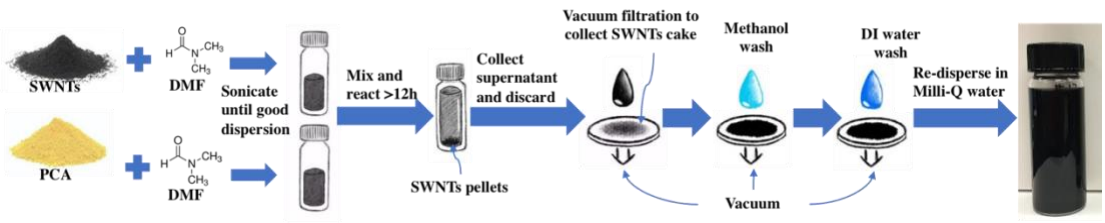

Figure 3.1 Schematic of water-based PCA/SWNTs ink synthesis.

3.3.3 Wax Printing and PCA/SWCNTs Ink Deposition

The wax printing process is shown in **Figure 3.2**. Patterns were pre-designed on a computer using GIMP software. Fluidic channels (21 mm long and 1 mm wide) were created by printing the wax patterns onto the paper surface. Baking at 170 °C for 5 min melted the

wax ink into the paper matrix, creating hydrophobic regions throughout the thickness of the paper. A second layer of the pattern was printed on the same side of the paper to ensure adequate hydrophobicity near the paper surface. The paper substrates were then placed at the center of a vacuum filter funnel under a vacuum pressure of ~78 kPa. A 3 mL syringe was used to transfer the PCA/SWCNTs ink onto the paper surface. The vacuum forced the ink onto the paper while the wax barrier confined the ink to the sensing region. Silver paste was prepared in acetone at 2.15 g/mL and silver terminals were painted on each end of the sensing channel with a brush of 0.25 cm diameter. The terminals were subsequently dried at room temperature.

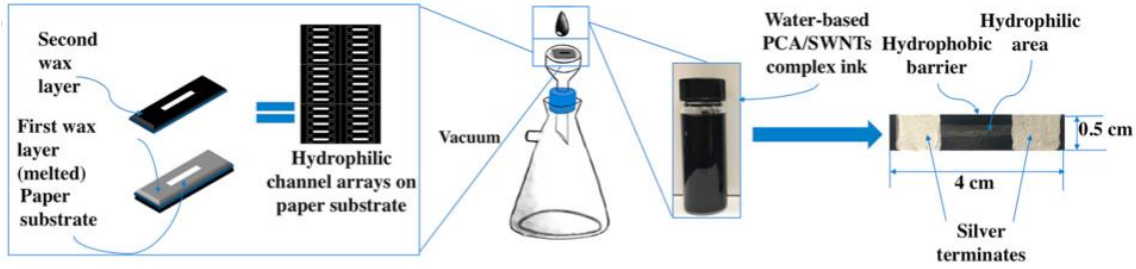

Figure 3.2 Schematic of wax printing and PCA/SWNTs ink deposition processes.

3.3.4 Preliminary NO_2 Gas Sensing

Figure 3.3 shows the set-up used for gas sensing. A gas chamber made of poly (methyl methacrylate) (PMMA) and PDMS gasket ensured the sealing of the chamber. NO_2 gas and N_2 gas were supplied from gas cylinders. Under the control of mass flow controllers (MFCs), NO_2 was diluted in a gas mixer with N_2 before approaching the PCA/SWCNTs channels. Each pulse of NO_2 was 2 min and the N_2 recovery was 10 min.

A LabView-controlled Keithley 2636B instrument applied 0.1 V across the source-drain electrodes and measured the source-drain current with respect to time.

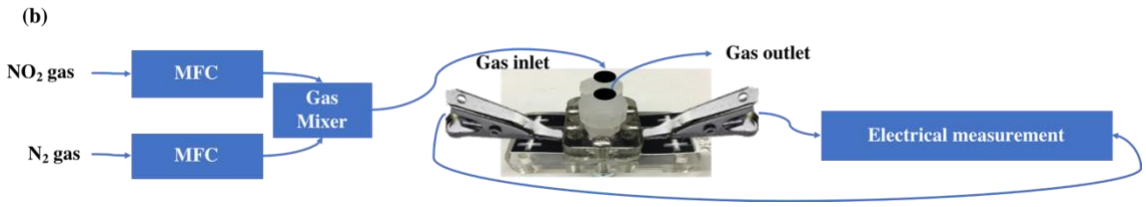

Figure 3.3 Schematic of NO_2 gas sensing set-up used for optimization of initial resistance of the sensing channels.

3.3.5 Functionalization of Anti-HSA Antibody

All incubations were conducted in humid air with a wet Kimwipe around the sensors at room-temperature. Fifteen seconds of vacuum pressure at 78 kPa was adequate to remove 20 µL bulk fluid vertically through the sensing channels. Monoclonal anti-HSA antibodies were covalently attached to the carboxylic groups on the PCA/SWCNTs by EDC/NHS chemistry. First, the sensing channels were immersed in 10 mM phosphate buffer (PB) (pH 6.2) containing 4 mM EDC and 8 mM NHS for 20 min to activate the carboxylic groups, followed by adequate 10 mM PB wash. Diluted anti-HSA antibody in 10 mM PB (pH 6.2) at 20 µg/mL was pipetted onto the sensing channels and incubated for 2 h followed by washing with 10 mM PB. Quenching and blocking agent were prepared in 10 mM PB (pH 6.2) and quenching of unreacted -NHS and blocking of bare SWCNTs were completed by pipetting 0.1 M ethanolamine, with 10 mM PB washes, and 0.1% Tween 20, with 10 mM PB washes, respectively. Then the functionalized paper-based devices were ready for biosensing. The negative controls were fabricated with anti-HSA antibody on the sensor while sensing with 10 mM PB as blank samples for 6 times per

sensor or 30 μM BSA. The positive control sensors were fabricated without antibody functionalization but with the quenching and blocking process with ethanolamine and Tween 20, respectively.

3.3.6 Sample Incubation and Electrochemical Measurements

All electrochemical measurements were carried out with a CH Instrument (Model 6005E) and a Keithley source meter (Model 2636) at room temperature. Flat aluminum clips were used for connecting to the silver terminals. For NO_2 gas sensing, Keithley instrument obtained the long-time resistance records with a constant source-drain voltage at 0.1 V. For sensing liquid sample, the electrical measurements were done by measuring the I-V curve by sweeping the potential between source and drain using linear sweep voltammetry (LSV) from − 0.1 V to 0.1V. The reciprocal of the slope of the I-V curve was the resistance of the sensing channels. All HSA standard solutions were prepared in 10 mM PB at a desired pH. BSA were prepared at 30 μM in 10 mM PB (pH 7.4) for the specificity study. Each time, 20 μL of analyte sample was pipetted onto the sensing channel. After 5 min incubation, vacuum force removed the bulk fluid and 10 mM PB (at the same pH value of the analyte samples) washes under vacuum removed unbound molecules (**Figure 3.4**).

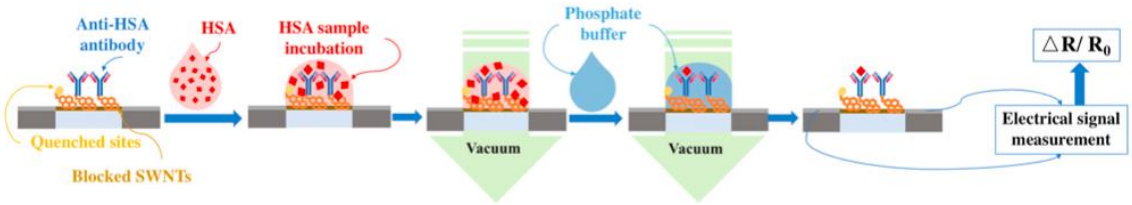

Figure 3.4 Schematic of sensing protocol including sample incubation and PB wash process.

3.3.7 Integration of SWCNTs Chemiresistor with Laser-Etched Grooves for Fully Assembled Biosensor

The demonstration device utilizes a paper-based chemiresistive biosensor employing SWCNTs, which we recently reported[40]. The dry initial resistance of the sensing channels after functionalization, quenching, and blocking was 9.90 ± 0.31 kΩ.

Groove designs were created in Adobe Illustrator CC (Adobe Inc, San Jose, CA). Whatman 4 filter paper (GE Healthcare, Chicago, IL) was cut out and etched using an Epilog Zing 16 30W CO_2 laser cutter (Epilog Lasers, Golden, CO). Laser power and frequency were set at 5% and 5000 Hz respectively, while laser speed was varied between 20% and 100% to etch grooves with different depths. The nominal thickness of untreated filter paper is 180 μm.

The rest of the demonstration device consisted of a fluid-handling layer, which facilitated rapid, sequential delivery of a sample and wash buffer and waste pads that absorbed excess fluid as it passed through the sensor. Both fluid-handling and waste layers were constructed from Whatman 4 filter paper and cut out using the CO_2 laser. The device itself was constructed using a bottom-up approach. A strip of Uline tape was placed adhesive-side up onto a piece of thick, double-sided tape (Style-592, Intertape Polymer Group, Newport Beach, CA). This double-sided tape acted as a rigid support for the device. The waste pad was then attached to the Uline tape, followed by the sensor and the fluid-handling layer on top of that. Another piece of Uline tape was placed on top of the fluid handling layer to seal together this three-layer sandwich. This top layer of tape had holes

cut into it to allow addition of sample and wash buffer and to connect electrodes to the sensor for electrical measurement.

All electrical measurements were carried out using a potentialstat (model 600E, CH Instruments, Austin TX) as previously reported[40]. Flat alligator clips were connected to the silver conductive pads. Electrical measurements were performed by measuring the I–V curve using LSV from − 0.1 V to 0.1 V. The reciprocal of the slope of the curve was the resistance of the sensor. Real-time monitoring was done by amperometrical monitoring of current vs. time with a source-drain bias at 0.1 V.

Devices were tested by first priming the chemiresistive sensor with 20 μL of 10 mM PB (pH 7.4), which was added to the sample inlet and allowed to saturate the sensor for 2 min. HSA solutions were prepared using PB, artificial urine (AU) and artificial saliva (AS). AU and AS formulations were adapted from previous studies[41,42]. Preparation of AU included the following: 170 mM urea, 90 mM KCl, 90 mM NaCl, 25 mM NH_4Cl, 7 mM creatinine, 7 mM K_2HPO_4, 7 mM KH_2PO_4, 2.5 mM $CaCl_2$, 2 mM $MgSO_4$, 2 mM $MnCl_2$, and 0.4 mM uric acid mixed together in DI H_2O with pH adjusted to 7.4. AS consisted of 0.6 g/L of Na_2HPO_4, 0.6 g/L of anhydrous $CaCl_2$, 0.4 g/L of KCl, 0.4 g/L of NaCl, 4 g/L of mucin and 4 g/L of urea dissolved in deionized H_2O with pH adjusted to 7.4. Then, 20 μL of HSA sample (prepared at varying concentrations in PB, AU, or AS) and another 60 μL of 10 mM PB were simultaneously added to the sample and wash buffer inlets, respectively. Measurements were taken until the output current achieved steady state.

3.4 Results and Discussions

3.4.1 Characterization of PCA/SWCNTs Ink

PCA is one of the simplest molecules that contains both carboxylic and pyrene groups and is thus an ideal bi-linker molecule for facilitating both dispersion of SWCNTs in aqueous media and its functionalization with biomolecules without affecting the electrical properties. SEM images in **Figure 3.5a** and **Figure 3.5b** show the distinct difference between unmodified SWCNTs and the PCA modified SWCNTs (from here on designated as PCA/ SWCNTs). The unmodified SWCNTs at < 0.1 mg/mL formed large aggregates, whereas the PCA/SWCNTs was more dispersed in water. This was attributed to the π-π stacking that occurs between the pyrene groups and the aromatic structures of SWCNTs. The –COOH groups on the SWCNTs provide the hydrophilic moiety with affinity to water. The PCA/SWCNTs ink can be stable for up to one month at ambient condition (**Figure 3.6**). The Raman spectrum in **Figure 3.5c** shows the D-band and G-band of unmodified SWCNTs and PCA/ SWCNTs at 1340 cm^{-1} and 1595 cm^{-1}, respectively. The D-band is related to the disordered carbon bonding consistent with defects in the graphite lattice of the SWCNTs[43]. The ratio of D-band to G-band was 0.131 and 0.133 for the SWCNTs before and after the PCA modification. The mild change in D-band to G-band ratio, compared to other SWCNTs modification methods[44], confirms that the PCA/SWCNTs retained its mechanical and electrical properties during the non-covalent modification. The increased concentration of carboxylic groups on SWCNTs was confirmed by the FTIR spectrum. The characteristic peaks are demonstrated in **Figure 3.5d** where C-H bending and C-O, C=O, and O-H stretching are pointed out. **Figure 3.5e** also

reveals the UV–vis spectrum of unmodified SWCNTs in H_2O, PCA/SWCNTs in H_2O and PCA in methanol. PCA in methanol showed two characteristic peaks at 274 nm and 341 nm. Clearly, the unmodified SWCNTs showed no obvious peaks, whereas the PCA/SWCNTs showed the absorption peaks corresponding to PCA moieties. These results validated the successful non-covalent modification of PCA on SWCNTs, allowing a higher concentration of carboxylic moieties on SWCNTs. This method enabled a higher dispersibility of carbon nanotubes in water and a higher density of bio-conjugation sites for antibody functionalization. Moreover, since the π-π interaction between SWCNTs and the pyrene structure of PCA is universal among SWCNTs and analogous aromatic ring-containing molecules, this fabrication method provides great potential in the development of non-covalent functionalization of SWCNTs with a variety of bi-linker molecules.

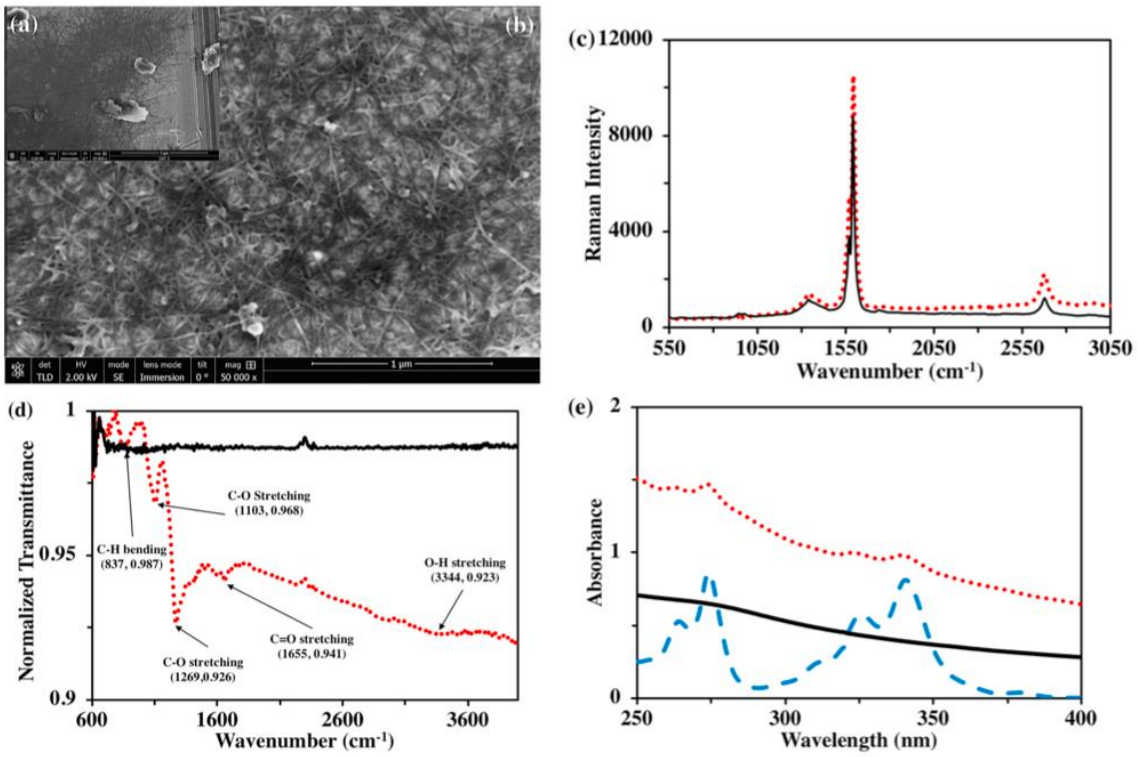

Figure 3.5 Characterizations of water-based unmodified SWNTs and PCA/SWNTs ink. (a) SEM images of unmodified SWNTs/H_2O at < 0.1 mg/mL; (b) PCA/SWNTs in H2O at ~4 mg/mL; (c), (d) and (e) are Raman spectrum, FTIR spectrum and UV–vis spectrum of unmodified SWNTs (solid line), PCA/ SWNTs (dotted line) and PCA/methanol (dashed line), respectively.

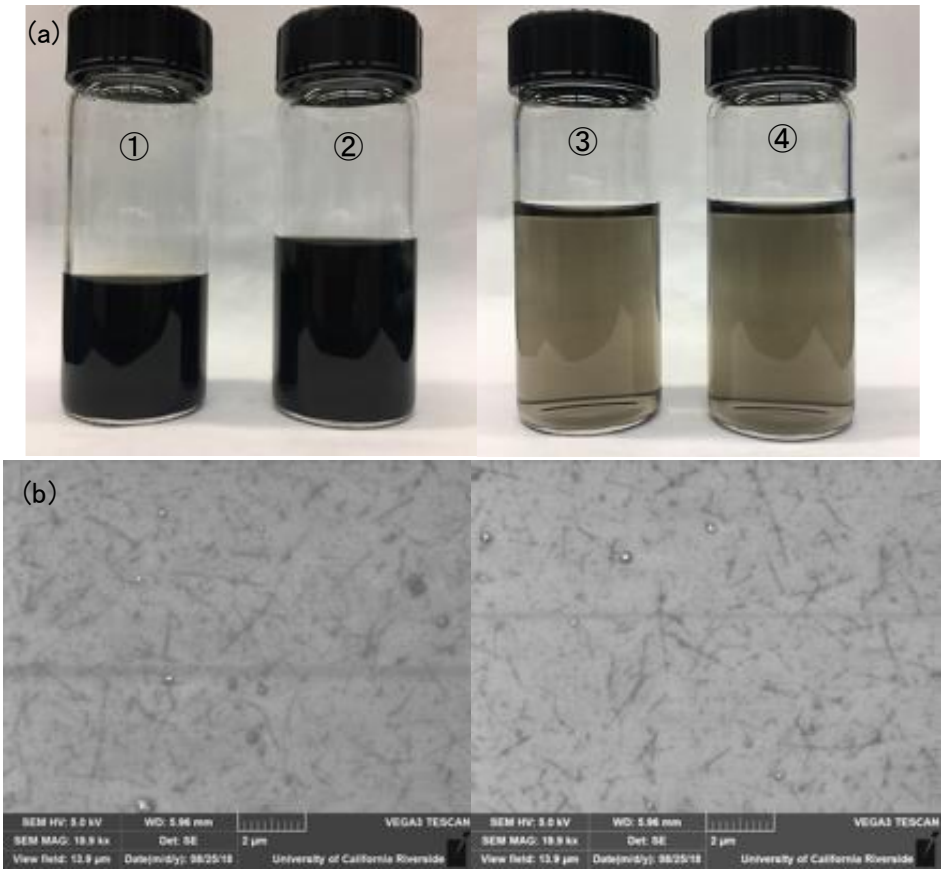

Figure 3.6 Optical images and SEM images of the SWNTs samples. (a) Optical images of freshly prepared (①) and one-month-old (②) PCA/SWNTs ink at 4 mg/mL. and fresh ink (③) and one-month-old ink (④) after dilution to 0.1 mg/mL. The later images highlight the absence of large SWNTs aggregates for both fresh and one month old ink even at low concentration. (b) SEM images of freshly prepared (left) and one-month-old (right) 0.1 mg/mL PCA/SWNTs ink.

3.4.2 SWCNTs Transducing Element Fabrication and Optimization

As is shown in **Figure 3.2**, simple vacuum filtration facilitated the maskless deposition of PCA/SWCNTs ink on paper substrates. The second layer of wax on the paper surface prevented flooding of the PCA/ SWCNTs ink during the deposition process. By varying the volume of PCA/SWCNTs ink, the initial resistance of the transducing element can be tuned. **Figure 3.7a** demonstrates that increasing loading of the PCA/ SWCNTs

decreased the initial resistance. **Figure 3.8** displays the I-V curves of various loadings of PCA/SWCNTs in the hydrophilic channels. When the concentration exceeded 10 μg/mm^2, the resistance plateaued. However, the thickness of the PCA/ SWCNTs layer displays a linear relationship with respect to the PCA/ SWCNTs loading.

The combination of wax printing and vacuum filtration in this study is beneficial compared to previous studies utilizing the vacuum filtration method. Lee et al.[26] and Lei et al.[21] developed a multi-step method to define the sensing regions on paper, in which metal masks are necessary to define the geometry of the carbon materials on paper, followed by time-consuming hydrophobic barrier formation. For example, PDMS formed hydrophobic barrier throughout the thickness of carbon material layers and paper substrate after hours of curing at low temperature (4 °C) to slow the polymerization of PDMS before it finally penetrated to the other side of the paper. Thus, the locations of carbon materials and hydrophilic sensing areas were formed separately. On the other hand, in our method, the determination of hydrophilic sensing areas and the PCA/SWCNTs ink deposition on paper were created in a consistent way where no mask/stencil was needed. Therefore, this method eased the equipment requirements and eliminated the need of gaskets for sealing since wax printed barriers were adequate to ensure well-defined geometries of both the hydrophilic area and PCA/SWCNTs geometry on paper.

It is reported that the initial resistance of the chemiresistor affects the biosensor sensitivity[45]. To achieve the highest sensitivity in the transducing element, we evaluated the performance of our paper-based chemiresistor for sensing of NO_2 gas. **Figure 3.7b** and **Figure 3.7c** shows the responses and optimization of initial resistance of transducer

resistance. When exposed to NO_2, the p-doped semiconducting SWCNTs shifted the Fermi level closer to the valence band. This lead to enriched hole carriers in the SWCNTs and increased the conductance[46]. The optimum initial resistance before bio-functionalization for the PCA/SWCNTs transducing element was between 4.5 kΩ to 5.5 kΩ. Accordingly, the subsequent devices were fabricated with initial resistance within this range.

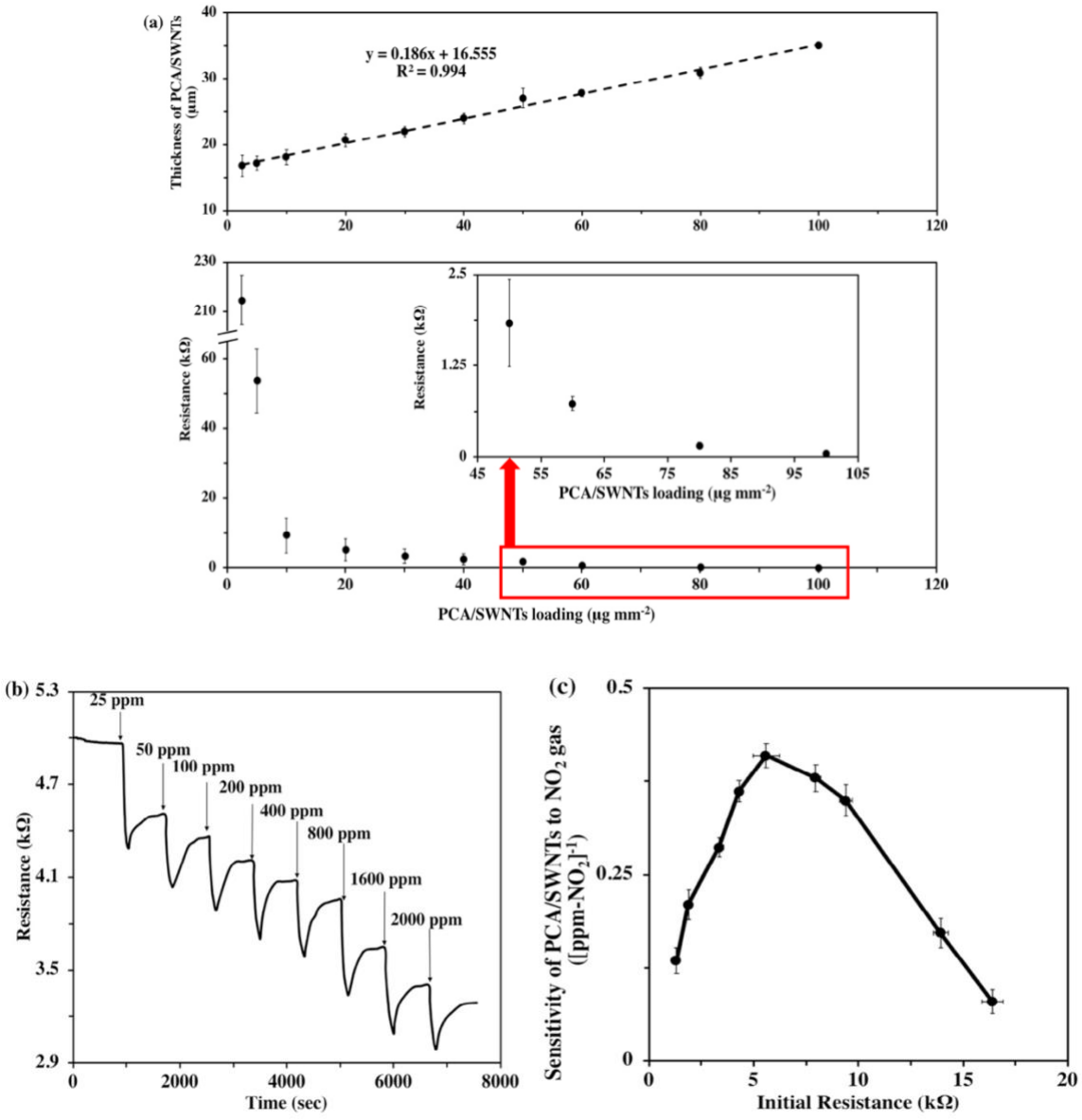

Figure 3.7 Preliminary optimization of PCA/SWNTs density on the sensing channels. (a) The relationships between the loading of PCA/SWNTs on paper versus the initial resistance, and a linear relationship between the thickness and the loading of PCA/SWNTs. Each data point is an average of 6 devices and the error bars represent ± 1 standard deviation; (b) A typical response of PCA/SWNTs to NO_2 gas, with arrows indicate the exposure to NO_2 gas; (c) the changing sensitivity with various initial resistances. Each data point is an average of 9 sensors and the error bars represent ± 1 standard deviation.

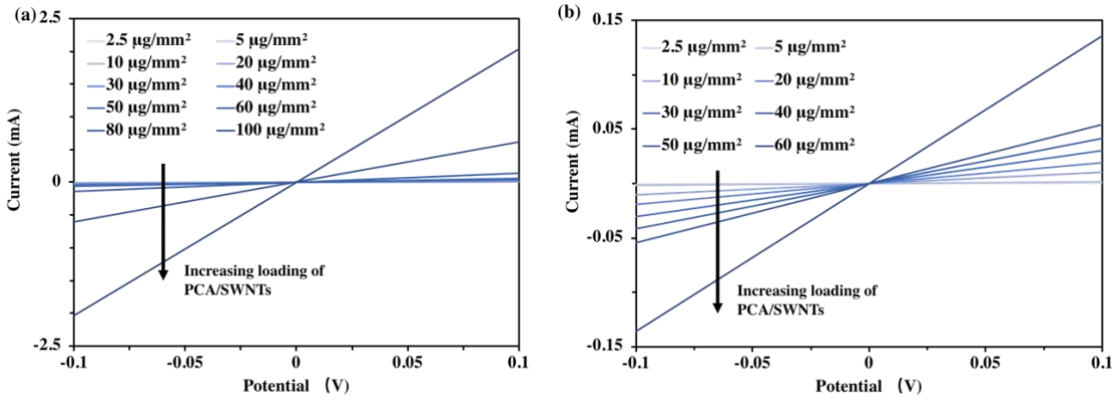

Figure 3.8 I-V curves for increasing loading of PCA/SWNTs ink on hydrophilic channels. (a) PCA/SWNTs loading from 2.5 to 100 µg/mm^2; (b) PCA/SWNTs loading from 2.5 to 60 µg/mm^2.

3.4.3 Biosensor Fabrication, Optimization and Analytical Characteristics

Figure 3.9 shows I-V curves of the device after each modification step during the biosensor fabrication process. The initial resistances were all within the range of 5.0 ± 0.38 kΩ (n = 6), indicating good repeatability of the SWCNTs chemiresistor transducer fabrication process using our new maskless method. After incubation with 10 mM PB (pH 6.3) the resistance increased by ~ 10% (**Figure 3.10**). This is probably because more water molecules in the buffer adsorbed into the SWCNT network and behaved similar to electron donors, which reduced the hole density of p-type SWCNTs[47]. As shown in **Figure 3.10**, while the resistance changes were not significant after the EDC/NHS chemistry and the quenching/blocking processes, there was a dramatic increase upon antibody functionalization. These results prove successful functionalization of antibodies on the sensing channels.

Next, we evaluated the performance of anti-HSA functionalized SWCNTs chemiresistor on paper for detection of HSA. The result showed that the biosensor current

decreased, i.e., the resistance increased, with increasing concentration of HSA (**Figure 3.11**) over a broad dynamic range from 0 to ~ 50 nM HSA. In this study, the analyte sample was incubated for 5 min and the biosensor was washed in between incubation with increasing concentration of analyte sample with a 60 μL single bulk wash of 10 mM PB.

The response of the paper-based chemiresistor biosensor is a function of the volume of buffer wash to remove any free antigen. Two methods of biosensor washing with 10 mM PB post incubation with successive increasing concentration of HSA – a single bulk wash with 60 μL and three washings with 20 μL each – were investigated. A comparison of normalized resistance change $[(R-R_0)/R_0$, where R_0 is the resistance of the device after functionalization, quenching and blocking and R is the resistance after incubation with sample between a single/ bulk wash and multiple washes with smaller volumes showed the bulk wash to be equally efficient as multiple washes (**Figure 3.12a**). This is probably due to the buffer washes traversing vertically through the SWCNTs thickness instead of being diffusion-dependent. This finding is also important as a single wash makes the analysis simple to conduct.

The duration of incubation/immunoreaction of the analyte sample with the biosensor can affect the sensor/chemiresistor sensitivity. A comparison of the biosensor responses for incubation times of 5 and 10 min showed (**Figure 3.12b**) the difference in the sensitivity to be statistically insignificant ($p \approx 0.45 > 0.05$). Therefore, an incubation time of 5 min was selected for subsequent experiments.

The effect of varying amounts of anti-HSA employed for functionalization of SWCNTs channel on the biosensor sensitivity and dynamic range was investigated. As

shown in **Figure 3.12c**, while the biosensor sensitivity, slope of the plot of normalized resistance changes versus HSA concentration increased by 25% when the amount of anti-HSA used for biofunctionalization was increased from 0.2 to 0.4 μg, there was only a 2% gain in sensitivity when the anti-HSA amount was increased further to 0.8 μg per device. A reason might be that the limited bio-conjugation sites on the PCA/SWCNTs channels and the dosage of 0.4 μg anti-HSA antibody per device nearly saturated the available bio-functionalization sites, and therefore no significant further improvement in the sensitivity was seen. Based on these results, the amount of 0.4 μg anti-HSA per device was used in subsequent experiments.

The analytical figures of merits (sensitivity, selectivity, and controls) for the present biosensor were obtained from calibration plots prepared using devices with optimized amount of anti-HSA (0.4 μg per device), incubation time of 5 min with 20 μL of analyte sample with 0 to ~50 nM of HSA and a 60 μL bulk wash with 10 mM PB (**Figure 3.12**). As shown in the figure, the response was a linear function of the log of HSA over the range of 0.015 – 9.43 nM with a sensitivity of 9.44% change per Log_{10}([HSA, nM]). The LOD estimated by S/N = 3 was 1 pM HSA. The sensors had excellent reproducibility as evidenced by a low coefficient of variation, 6.67 – 8.97% of the data points obtained from 12 independent sensors with 0.4 μg antibody per device. In comparison with traditional sensors on the detection of HSA, most of these detection limits were in micromolar range[48]. The increased sensitivity is probably due to the porous and rough surface of the paper substrate compared to smooth surface of Si wafer or glass substrate[49]. Thus, paper substrate can accommodate more SWCNTs with a firm connectivity of SWCNTs on paper[50]. The

cellulose fibers contain multiple hydroxyl groups that form hydrogen bonds not only between cellulose molecules, but also with SWCNTs. Thus, disconnected SWCNTs on paper matrix are electrically bridged even though the paper fiber is dielectric. The carrier hopping and tunneling effects facilitate the inter-tube conduction, which leads to an increased percolation path and decreased effective conduction distance[47]. As a result, the paper-based biosensor sensitivity was increased.

The positive control experiment, in which the sensor without anti-HSA antibody was exposed to 0 to ~ 50 nM HSA (**Figure 3.12a**) showed the biosensor had a minimal response to their exposures confirming the high quality of sensors prepared by the transducer fabrication and biofunctionalization protocol developed in this work. Additional negative control experiment in which a biosensor with anti-HSA antibody was exposed to blank PB, i.e., no HSA, repeatedly for 6 times, had a response of +3.15 ± 0.56% (**Figure 3.13**). The result of repeated vacuum filtrations validated that the observed response of biosensor to HSA was not caused by mechanical disruption in the SWCNTs network. Furthermore, the negative control experiments in which the biosensor with anti-HSA antibody was challenged with 30 μM BSA in PB showed a response of +3.30 ± 0.40% (**Figure 3.13**) confirmed the high selectivity of sensors for HSA.

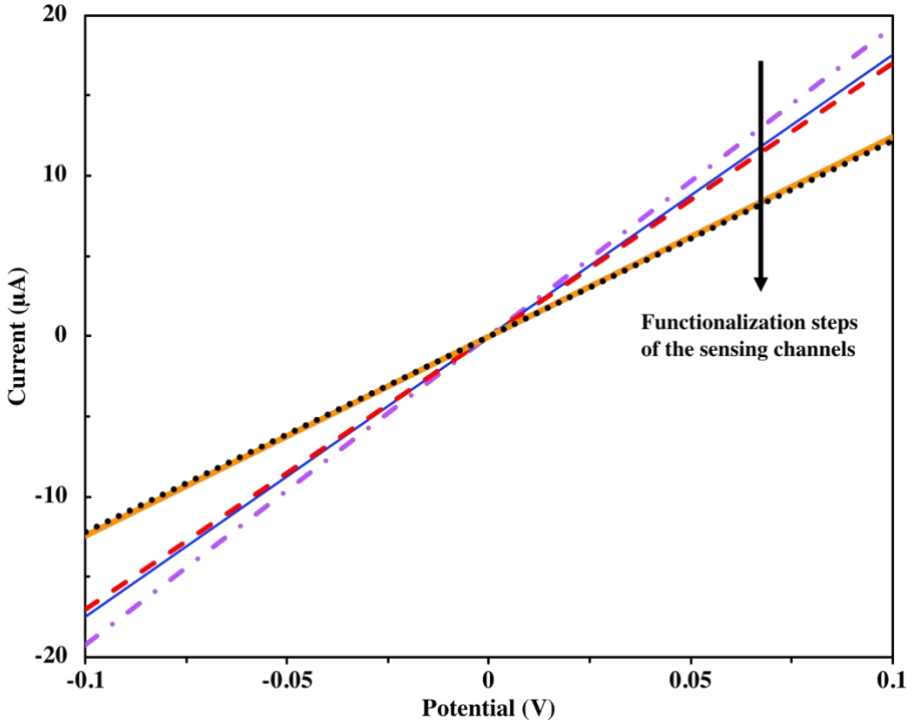

Figure 3.9 I-V curves of the device after each step during the biosensor fabrication process. The subsequent steps are (1) Initial resistance (dash dot line), (2) PB activation (thin solid line), (3) EDC/NHS chemistry (dashed line), (4) anti-HSA antibody functionalization (bold sold line), and (5) quenching and blocking (dotted line). The arrow indicates steps 1 through 5 of functionalization.

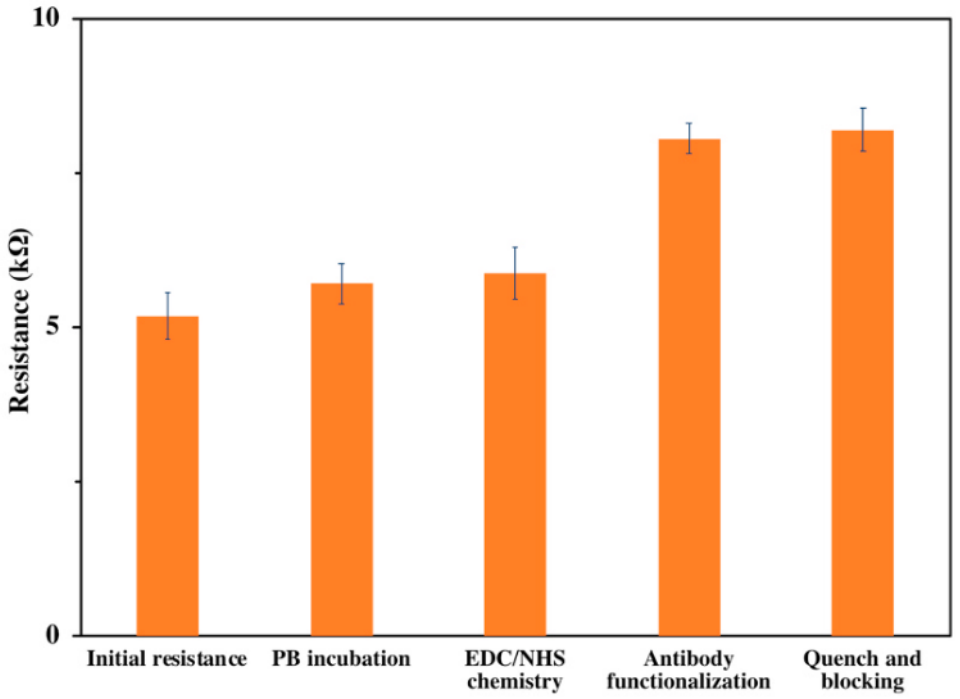

Figure 3.10 Resistances change of the paper-based SWNTs chemiresistor device during the different functionalization steps of biosensor fabrication. The data points in the inset are average of 6 devices and error bars represent ± 1 standard deviation.

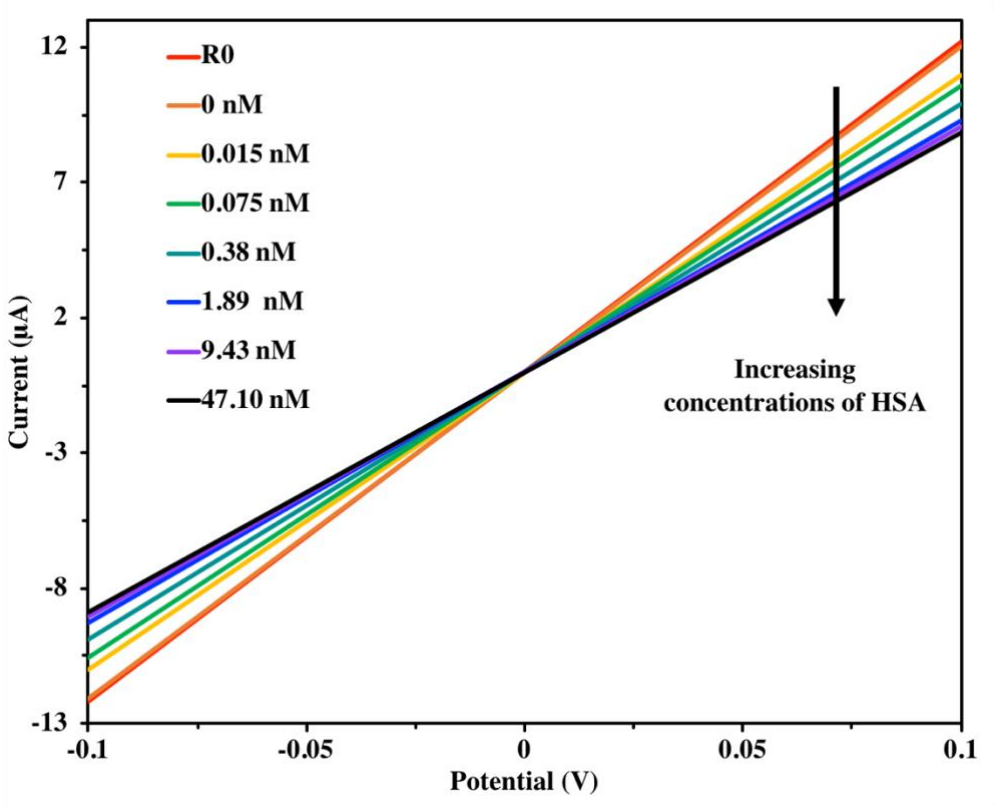

Figure 3.11 I-V curves for the responses of increasing concentrations of HSA from 0 to ~ 50 nM. The arrow indicated the direction of increasing HSA concentrations.

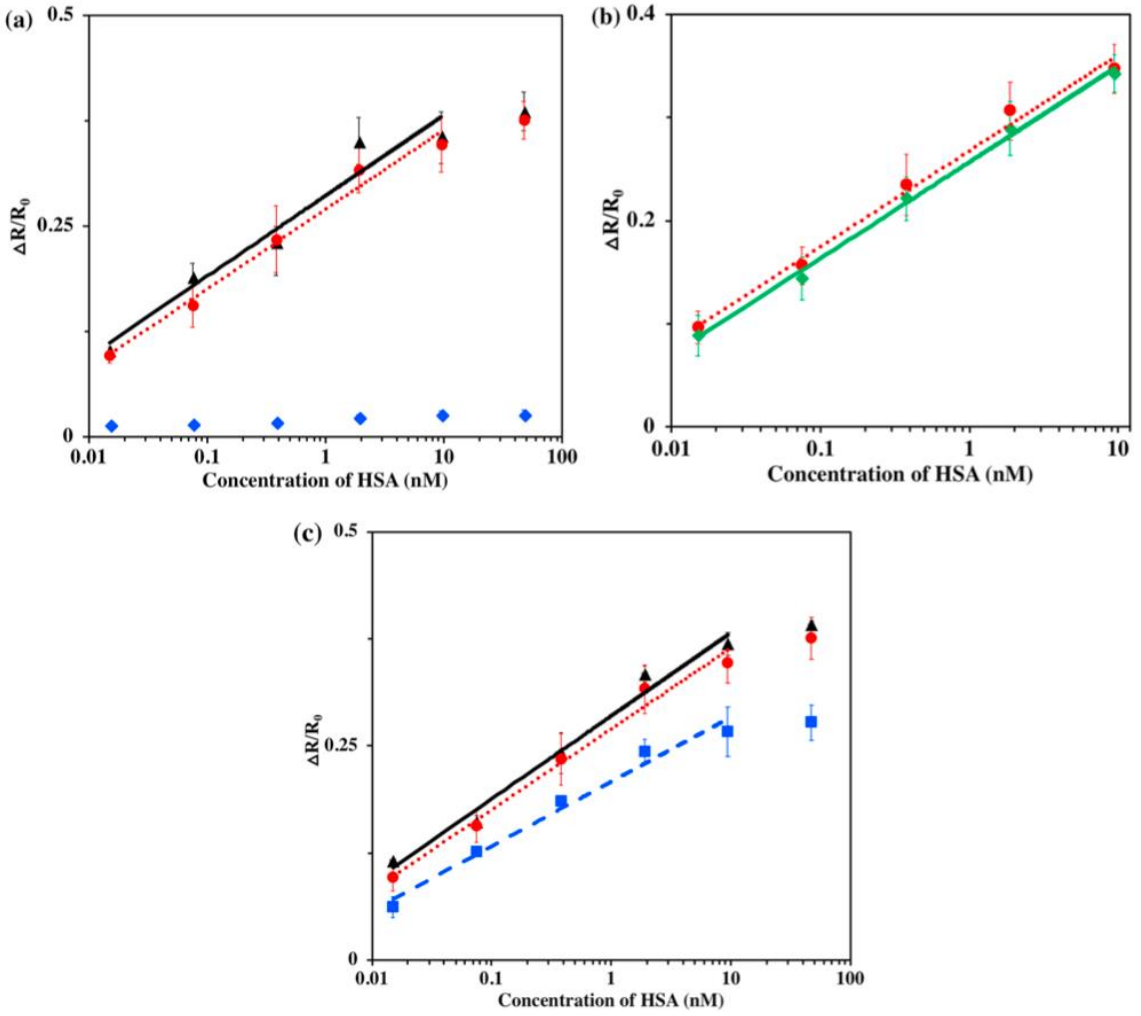

Figure 3.12 The change of the electrical properties of the sensing channels at increasing concentrations. (a) Relative resistance changes for bulk wash mode (•) with linear regression y = 0.0944 Log_{10}(x) + 0.270 with R^2 = 0.984, individual wash mode (▲) with linear regression y = 0.0957 Log_{10}(x) + 0.286 with R^2 = 0.952, and control (◆). Each data point is an average of 12 sensors; (b) Comparison of 5 min (•) and 10min (◆) HSA sample incubation in PB, with regression lines for 5 min HSA incubation (dotted line) y = 0.0944 Log_{10} (x) + 0.2672 with R^2 =0.991, and for 10 min HSA incubation (solid line) y = 0.0932 Log_{10} (x) + 0.2566 with R^2 = 0.996. Each data point is an average of 6 sensors. All error bars represent ± 1 standard deviation. (c) Comparison of different amount of anti-HSA antibody used in the bio-functionalization process: 0.2 μg (■) with linear regression y = 0.0754 Log_{10} (x) + 0.209 with R^2 = 0.979 and 0.4 μg (•) with linear regression y = 0.0944 Log_{10} (x) + 0.270 with R^2 = 0.984 and 0.8 μg (▲) with linear regression y = 0.0971 Log_{10} (x) + 0.285 with R^2 = 0.981. Each data point is an average of 9 sensors. All error bars represent ± 1 standard deviation.

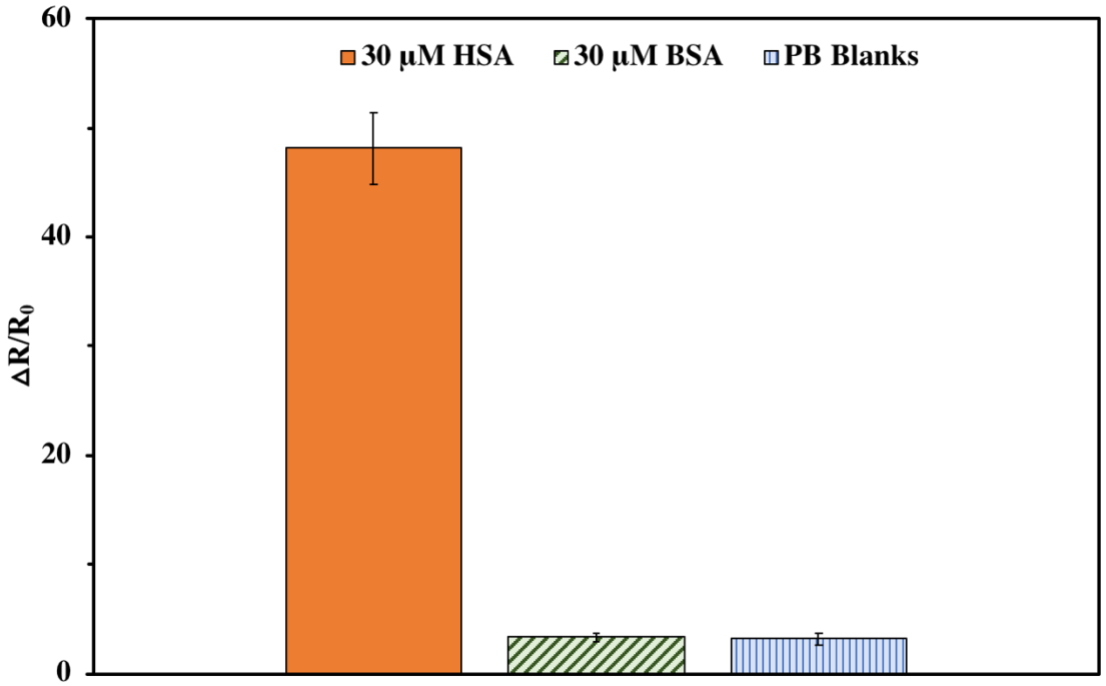

Figure 3.13 Comparison between HSA detection (solid fill) and negative control experiments: sensors functionalized with anti-HSA antibody but sensed with BSA (diagonal stripe), and sensors functionalized with anti-HSA antibody but sensed with PB blank samples (vertical stripe bar).

3.4.4 Sensing Mechanism of Paper-Based Bulk SWCNTs Network Biosensor

The sensing mechanisms of carbon nanotubes-based chemiresistive biosensors include electrostatic gating effect, changes in gate coupling, carrier mobility changes, and Schottky barrier effects[51]. SWCNTs-based field-effect transistor is usually dominated by a combination of electrostatic gating and Schottky barrier effect. In order to determine the dominating mechanism in our biosensors, we investigated the biosensor response to HSA samples in 10 mM PB at different pH values. As shown in **Figure 3.14**, the response of the biosensors reversed (i.e., there was a decrease in resistance instead of an increase) when the sample pH dropped from 7.4 to 3.5. This is in accordance with observations of Heller

et al.[51], and is attributed to the change in the net charge of protein from negative to positive when the pH changed from above to below pI value, which for HSA is 4.8.

Additionally, the magnitude of response was larger in pH 7.4 compared to 5.9 and is ascribed to the more negative charge of protein. Furthermore, it was observed that at pH 3.5 the magnitude of the response was smaller than that of pH 5.9 and is attributed to the dramatic decrease of the binding constant at pH below 4[52]. These results confirmed the dominating mechanism behind the paper-based SWCNT-chemiresistive biosensors should be the electrostatic gating effect.

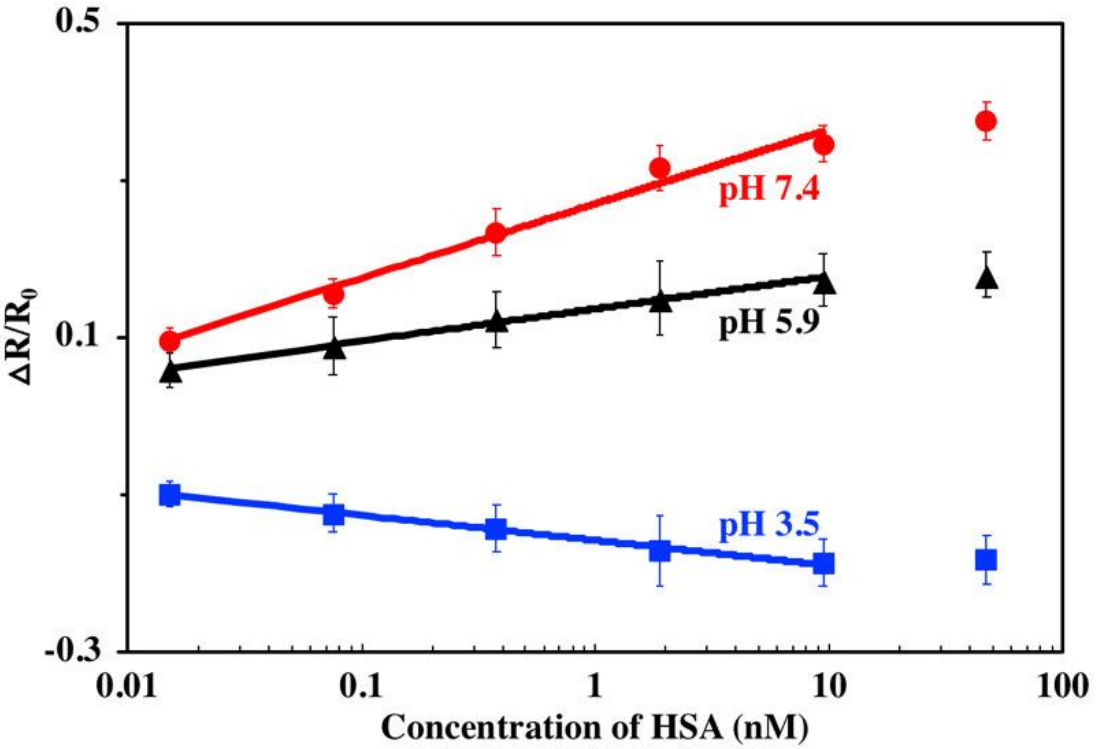

Figure 3.14 The chemiresistive responses to HSA samples at different pH values: pH 7.4 (•), pH 5.9 (▲), and pH 3.5 (■). Each data point is an average of 9 sensors and the error bars represent ± 1 standard deviation.

3.4.5 Demonstration Device for Sequential Delivery and Analyte Detection

The optimization studies conducted on laser-etched grooves[28] were used to design a fluid-handling mechanism for the chemiresistive paper-based sensor. The main goal of the fluid-handing mechanism was to sequentially deliver a sample and wash buffer to the chemiresistive sensor without any user intervention after initial depositions of fluids. In our previous report[40], both the sample and wash buffer were manually applied by pipet and removed by vacuum filtration in sequence, requiring substantial user intervention. In addition, a vacuum source might not be readily available in resource-limited or in-field settings.

As shown in **Figure 3.15a**, the location of the sample inlet provided the liquid with two possible directions to flow, either towards the etched channel to the sensor or towards a narrow channel to the wash buffer inlet. Because the grooved channel had a much lower resistance to flow, almost all the sample flowed in that direction. The grooved channel rapidly delivered the sample across the surface of the chemiresistive sensor that was positioned directly underneath. Additionally, since the grooves were slits, they allowed bulk fluid to directly contact the sensor, improving mass-transfer kinetics and reducing time required for reaching stable signals. A secondary waste pad (**Figure 3.15b iv**) sat directly below the sensor and absorbed any fluid that passed through it, reducing accumulation of 'depleted' sample fluid at the sensor surface. Excess sample also flowed into the waste-pad region at the end of the grooved channel. Since the channel was pre-saturated with fluid, the wash buffer did not start moving downstream until the sample

solution in the sample inlet was sufficiently depleted. **Figure 3.16** shows a time-lapse of the aforementioned sequential delivery step.

Since the SWCNT chemiresistor sensor is highly sensitive to its environment, priming buffer was needed to fully moisturize the sensor before sample was introduced. The assembled devices showed a stable current around 10 μA with a source-drain voltage of 0.1V, because of its initial dry resistance of 9.9 kΩ. However, the current decreased significantly upon the addition of the priming buffer (20 μL 10 mM PB, pH 7.4) due to a large addition of water molecules onto the chemiresistor (**Figure 3.15c**). Water molecules in the priming buffer n-doped the p-typed SWCNTs and thus caused the observed decrease in the current through a dramatic increase in the resistance[40,47,53]. As shown in **Figure 3.15c**, sample added after the priming process flattened the baseline current. Normalization based on the primed baseline was an essential step for reading the electrical responses. Normalized current was defined as the ratio of the raw current (I) and the current after the priming process (I_p). As shown in **Figure 3.15c**, the normalized current was, by definition, at 1.0 at the point of sample arrival and decreased as more HSA sample was delivered to the sensor. In PB at pH 7.4, HSA molecules carried a net negative charge and were specifically bound to the anti-HSA. The binding events transferred charge to the semiconducting SWCNTs. The SWCNT chemiresistive sensor responded to the charge change at the sensor's surface due to the dominating effect of electrostatic gating[40]. **Figure 3.17** contains current vs. time plots for different concentrations of HSA in PB and controls.

A linear calibration curve with a satisfactory sensitivity and specificity was obtained over a wide range between 0.015 nM and 9.47 nM. As shown in **Figure 3.15d**,

the calibration curves were graphed as $\Delta R/R_0$ vs. Log_{10}[HSA, nM], where ΔR was the difference between the steady-state resistance (R) after sample incubation and wash and the resistance R_0 after the sensor was primed (before sample addition). The response was linear with a 6.47% increase in the resistance per Log_{10}[HSA, nM]. Controls were tested by adding the same volume of PB or a non-target protein (9.47 nM human immunoglobin G (HIgG) in 10 mM PB, pH 7.4). PB alone introduced a $-$ 1.01 $\pm$ 1.1% change after normalization, while the non-target crosstalk control (HIgG) resulted in only a 0.289 $\pm$ 1.4% change. By comparing the responses from the PB blank ($\Delta R/R_0 \pm 3SD$) and the responses from 15 pM HSA in PB ($\Delta R/R_0 \pm SD$), the lowest detectable concentration of HSA in PB was 15 pM based on an S/N ratio of 3 ($p = 0.023 < 0.05$). This figure is superior to traditional HSA biosensor LODs in the milligram per milliliter or micromolar range[48,54]. These results indicated the high sensitivity and specificity of the biosensor.

Furthermore, to mimic the detection of HSA in real samples, we challenged the device with HSA samples in complex matrices, such as AU and AS. Due to the elevated level of dissolved salts in the AU and AS, the local ionic strength near the sensor surface was high and led to a minimal Debye length. Thus, it was necessary to use PB washes to dilute the local ionic solution and recover the electrical responses corresponding to the affinity-based binding between the antigen and antibody[53,55]. As shown in **Figure 3.15c**, after PB priming, the HSA sample in AU or AS matrix gave a reduced response (less decrease in the current) compared to that in HSA samples in PB. A 60 μL PB wash was used to recover the responses (more decrease in the current). The possible mechanism was that the continuous inflow of PB with low ionic strength washed the salts to the waste

layer/pad and diluted the local matrix, which resulted in a larger Debye length to overturn the charge screening and thus recovered the responses[53,55]. These observations show that a well-controlled fluid delay is an essential function for a paper-based microfluidic biosensor for more complex, real-life samples. **Figure 3.18** and **Figure 3.19** contain current vs. time plots for different concentrations of HSA in AU and AS, respectively. The viscosity of the biological samples can also affect their wicking behavior in paper (**Figure 3.20**).

Compared with our previous work[40], in which the samples and wash buffers were manually added by pipet and removed by vacuum filtration, the device presented here was ~70% as sensitive with a satisfactory lowest detectable limit of 15 pM HSA in PB. The lower sensitivity for HSA in PB in the current device compared to our prior work is likely because the latter utilized the vacuum filtration to very effectively remove excess sample and wash solution from the sensor surface after incubations. The current device also gave good sensitivities to HSA in AU and AS. The responses were linear with a 4.52% and 4.87% increase in the resistance per Log_{10}[HSA, nM] for AU and AS, respectively. However, devices tested in AU/AS had a ~ 25% – 30% lower sensitivity compared to devices tested with PB only. The lower sensitivities for HSA in AU and AS were likely because the washing process is even more critical for samples containing ions and other interfering substances. It is expected that the sensitivities can be improved with the revision of the device design to allow for a larger wash buffer volume, which is currently limited to 60 μL. Nevertheless, the sensor still maintained good sensitivity and specificity to HSA. Furthermore, with the new fluid-handling architecture, external devices such as a vacuum filter and a vacuum pump are no longer necessary. The fluid-handling layer was able to

semi-automatically deliver the fluids sequentially to the SWCNT chemiresistor, thus eliminating the need for specialized personnel.

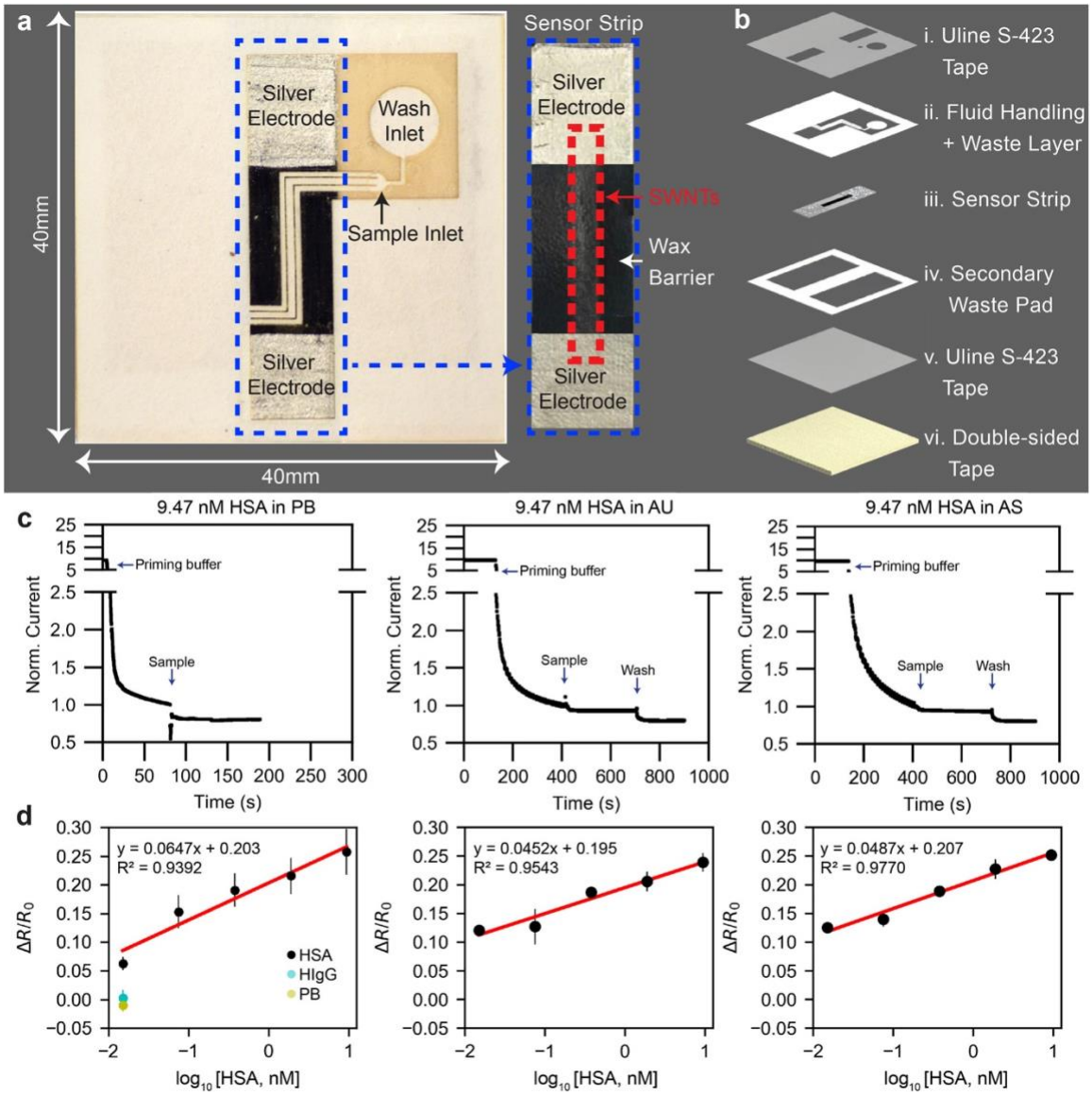

Figure 3.15 Overall design and demonstration of the paper-based chemiresistive sensor device. (a) Images of the assembled multi-layer device (left) and the sensor strip inside (right). (b) Schematic of the multi-layer assembly, showing the fluid-handling layer, the chemiresistive sensor strip, and the other layers. (c) Current response for a fixed concentration of HSA (9.47 nM) in PB, AU and AS. Current is normalized with respect to the current after priming. Plots for both artificial biological fluids show the need for a washing step for signal recovery compared to PB. (d) Calibration plot of normalized change in resistance for each fluid type. Data presented as mean ± SD. N = 3.

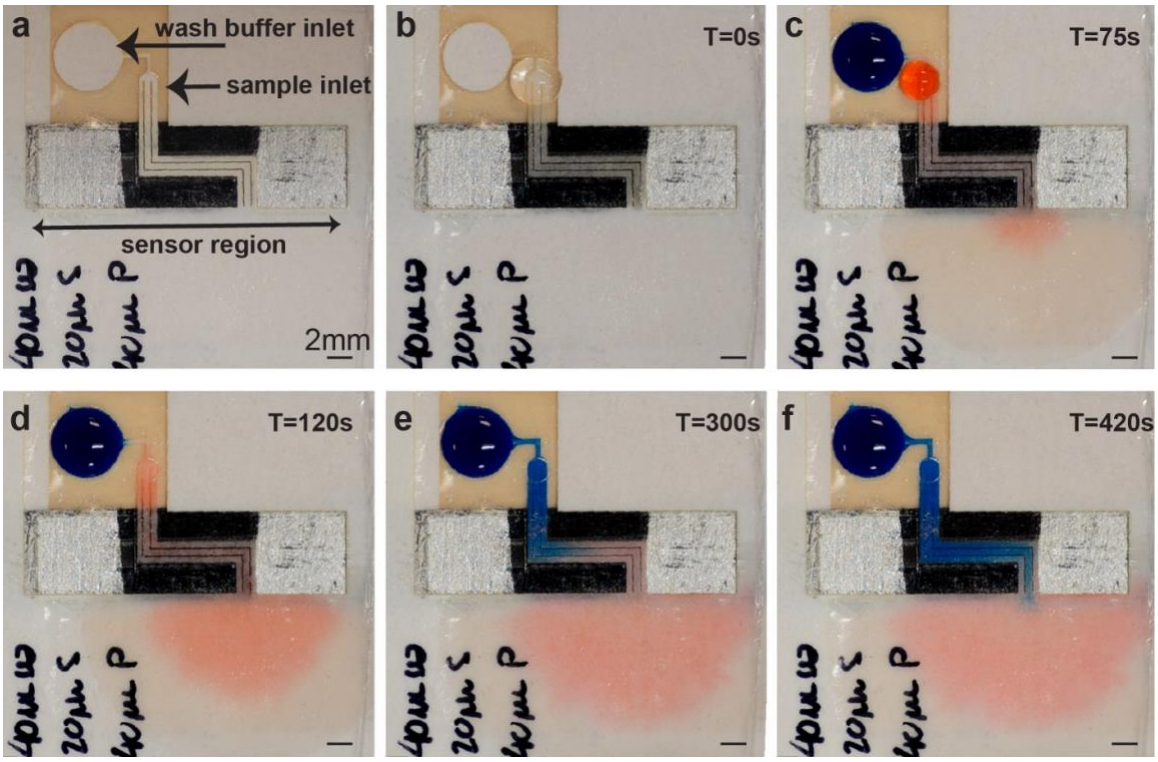

Figure 3.16 Time-lapse of sequential fluid delivery in the paper-based chemiresistive sensor device (a). After a priming buffer was added to the channel (b), a sample and wash buffer were simultaneously deposited (red and blue dye respectively) (c). The grooves in the channel drove the sample towards the sensor rather than towards the wash buffer (d). The presence of the sample droplet prevented the dye from wicking until the sample was completely gone (e). After that, the wash buffer flowed across the sensor (f). Scale bar = 2 mm.

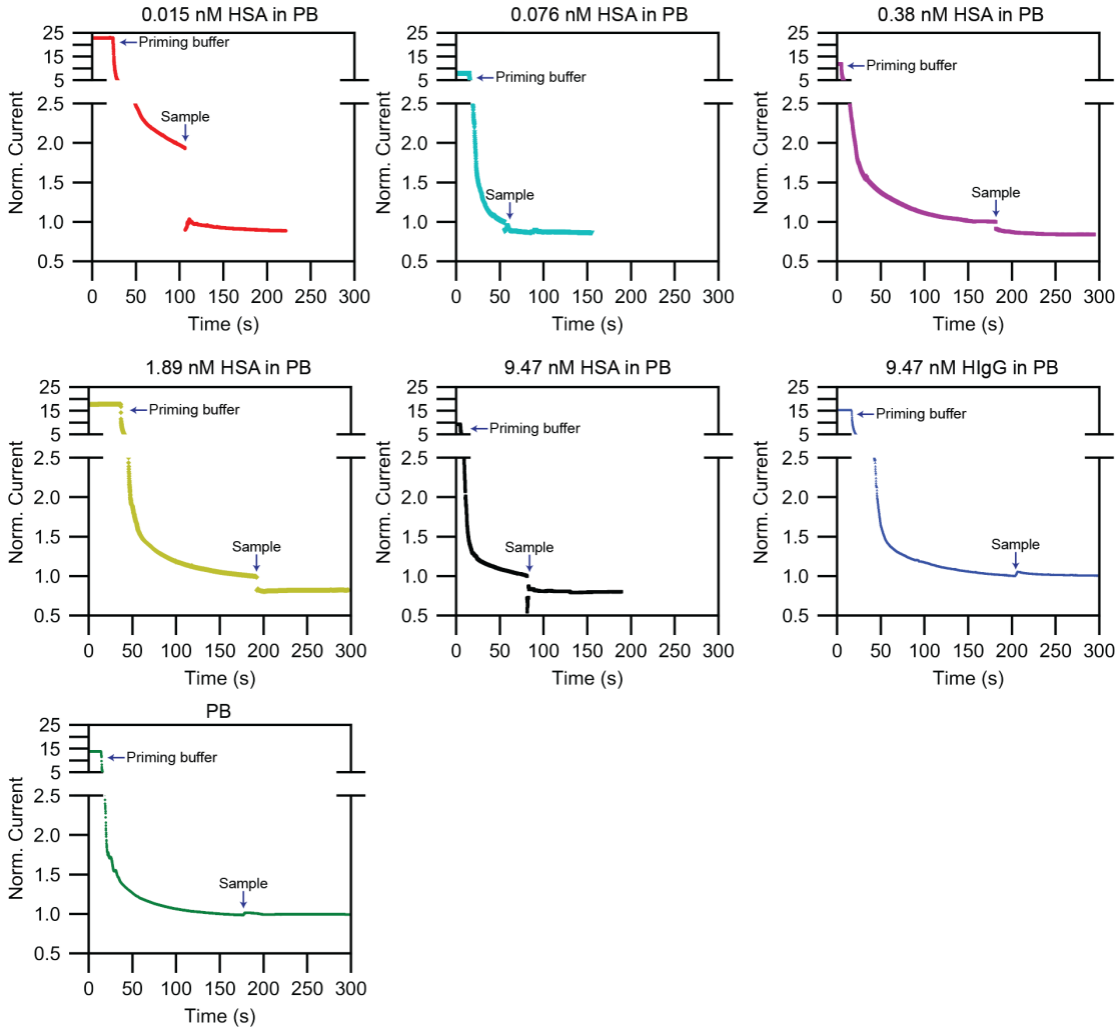

Figure 3.17 Normalized current vs. time plots for different concentrations of HSA in PB and controls. Controls consisted of PB with no sample and 9.47 nM HIgG in PB. After a priming buffer was added to the channel, a sample was deposited. The grooves in the channel drove the sample towards the sensor rapidly and distributed it over the surface of the sensor.

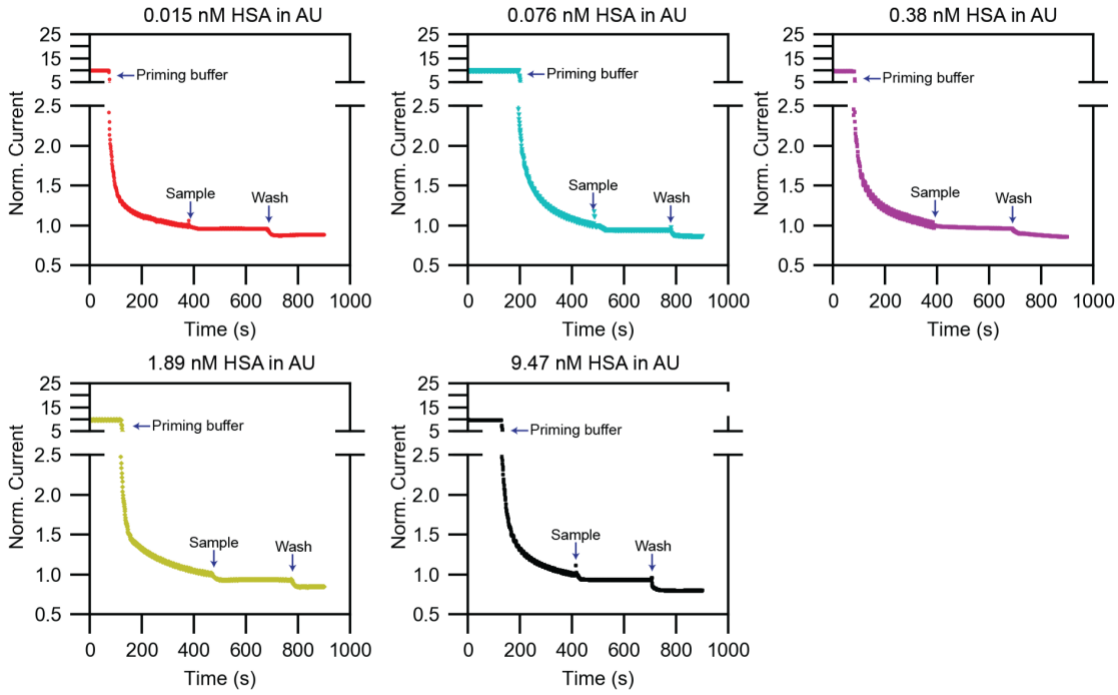

Figure 3.18 Normalized current vs. time plots for different concentrations of HSA in artificial urine (AU). After a priming buffer was added to the channel, a sample and wash buffer were deposited. The grooves in the channel drove the sample/wash buffer towards the sensor rapidly and distributed it over the surface of the sensor. The wash buffer is needed to recover sensitivity when using AU.

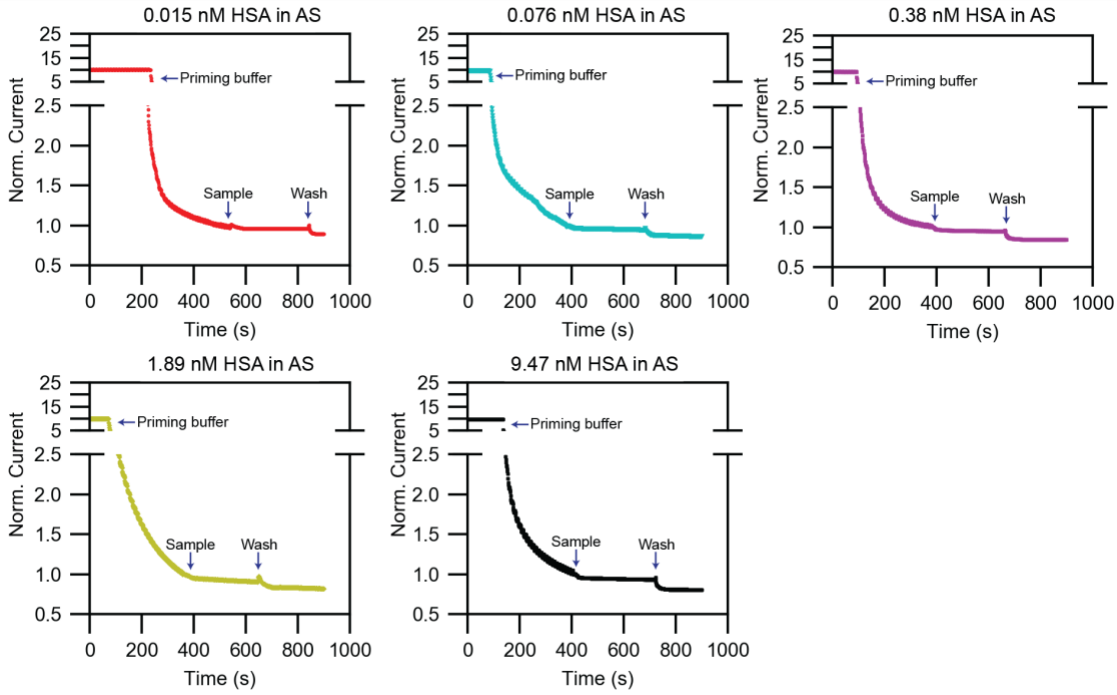

Figure 3.19 Normalized current vs. time plots for different concentrations of HSA in artificial saliva (AS). After a priming buffer was added to the channel, a sample and wash buffer were deposited. The grooves in the channel drove the sample/wash buffer towards the sensor rapidly and distributed it over the surface of the sensor. The wash buffer is needed to recover sensitivity when using AS.

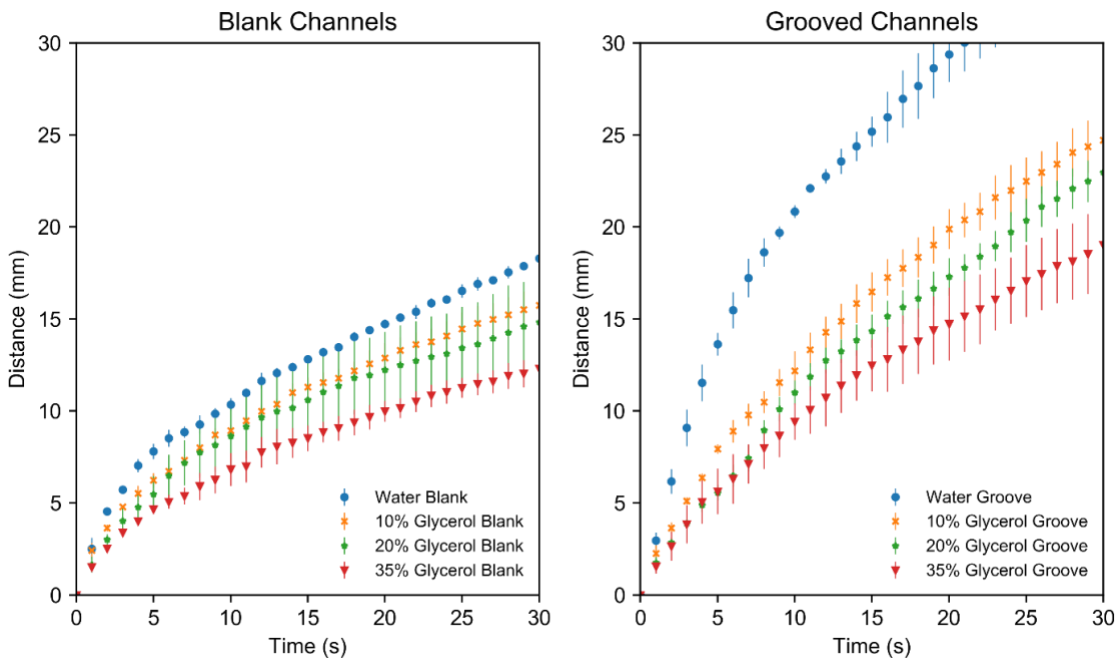

Figure 3.20 Distance vs. time plots for blank and 20%-etched channels imbibing DI H2O, 10%, 20% and 35% v/v glycerol solutions. All channels were sealed on both sides with Uline S-423 Industrial Tape. Increasing the viscosity of the fluid had a dramatic effect on the performance of the channels. This highlights the importance of taking fluid viscosity into consideration when designing paper-based devices. Data presented as mean ± SD. N = 3.

3.5 Conclusions

In conclusion, this study presents a low cost, yet highly sensitive SWCNTs-based chemiresistive biosensor on paper. The biosensor is fabricated using a facile maskless method of combining wax printing and vacuum filtering of water-based high concentration (4 mg/mL) and stable (up to one month under ambient conditions) SWCNTs ink on the sensing channel followed by covalent biofunctionalization with biorecognition molecule. With optimizations of the washing mode and the anti-HSA loading, detection of as low as 1 pM HSA with high selectivity was achieved with our paper-based biosensor.

This study verified the feasibility of the paper-based chemiresistor biosensor architecture with the proposed vertical-microfluidic channel. Furthermore, the synthesized water-based ink will be compatible with a spectrum of other instrumentation for chemiresistor biosensor fabrication since water is more instrument-friendly. The simple maskless method of wax printing and vacuum filtration will further ease the instrumental burden of traditional microfluidic channel fabrication on paper.

As a proof of concept, we successfully demonstrated the utility of laser-etched grooves by enabling rapid, semi-automated sequential fluid delivery for a chemiresistive SWCNT paper-based sensor targeting HSA in PB, AU, and AS. Furthermore, it is expected that by combining etching with other fluid control strategies, such as delay shunts or multilayer channels, a much higher degree of wicking control can be available for more complicated point-of-care devices.

Collectively, this work provides a potential platform for future automated, disposable paper-based biosensors with multiplexed detection capability and self-driven microfluidic controls towards meeting “ASSURED” (i.e. Affordable, Sensitive, Specific, User-friendly, Rapid and robust, Equipment-free, Deliver to the users who need them) criteria sought for diagnostics technologies in resource limited environment.

3.6 References

1. Lee, W. G., Kim, Y.-G., Chung, B. G., Demirci, U. & Khademhosseini, A. Nano/Microfluidics for diagnosis of infectious diseases in developing countries. *Adv. Drug Deliv. Rev.* **62**, 449–457 (2010).

2. Yager, P. *et al.* Microfluidic diagnostic technologies for global public health. *Nature* **442**, 412 (2006).

3. Hu, J. *et al.* Advances in paper-based point-of-care diagnostics. *Biosens. Bioelectron.* **54**, 585–597 (2014).

4. Foster, L. S. & Gruntfest, I. J. Demonstration experiments using universal indicators. *J. Chem. Educ.* **14**, 274 (1937).

5. Martinez, A. W., Phillips, S. T., Butte, M. J. & Whitesides, G. M. Patterned paper as a platform for inexpensive, low-volume, portable bioassays. *Angew. Chemie Int. Ed.* **46**, 1318–1320 (2007).

6. Cheng, C. *et al.* Paper-based ELISA. *Angew. Chemie Int. Ed.* **49**, 4771–4774 (2010).

7. Hsu, C.-K. *et al.* Paper-Based ELISA for the Detection of Autoimmune Antibodies in Body Fluid—The Case of Bullous Pemphigoid. *Anal. Chem.* **86**, 4605–4610 (2014).

8. Nie, Z. *et al.* Electrochemical sensing in paper-based microfluidic devices. *Lab Chip* **10**, 477–483 (2010).

9. Sarfraz, J., Tobjork, D., Osterbacka, R. & Linden, M. Low-cost hydrogen sulfide gas sensor on paper substrates: fabrication and demonstration. *IEEE Sens. J.* **12**, 1973–1978 (2011).

10. Nery, E. W. & Kubota, L. T. Sensing approaches on paper-based devices: a review. *Anal. Bioanal. Chem.* **405**, 7573–7595 (2013).

11. Hossain, S. M. Z. & Brennan, J. D. β-Galactosidase-based colorimetric paper sensor for determination of heavy metals. *Anal. Chem.* **83**, 8772–8778 (2011).

12. Ge, L., Wang, S., Song, X., Ge, S. & Yu, J. 3D origami-based multifunction-integrated immunodevice: Low-cost and multiplexed sandwich chemiluminescence immunoassay on microfluidic paper-based analytical device. *Lab Chip* **12**, 3150–3158 (2012).

13. Nie, Z., Deiss, F., Liu, X., Akbulut, O. & Whitesides, G. M. Integration of paper-based microfluidic devices with commercial electrochemical readers. *Lab Chip* **10**, 3163–3169 (2010).

14. Tang, R., Shi, Y., Hou, Z. & Wei, L. Carbon nanotube-based chemiresistive sensors. *Sensors* **17**, 882 (2017).

15. Park, M., Cella, L. N., Chen, W., Myung, N. V & Mulchandani, A. Carbon nanotubes-based chemiresistive immunosensor for small molecules: Detection of nitroaromatic explosives. *Biosens. Bioelectron.* **26**, 1297–1301 (2010).

16. Rajesh *et al.* Label-free detection of cardiac troponin-I using gold nanoparticles functionalized single-walled carbon nanotubes based chemiresistive biosensor. *Appl. Phys. Lett.* **103**, 203703 (2013).

17. Tan, F., Saucedo, N. M., Ramnani, P. & Mulchandani, A. Label-free electrical immunosensor for highly sensitive and specific detection of microcystin-LR in water samples. *Environ. Sci. Technol.* **49**, 9256–9263 (2015).

18. Martinez, A. W., Phillips, S. T., Whitesides, G. M. & Carrilho, E. Diagnostics for the developing world: microfluidic paper-based analytical devices. *Anal. Chem.* **82**, 3–10 (2009).

19. Dungchai, W., Chailapakul, O. & Henry, C. S. A low-cost, simple, and rapid fabrication method for paper-based microfluidics using wax screen-printing. *Analyst* **136**, 77–82 (2011).

20. Nurak, T., Praphairaksit, N. & Chailapakul, O. Fabrication of paper-based devices by lacquer spraying method for the determination of nickel (II) ion in waste water. *Talanta* **114**, 291–296 (2013).

21. Lei, K. F., Yang, S.-I., Tsai, S.-W. & Hsu, H.-T. Paper-based microfluidic sensing device for label-free immunoassay demonstrated by biotin–avidin binding interaction. *Talanta* **134**, 264–270 (2015).

22. Abe, K., Suzuki, K. & Citterio, D. Inkjet-printed microfluidic multianalyte chemical sensing paper. *Anal. Chem.* **80**, 6928–6934 (2008).

23. Lu, Y., Shi, W., Qin, J. & Lin, B. Fabrication and characterization of paper-based microfluidics prepared in nitrocellulose membrane by wax printing. *Anal. Chem.* **82**, 329–335 (2009).

24. Dungchai, W., Chailapakul, O. & Henry, C. S. Electrochemical detection for paper-based microfluidics. *Anal. Chem.* **81**, 5821–5826 (2009).

25. Bruzewicz, D. A., Reches, M. & Whitesides, G. M. Low-cost printing of poly (dimethylsiloxane) barriers to define microchannels in paper. *Anal. Chem.* **80**, 3387–3392 (2008).

26. Lee, C.-Y., Lei, K. F., Tsai, S.-W. & Tsang, N.-M. Development of graphene-based sensors on paper substrate for the measurement of pH value of analyte. *BioChip J.* **10**, 182–188 (2016).

27. Carrilho, E., Martinez, A. W. & Whitesides, G. M. Understanding wax printing: a simple micropatterning process for paper-based microfluidics. *Anal. Chem.* **81**, 7091–7095 (2009).

28. Modha, S., Shen, Y., Chamouni, H., Mulchandani, A. & Tsutsui, H. Laser-etched grooves for rapid fluid delivery for a paper-based chemiresistive biosensor. *Biosens. Bioelectron.* **180**, 113090 (2021).

29. Elizalde, E., Urteaga, R. & Berli, C. L. A. Rational design of capillary-driven flows for paper-based microfluidics. *Lab Chip* **15**, 2173–2180 (2015).

30. Castro, C., Rosillo, C. & Tsutsui, H. Characterizing effects of humidity and channel size on imbibition in paper-based microfluidic channels. *Microfluid. Nanofluidics* **21**, 21 (2017).

31. Jahanshahi-Anbuhi, S. *et al.* Paper-based microfluidics with an erodible polymeric bridge giving controlled release and timed flow shutoff. *Lab Chip* **14**, 229–236 (2014).

32. da Silva, E. T. S. G., Santhiago, M., de Souza, F. R., Coltro, W. K. T. & Kubota, L. T. Triboelectric effect as a new strategy for sealing and controlling the flow in paper-based devices. *Lab Chip* **15**, 1651–1655 (2015).

33. Camplisson, C. K., Schilling, K. M., Pedrotti, W. L., Stone, H. A. & Martinez, A. W. Two-ply channels for faster wicking in paper-based microfluidic devices. *Lab Chip* **15**, 4461–4466 (2015).

34. Channon, R. B. *et al.* Rapid flow in multilayer microfluidic paper-based analytical devices. *Lab Chip* **18**, 793–802 (2018).

35. Kalish, B., Tan, M. K. & Tsutsui, H. Modifying wicking speeds in paper-based microfluidic devices by laser-etching. *Micromachines* **11**, 773 (2020).

36. Renault, C., Li, X., Fosdick, S. E. & Crooks, R. M. Hollow-channel paper analytical devices. *Anal. Chem.* **85**, 7976–7979 (2013).

37. Giokas, D. L., Tsogas, G. Z. & Vlessidis, A. G. Programming fluid transport in paper-based microfluidic devices using razor-crafted open channels. *Anal. Chem.* **86**, 6202–6207 (2014).

38. Shin, J.-H., Lee, G.-J., Kim, W. & Choi, S. A stand-alone pressure-driven 3D microfluidic chemical sensing analytic device. *Sensors Actuators B Chem.* **230**, 380–387 (2016).

39. Liu, Q., Xu, C. & Liang, H. Laser carved micro-crack channels in paper-based dilution devices. *Talanta* **175**, 289–296 (2017).

40. Shen, Y., Tran, T.-T., Modha, S., Tsutsui, H. & Mulchandani, A. A paper-based chemiresistive biosensor employing single-walled carbon nanotubes for low-cost, point-of-care detection. *Biosens. Bioelectron.* **130**, 367–373 (2019).

41. Brooks, T. & Keevil, C. W. A simple artificial urine for the growth of urinary pathogens. *Lett. Appl. Microbiol.* **24**, 203–206 (1997).

42. Tlili, C., Cella, L. N., Myung, N. V, Shetty, V. & Mulchandani, A. Single-walled carbon nanotube chemoresistive label-free immunosensor for salivary stress biomarkers. *Analyst* **135**, 2637–2642 (2010).

43. Brown, S. D. M., Jorio, A., Dresselhaus, M. S. & Dresselhaus, G. Observations of the D-band feature in the Raman spectra of carbon nanotubes. *Phys. Rev. B* **64**, 73403 (2001).

44. Simmons, T. J., Bult, J., Hashim, D. P., Linhardt, R. J. & Ajayan, P. M. Noncovalent functionalization as an alternative to oxidative acid treatment of single wall carbon nanotubes with applications for polymer composites. *ACS Nano* **3**, 865–870 (2009).

45. Zhang, T. *et al.* Poly (m-aminobenzene sulfonic acid) functionalized single-walled carbon nanotubes based gas sensor. *Nanotechnology* **18**, 165504 (2007).

46. Kong, J. *et al.* Nanotube molecular wires as chemical sensors. *Science (80-.).* **287**, 622–625 (2000).

47. Han, J.-W., Kim, B., Li, J. & Meyyappan, M. Carbon nanotube based humidity sensor on cellulose paper. *J. Phys. Chem. C* **116**, 22094–22097 (2012).

48. Choi, S., Choi, E. Y., Kim, H. S. & Oh, S. W. On-site quantification of human urinary albumin by a fluorescence immunoassay. *Clin. Chem.* **50**, 1052–1055 (2004).

49. Ogata, A. F. *et al.* Virus-Enabled Biosensor for Human Serum Albumin. *Anal. Chem.* **89**, 1373–1381 (2017).

50. Tsai, J.-Z. *et al.* Screen-printed carbon electrode-based electrochemical immunosensor for rapid detection of microalbuminuria. *Biosens. Bioelectron.* **77**, 1175–1182 (2016).

51. Heller, I. *et al.* Identifying the mechanism of biosensing with carbon nanotube transistors. *Nano Lett.* **8**, 591–595 (2008).

52. Sada, E., Katoh, S., Sukai, K., Tohma, M. & Kondo, A. Adsorption equilibrium in immuno-affinity chromatography with polyclonal and monoclonal antibodies. *Biotechnol. Bioeng.* **28**, 1497–1502 (1986).

53. Shen, Y., Modha, S., Tsutsui, H. & Mulchandani, A. An origami electrical biosensor for multiplexed analyte detection in body fluids. *Biosens. Bioelectron.* **171**, 112721 (2021).

54. Aliño, V. J. & Yang, K.-L. Using liquid crystals as a readout system in urinary albumin assays. *Analyst* **136**, 3307–3313 (2011).

55. Kaisti, M. Detection principles of biological and chemical FET sensors. *Biosens. Bioelectron.* **98**, 437–448 (2017).

Chapter 4. Development of Ultrasensitive Single-Walled Carbon Nanotubes-Based Chemiresistive Biosensors on Origami Microfluidics for Multiplexed Detections of Protein Biomarkers

This chapter is based on, or in part a reprint of the material as it appears in Shen, Y., Modha, S., Tsutsui, H., & Mulchandani, A. (2021). An origami electrical biosensor for multiplexed analyte detection in body fluids. *Biosensors and Bioelectronics*, 171, 112721.

4.1 Abstract

We developed an affordable, highly sensitive, and specific paper-based microfluidic platform for fast multiplexed detections of important biomarkers in various body fluids, including urine, saliva, serum, and whole blood. The sensor array consisted of five individual sensing channels with various functionalities that only required a micro liter-sized sample, which was equally split into aliquots by the built-in paper microfluidics. We achieved the individual functionalizations of various bioreceptors by employing the use of wax barriers and 'paper bridges' in an easy and low-cost manner. Pyrene carboxylic acid-modified single-walled carbon nanotubes (PCA/SWCNTs) were deposited by quantitative inkjet printing with an optimal 3-dimensional semiconductor density on a paper substrate. Multiple antibodies were immobilized onto the SWCNTs surface for highly sensitive and specific field- effect transistor (FET)/chemiresistor (CR) biosensors. We explored the optimal sensing conditions for the paper- based CR biosensor to achieve high sensitivities and specificities towards the target biomarker proteins (human serum

albumin (HSA) and human immunoglobulin G (HIgG)) and achieved an ultralow detectable concentration of HSA and HIgG at 1.5 pM. Besides, origami folding was employed to simplify the fabrication process further. The sensing platform described in this work was cost-effective, semi-automated, and user-friendly. It demonstrated the capability of having multiple sensing functions in one paper-based microfluidic sensing platform. It envisioned the potential of a point-of-care device with full-analysis for practical diagnostics in an ASSURED (**a**ffordable, **s**ensitive, **s**pecific, **u**ser-friendly, **r**apid and robust, **e**quipment-free and **d**eliverable to end-users) fashion for a quick test of targets of interest.

4.2 Introduction

Many efforts have been made towards developing diagnostic devices that meet the ASSURED criteria of being affordable, sensitive, specific, user-friendly, rapid and robust, equipment-free, and deliverable-to- those-who-need-it[1]. Given that over 95% of the deaths in low-income countries are due to major infectious diseases and cancers, early diagnosis is of great importance to the overall health of human beings[2]. Point-of-care (POC) diagnostic devices using low-cost substrates and easy fabrication methods are being extensively studied. Paper exhibits great advantages beyond other polymer-based flexible substrate materials[3–7] for being low-cost with intrinsic capillary microfluidics, easily disposable and biocompatible, requiring no external pumps, low-instrumentation and easy-to-assemble. Therefore, paper has become a popular substrate to build ASSURED biosensing platforms[8–11].

Paper-based biosensors using colorimetric/chemiluminescence and electrochemical detection with pre-deposited reagents and automated or semi-automated microfluidics have been widely explored[9,12–17]. Nevertheless, many colorimetric devices are primarily qualitative, while the ones that are quantitative have a poor limit of detection (LOD) in the micromolar or millimolar ranges[15], require special cameras or scanners to capture the light intensities[18], and often necessitate a fixed lighting environment for accurate measurements[19]. Electrochemical biosensors, on the other hand, require bulky liquid reservoirs for the redox reaction to occur as well as employment of multiple antibodies (capture antibodies and reporter probe antibodies) and labels (enzymes, dyes, nanoparticles, etc.) for complicated sandwich assays[20]. Current label-based immunoassays are limited by the lack of an ideal label that is compatible with all potential target analytes, the inability to achieve LOD at nanomolar to attomolar levels, and the long assay time. As such, label-free immuno-nanosensors are an active research subject. Compared to the previously developed technologies, the label-free field-effect transistor (FET)/chemiresistor (CR)-based biosensors are more appealing in providing high sensitivities and selectivities for target biomarkers[21,22].

Owing to their intriguing physical, chemical, and electrical proper- ties, carbon-based nanomaterials have emerged as potential candidates for the development of next-generation miniaturized biosensors[22–24]. Single-walled carbon nanotubes (SWCNTs) have been employed extensively as transducer elements in FET/CR sensors due to their high surface-to-volume ratio, which causes the Debye length (λ_D), a measure of electric field penetration into a bulk material, to be comparable to the dimensions of these

nanostructures[22]. This leads to significant modulations of their electronic properties upon exposure to chemicals, enabling the label-free detection of analytes with higher sensitivities and lower LODs. Moreover, SWCNTs FETs/CRs can be integrated with modern microelectronics in multifunctional devices that detect multiple analytes simultaneously[25]. Thus, SWCNTs are the promising semiconducting transducer material to fabricate FET/CR biosensors in this work. Methods to fabricate paper-based microfluidic channels range from sophisticated photolithography to facile printing methods[26]. However, the high cost of the toxic reagents/solvents of most fabrication methods of paper-based microfluidics still poses a challenge to fabricating a well-defined biosensor array on a porous paper substrate with high sensitivity and specificity to conduct multi-analyte detection with minimal sample requirements. On the other hand, wax printing shows several merits such as (1) a simple fabrication process of printing and baking with adequate pattern resolutions, (2) rapid fabrication in minutes, (3) low cost (easy to obtain paper and wax), (4) environment-friendly (no organic solvents), and (5) ease of disposal after use by incineration[11]. Hence, wax printing is employed in this work to build the multiplexed paper microfluidic channels in a facile and economic manner.

Herein, we present a new biosensing platform featuring a paper- based microfluidic FET/CR array for highly sensitive and selective multiplexed detections of important biomarkers in body fluids.

4.3 Materials and Methods

4.3.1 Inkjet Printing Fabrication of Paper-Based SWCNTs CR Array

DMP-2831 inkjet printer (FUJIFILM Dimatix, Inc.) was used to print the conductive silver leads (Metalon JS-B25P, NovaCentrix, Inc.) and pyrene carboxylic acid (PCA)-modified SWCNTs, from now-on designated as PCA/SWCNTs. Cellulose paper (Whatman Grade 1 chromatography paper, 20 cm by 20 cm) was used as the substrate for depositing the sensor arrays. Drop spacing was 20 μm and droplet speed was 6 – 8 m/s. Wax patterns were designed using GNU Image Manipulation Program (GIMP) software and exported as TIFF files. Xerox ColorQube 8880DN was used to print wax barriers on paper substrate. The paper bridge patterns were printed on another piece of paper and cut into rings afterward as separate pieces of paper bridges. All wax patterns were baked at 170 ˚C for 5 min to ensure wax penetrated the full thickness of the paper substrate.

The commercial silver nanoparticle ink (Metalon JS-B25P) was loaded into the inkjet printer cartridge with the built-in Drop Watcher to check the inkjet printing quality. The temperature for all settings was maintained at room temperature except the platen temperature was 60 ˚C for silver inkjet printing to ensure fast evaporation of the solvent and thus reducing the lateral spreading of the silver prints. With the drop spacing of 20 μm and the average jetting voltage of 35 ± 1 V, silver nanoparticles were printed on the paper to form the conductive leads design. The silver on paper was annealed at 200 ˚C for 2h to remove the polymer additives and solvent completely. To investigate the effect of baking/annealing on the paper capillary flow, we prepared identical 2 mm wide by 25 mm long paper strips of untreated paper and baked paper (200 ˚C, 2h) and used deionized water

for the wicking process. The result showed that the fluid arrival time for baked channel was 119.0 ± 11.9 seconds (N = 30), which was about 8% slower than the untreated paper channels (110.1 ± 10.3 seconds, N = 30).

4.3.2 Formulation and Inkjet Printing of PCA/SWCNTs Ink & NO_2 Gas Sensing

We used the commercial SWCNTs from Carbon Solutions, Inc (P3-SWCNT, CA, USA) as the starting material with following characteristics: semiconducting to metallic SWCNTs ratio: 2:1; typical individual SWCNT diameter: 1.55 ± 0.1 nm; typical bundle length: 0.5 – 1.5 μm and a typical bundle diameter: 4 – 5 nm (https://carbonsolution.com/faq). The water-based PCA/SWCNT ink was synthesized as reported[11] and diluted to ~ 0.1 mg/mL to avoid clogging the nozzles. Briefly, 50 mg SWCNTs powder and 25 mg PCA were dispersed in 25 mL DMF individually. Twenty minutes of ultra-sonication ensured good dispersion of SWCNTs in DMF. SWCNTs/DMF and PCA/DMF were well mixed with stirring for 12 h to achieve complete the π-π stacking interaction. The mixture was then vacuum filtered by PTFE membranes to accumulate a wet cake of PCA/SWCNTs. Consecutive washes with methanol and deionized water removed excessive PCA and solvent. The PCA/SWCNTs was collected and weighted carefully before redispersion in Milli-Q water to obtain a desired concentration.

For the purpose of inkjet printing, the abovementioned PCA/SWCNTs solution were diluted with methanol and ethanol with the volume ratio of 3:2:1 to reduce the surface tension for inkjet printing with a final solid concentration of PCA/SWCNTs ink at around

0.1 mg/mL. 5 min of 3500 rpm centrifuge was necessary before loading to the inkjet cartridge to reduce nozzle clogging.

The DMP-2831 built-in cleaning cycles and additional sonication of the nozzles helped reduce the clogging problems. Waveform must be adjusted to establish repeatable, well-aligned, and fast droplet jetting with a speed of 6 to 8 m/s. Drop Watcher was used to confirm the proper jetting behavior of the PCA/SWCNT ink. The temperatures of the platen and the cartridge printing head were room temperature.

With the increasing number of printing layers, SWCNT networks with increasing density were built on the porous paper substrate. We exposed the SWCNT chemiresistor to a series of increasing concentrations of NO_2 diluted in N_2 gas and monitored the resistance change with Keithley source meter (Model 2636) at room temperature. The gas sensing set-up is illustrated in **Figure 4.1**. By reviewing the sensitivities of SWCNT with various network density to NO_2 gas adsorption, an optimal SWCNTs density, and thus an optimal number of printing layers, was determined for further bio-functionalization.

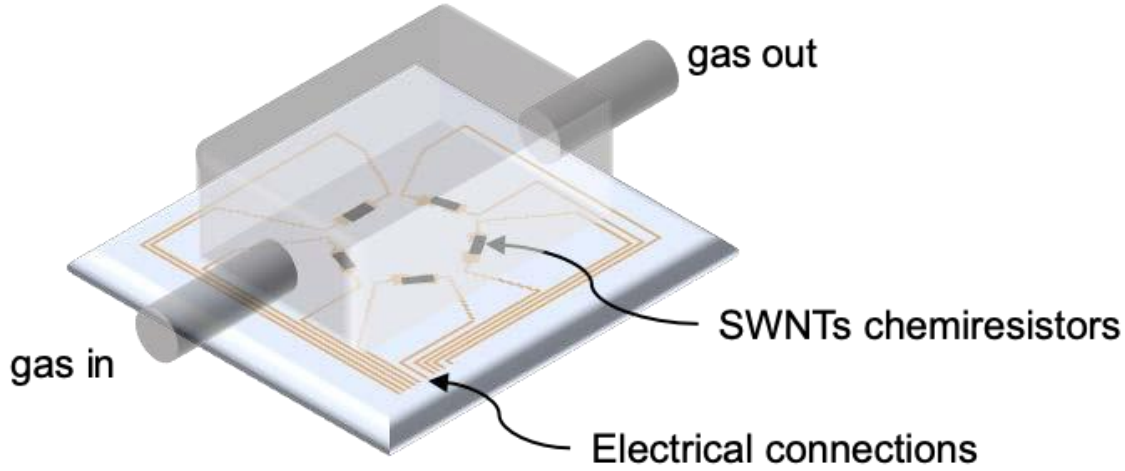

Figure 4.1 Illustration of the gas sensing set-up. Gas cylinders, gas mixers, mass flow controllers were used to supply the gas flow.

4.3.3 BSA Blocking

Bovine Serum Albumin (BSA) was used as a blocking agent for the non-specific binding sites of the porous cellulose paper. For one piece of 20cm-by-20cm Whatman grade 1 paper, 100 mL of 10 mg/mL of BSA in 10 mM phosphate buffer saline (pH 7.4) were used to submerge the paper channels for at least 6 hours. The non-specific adsorption of the porous paper was blocked by BSA adsorption. At least three times of 50 mL of deionized water was used to wash the excessive BSA.

Then the paper was naturally dried and kept flat under ambient condition. We collected the washes and monitored the concentrations of the BSA getting washed. As shown in **Figure 4.2**, excessive free BSA were washed thoroughly after 3 washes and subsequent final 50 mL 10 mM PB wash was executed to confirm that the adsorbed BSA was bound and non-removable during the sensing process.

The concentrations of BSA in the washes were measured by the Bradford protein assay. By the standard protocol for the Bradford protein assay (Bradford Reagent B6919, Sigma-Aldrich, St Louis, MO, USA), we observed the BSA concentration decayed using the microtiter plate reader (BioTek Gen 5, v1.06, Winooski, VT, USA). As shown in **Figure 4.2**, the normalized concentrations (normalized to the 10 mg/mL BSA) declined with increasing cycles of washes. After 3 washes, most of the free BSA were removed from the paper substrate, further wash 4 to wash 6 only resulted in less than 0.82% removal of the unbound BSA. Thus, we concluded that at least three washes were required to remove the free BSA molecules.

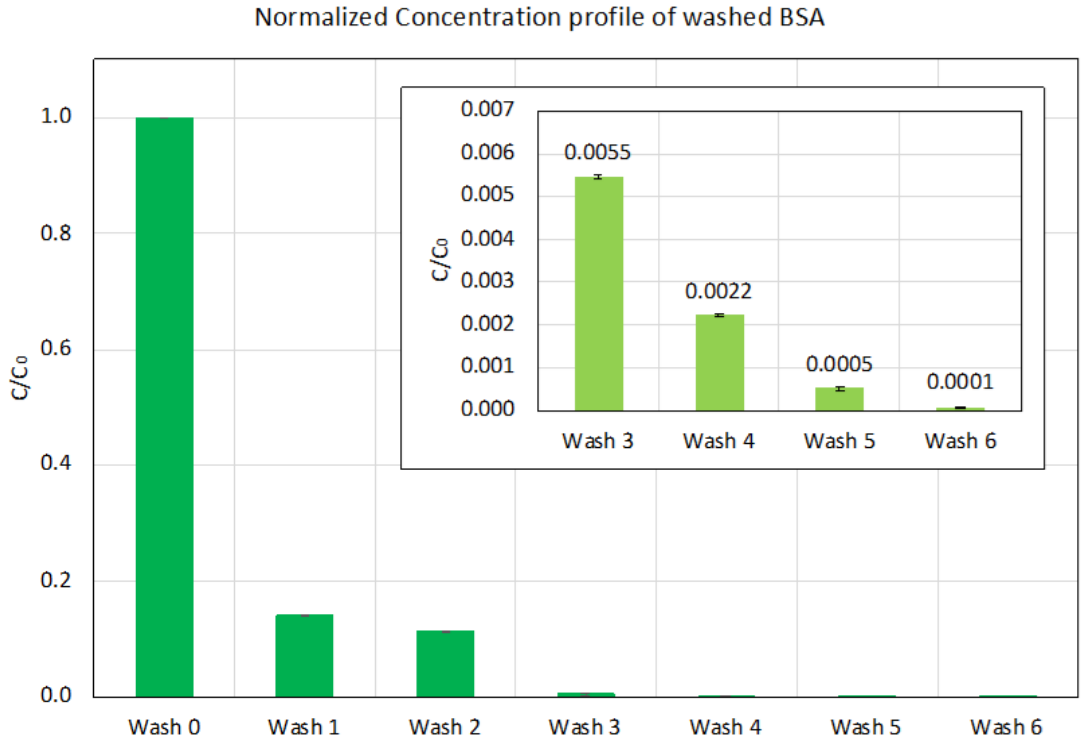

Figure 4.2 Normalized concentrations of BSA in each wash cycle. Error bars represents ± 1 standard deviation for three replicas. Each wash cycle used 50 mL 10 mM PB (pH 7.4) with respect to one 20 cm by 20 cm paper substrate.

4.3.4 Functionalization of SWCNTs CRs

All functionalization steps were done at room temperature, and all reagents were purchased from Sigma-Aldrich unless noted otherwise. Monoclonal anti-human serum albumin (HSA) and anti-human immunoglobulin G (HIgG) antibodies were purchased from Medix Biochemica (6502 SP-2) and Sigma-Aldrich (I6260), respectively. The PCA/SWCNTs CRs were submerged in 0.1 M MES buffer (pH 5.5) containing N-(3-Dimethylaminopropyl)-N′-ethylcarbodiimide (EDC) at 5 mM and N- Hydroxysuccinimide (NHS) at 2.5 mM for 20 min, followed by rinsing with phosphate buffer (PB), 10 mM at pH 7.4 unless otherwise specified, and tapped dry. In sequence, 20 µL of 50 µg/mL of each

antibody in PB, 10 μL of 0.1 M ethanolamine in PB, and 10 μL of 0.1 wt% Tween-20 in PB were added to each sensing sites and incubated individually at room temperature for 2 h, 15 min, and 30 min, respectively, followed by PB wash and tapped dry the paper surface after each incubation step.

4.3.5 Device Assembly, Sample Preparation and Electrical Measurement

From top to bottom, single-sided tape with an inlet hole, paper bridges, sensing layer, absorption layer, and sealing tape were assembled. With the absorbing pad (Whatman chromatography paper Grade 1) underneath the sensing pad, including the 5-petal pattern and the paper bridges, two pieces of single-sided transparent tape (ULINE S-423), one of which had a cut-out hole as the sample inlet in the top layer, were used to sandwich the absorbing layer and aligned sensing layers to seal the device. For origami device assembly, similar protocols were conducted except that the alignment and stacking were much easier since the patterns were precisely cut, and the connected layers facilitated the alignment between multiple paper layers. The assembled paper-based sensor arrays were stored in full humidity at 4 °C or room temperature for the stability tests. The assembled devices were stored with full humidity.

HSA or HIgG were spiked into the following matrices: (1) 10 mM PB (pH 7.4); (2) artificial urine matrix (adjusted to pH 7.4); (3) artificial saliva matrix to make a gradient of concentrations from 0.15 pM to 15 μM for both analytes; (4) human serum (H4522, Sigma Aldrich) diluted with PB; and (5) whole human blood (10762WB-EK3-MI, BioChemed Services, Inc.) diluted with PB.

All measurements were conducted at room temperature and full humidity (25 ℃, 100% relative humidity). Multiple aliquots of the priming buffer (20 μL 10 mM PB buffer, pH 7.4) were pipetted in the central inlet to fully moisturize the sensor, followed by injections of 20 μL sample solutions and 30 μL of 10 mM PB washes (pH 7.4) if needed. With the source-drain voltage of 0.1 V (e.g., no gate voltage), the electrical resistance changes of the chemiresistor array were monitored continuously with respect to time using a Keithley source meter (Model 2636) while full humidity at room temperature was maintained.

4.4 Results and Discussions

4.4.1 Design of Paper-Based Microfluidics with Paper Bridges

First, we designed the 5-petal shaped hydrophilic channels on paper to equally split one sample into five aliquots for individual sensing channels. As shown in **Figure 4.3a**, one sample injected at the central inlet would split into five. By the capillary force, each aliquot would have traveled along the hydrophilic channel, encountered the CR, and finally reached the waste reservoir at the pattern perimeter. In this design, the CRs can be inkjet-printed in the middle of each channel, followed by incubations with different bioreceptors for 2 h. However, here came the paradox that, while the capillary force transported the aliquots dispensed at the center to the destination spontaneously, it also allowed unwanted diffusion of various bioreceptors throughout the pattern during the incubations—a critical step to achieving multiplexed sensing functions. **Figure 4.3a** illustrates this unwanted diffusion using dyed solution. To mimic the 2-hour incubation, the dye was added in one

channel and was observed to travel into the other four channels and contaminated them with the non-desired molecules. Similarly, the CRs would have been contaminated with the undesired bioreceptors during bioreceptor incubations, which would have resulted in loss of selectivity for all sensing channels. Therefore, it was necessary to keep local functionalizations free of cross-contaminations and maintain the high specificity for each CR biosensor, while taking advantage of the self-wicking capability of paper to transport the sample and wash fluids from the central inlet to sensing channels.

Next, to address this predicament, we employed five pairs of extra wax barriers before, and a structure named ‘paper bridges’ after the bioreceptor incubations. Firstly, to confine the various incubation solutions for the duration (2 hours) of biofunctionalization, extra wax barriers that were perpendicular to the direction of the microfluidic channels were printed simultaneously with the 5-petal pattern (**Figure 4.3a**). The 5- petal channel with extra wax barriers were melted through the thickness of the paper and formed unyielding hydrophobic barriers, thus the sensing channels were partitioned by the extra wax barriers into separated regions where no diffusion was observed, as indicated by the non- interacting dye and clear water regions in **Figure 4.3a**. For the 2-h span of the incubation, extra wax barriers successfully prevented the cross- contaminations of different bioreceptors and preserved the high specificity of each sensing channel, as discussed in the crosstalk control. Secondly, after the functionalizations, the CR arrays were ready to receive the sample transport. However, the radial hydrophilic channels were now blocked by the extra wax barriers, which prevented the transport of liquid samples. Therefore, we employed the paper bridges to overcome this issue, as shown in **Figure 4.3b** (see **Figure**

4.4 for the paper bridge fabrication). The paper bridges acted as hydrophilic bridges for the liquid samples to flow over the extra wax barriers. The full-complement of the paper bridges, which had two concentric rings with melted discontinuous magenta wax, were accomplished by assembling them on top of the extra wax barriers to provide the hydrophilic openings and reconnect the microfluidic channels (see **Figure 4.5** for microfluidic dimensions). The middle image in **Figure 4.3b** shows the dyed equal flows of dye solution in the reconnected channels.

Figure 4.3c shows the mass fabrication process of the sensing platforms. On a 20cm-by-20cm Whatman Grade 1 paper, silver ink was inkjet-printed, and heat annealed to develop conductive silver leads. Paper is known to be sensitive to heat, but the optimized annealing temperature (200 ˚C) had a negligible impact on the capillary flow in the paper (**Section 4.3.1**). Next, the 5-petal pattern with extra wax barriers was printed and melted to form the hydrophobic barriers, followed by bovine serum albumin (BSA) blocking for all channels to prevent non-specific adsorption (**Figure 4.2**). After that, a formulated ink of water-based PCA/SWCNTs[11] was inkjet printed in the middle of each channel with an optimized inkjet condition to maintain the printing consistency (see **Section 4.3.2** for ink formulation and inkjet printing condition) After the PCA/SWCNTs were printed and the formulation solvent evaporated at room temperature, conjugation of the bioreceptors on the SWCNTs was performed. To demonstrate the capability of multi-analyte detections of the microfluidic sensing platform, we used two different antibodies: anti-HSA and anti-HIgG. They were individually incubated to produce two sets of CR immunosensors, whereas the fifth CR transducer served as a control (i.e., no antibody conjugated). Thus,

the sensing platform was equipped with two sensing replicas for two targets (HSA and HIgG) and one control channel used as a reference for evaluating the background noise. After biofunctionalizations, the absorption pad, sensing layer and paper bridges were assembled and held in place by tape. Note that the top tape layer tightly sealed any gaps between the sensor array layer and the paper bridges to ensure the connections of hydrophilic paper sections. The adsorbing pad was used as a waste reservoir and provided adequate capillary pumping. As a result, the sensing platform could handle up to ~ 250 μL of liquid. These changes allowed individual functionalizations of the sensor in each channel and retained the utility of the microfluidic channels to transport fluid toward the sensor and subsequently to the waste pad. Meanwhile, the resistances were recorded for individual CRs by connecting the platform to a source meter at the electrical vias.

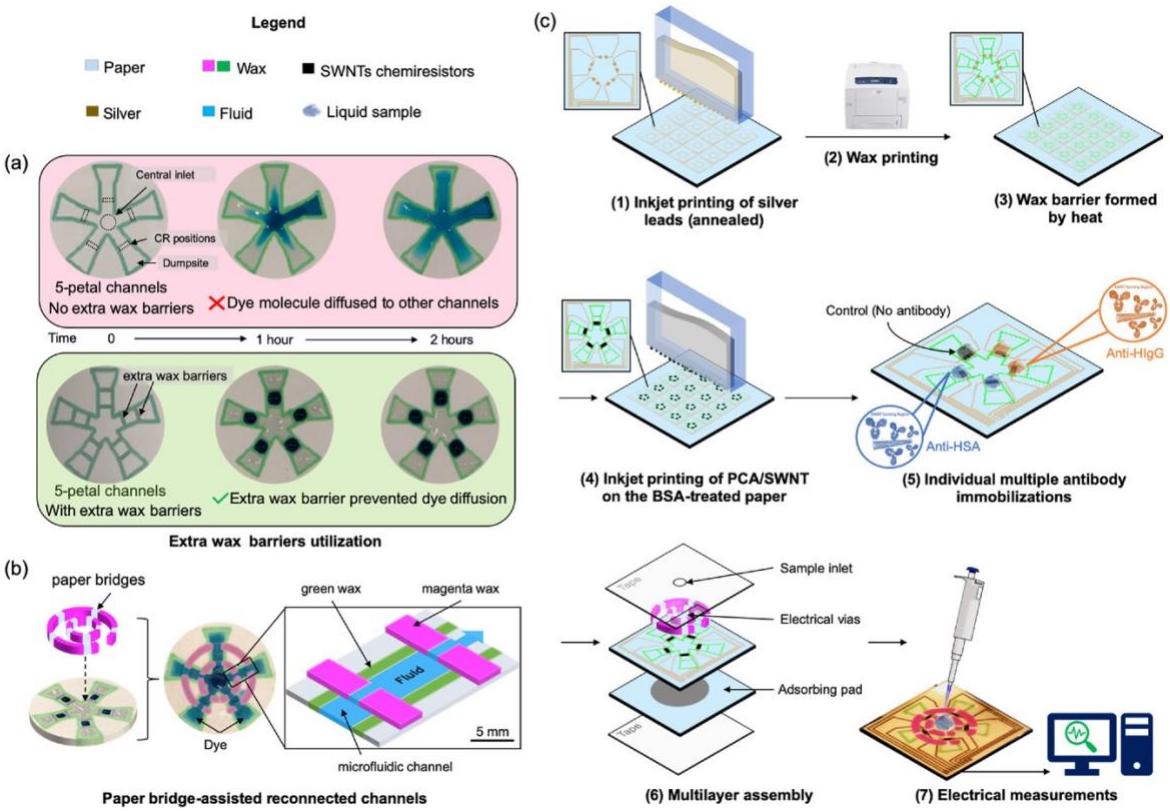

Figure 4.3 Design of the 5-petal microfluidic channels using extra wax barriers and paper bridges and an overall process flow of the sensor fabrication and testing. (a) Top: Pictures showing the dye spreading to other channels over 2 h without extra wax barriers. Bottom: Pictures showing the individual incubations of dyes in each sensing channel with the extra wax barriers. (b) The assembly of the paper bridges and the sensor layers. Paper bridges had two concentric rings with melted discontinuous magenta wax to provide hydrophilic bridges for channel reconnections. Two goals were achieved as 1) individual liquid confinement and 2) paper- based microfluidics reconnection. (c) An overview of the fabrication process: 1) inkjet printing of silver leads, followed by annealing at 200 ◦ C for 2 h; 2) wax printing of the hydrophobic patterns on the paper; 3) 5 min heating at 170 ◦C to melt the wax into paper substrate; 4) inkjet printing of PCA/SWCNTs ink and drying; 5) functionalization of multiple antibodies individually; 6) layer-by-layer assembly of the sensing platform; and 7) measurements of sensor signals.

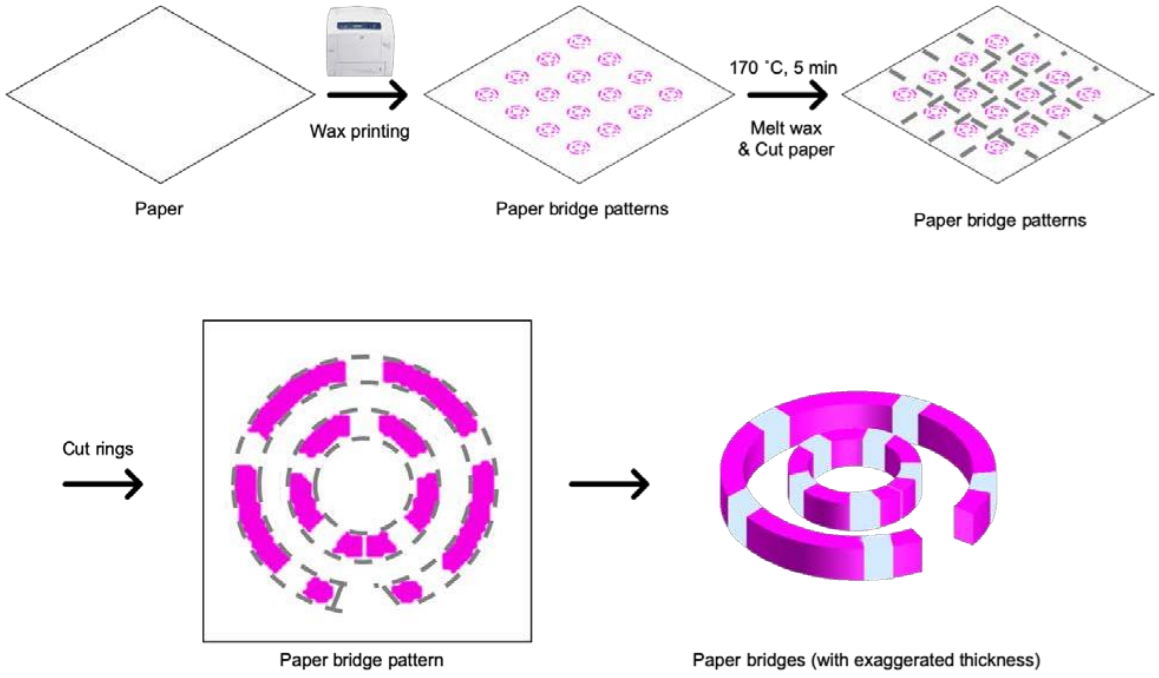

Figure 4.4 Fabrication process of paper bridges.

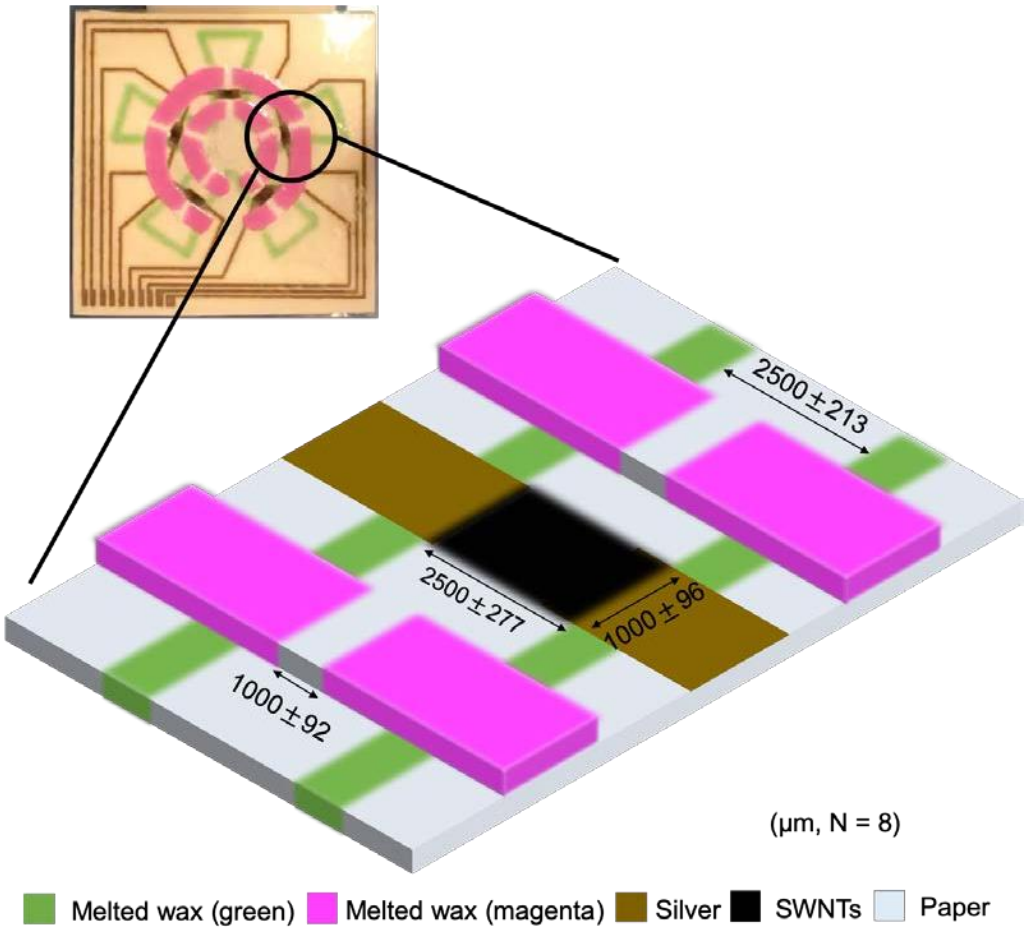

Figure 4.5 The dimensions of the hydrophilic channels, silver leads, and SWCNTs chemiresistors. With optimized geometries of the magenta wax, the paper bridges were made slightly longer to 'touch the ground' for the longitudinal sample delivery paths, and slightly narrower to prevent lateral leakages.

4.4.2 Optimization of SWCNTs Network Density

Since SWCNTs are rod-shaped nanomaterials and percolate into the paper during the deposition to form a 3-dimensional network[27], we varied the SWCNTs network density by inkjet-printing different number of layers of the PCA/SWCNTs ink. The electron microscopy images of SWCNTs network on paper are shown in **Figure 4.6**. The network density increased with printing more layers and resulted in a percolation profile in **Figure 7a**. As illustrated in **Figure 4.6a**, paper substrate itself was made of cellulose fibers and

was porous. After SWCNTs were deposited on the paper substrate, they formed a network (**Figure 4.6b**, and **Figure 4.6c**). The SWCNTs network with moderate density (**Figure 4.6b**, **Figure 4.6e**, and **Figure 4.6i**) was formed by the SWCNTs adherence to the paper fibers, as well as the inter-percolations among SWCNTs. When the SWCNTs formed a dense network, as shown in **Figure 4.6c**, **Figure 4.6f**, and **Figure 4.6j**, the paper fibers were densely deposited with SWCNTs network. In this stage, the resistance was low in the complete percolation region. Sheet resistance (R square) was defined as $R\square = R\ W/L$, where R is the initial resistance of the SWCNTs after inkjet printing with a source-drain voltage at 0.1 V, W is width (1000 ± 96 μm) and L is length (2500 ± 277 μm) of the SWCNTs chemiresistor. The percolation profile was plotted with the logarithm of the inverse of the sheet resistance R□ versus the number of printing layers, and can be divided into three regions: (1) non-percolated, (2) linear percolation, and (3) complete percolation. 1/R□ increased significantly with increasing printing layers in the non-percolated region, linearly in the linear percolation region, and slowly in the complete percolation region. In the non-percolated region, there could be scant SWCNTs to form the electron paths from source to drain electrodes as well as the inadequate affinity binding sites for the sensing activity. On the contrary, in the complete percolation region, there could be too many metallic SWCNTs short-circuiting the semiconducting SWCNTs, which might conceal the responses due to antigen-antibody affinity binding events near the semi-conducting SWCNTs. Therefore, we hypothesized that a network composed of neither too little nor too much semiconducting and metallic SWCNTs would be desirable for building a highly

sensitive CR and anticipated that the most sensitive density of SWCNTs network would be in the linear percolation region with initial resistance from 9.6 ± 0.14 kΩ to 80.5 ± 1.8 kΩ (**Figure 4.7a**). To test our hypothesis, we evaluated the PCA/SWCNTs CR arrays with various initial resistances (R_i) for a gas sensing with NO_2 in N_2 (**Figure 4.1**). All subsequent electrical responses in this work, for both gas and liquid phase sensing, are defined by **Equation 1**, where R_0 is the resistance of the SWCNTs CR after priming with N_2 or liquid buffer, and R is the stable resistance after each exposure to the samples. For the NO_2 gas sensing, the Fermi level shifted towards the valence band with NO2 adsorbed on the p-typed SWCNTs and resulted in an increase of conductance[28]. As shown in **Figure 4.7b**, the ideal initial resistance range of 25 kΩ – 35 kΩ at 25 ˚C and relative humidity (RH) ~ 30% gave the highest sensitivity, which was also confirmed by additional liquid phase biosensing. **Figure 4.8** shows that only the SWCNTs with appropriate initial resistance within the ideal range between 25 to 35 kΩ (i.e., appropriate printing layers and SWCNTs network density) exhibited the maximum sensitivity to the antigen-antibody binding events. Therefore, all subsequent sensors were prepared to have a similar initial resistance value.

$$Response = \frac{R-R_0}{R_0} = \frac{\Delta R}{R_0} \qquad \textbf{Equation 1}$$

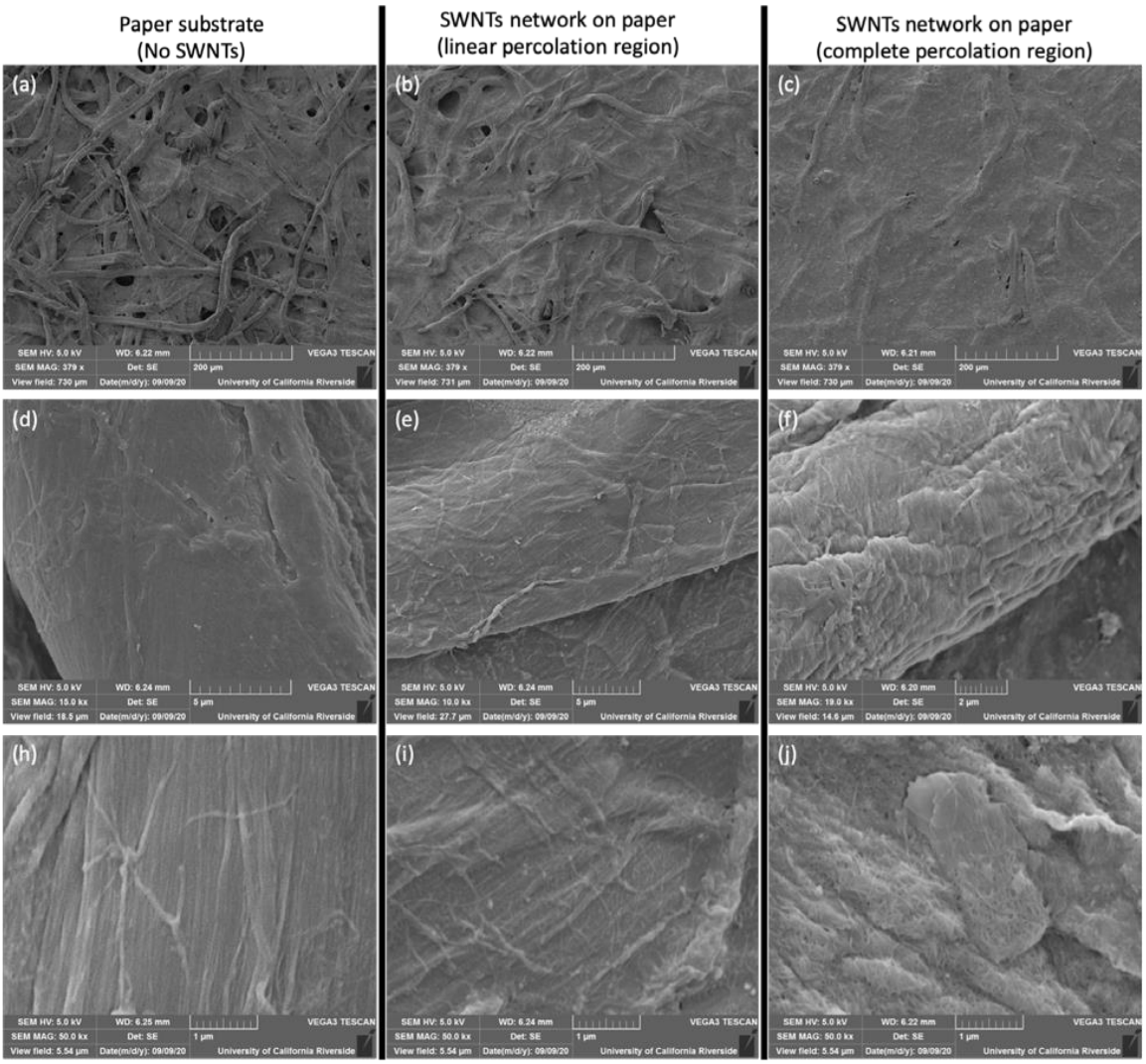

Figure 4.6 Scanning electron microscope images of paper substrate, moderate SWCNTs network on paper, and dense SWCNTs network on paper. (a) An overview of paper substrate. (b) An overview of paper substrate with a moderate SWCNTs network that gave a resistance in the linear percolation region. (c) An overview of paper substrate with a dense SWCNTs network that gave a resistance in the complete percolation region. (d) and (h), (e) and (i), (f) and (j) are the zoomed-in images for paper substrate, moderate SWCNTs network, and dense SWCNTs network, respectively.

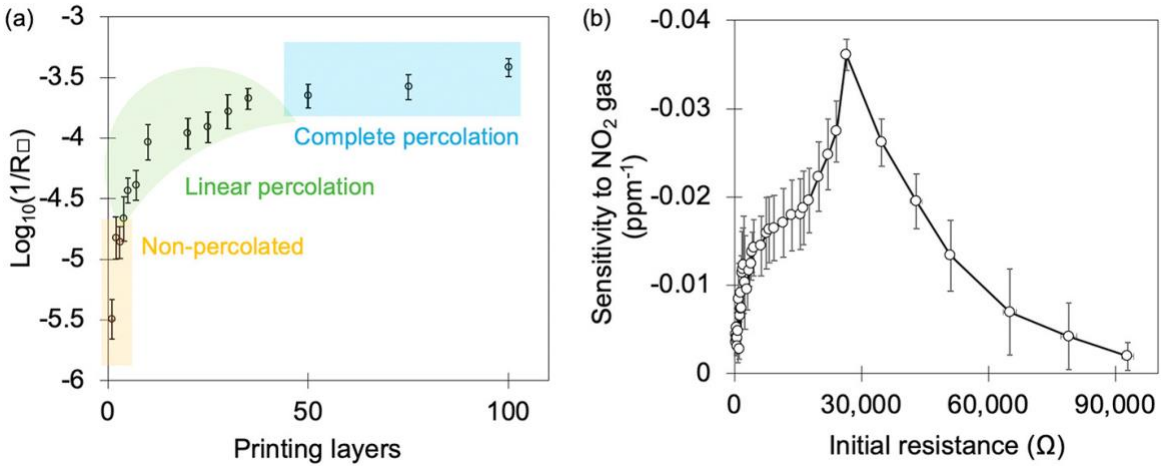

Figure 4.7 Percolation profile of the inkjet-printed PCA/SWCNTs network on the paper substrate and the optimization of the CR initial resistances. (a) The percolation profile of inkjet-printed PCA/SWCNTs network on paper substrate. (b) Sensitivities of PCA/SWCNTs networks with various initial resistances. Each data point is average of 5 sensors. Error bars represent ±1 standard deviation.

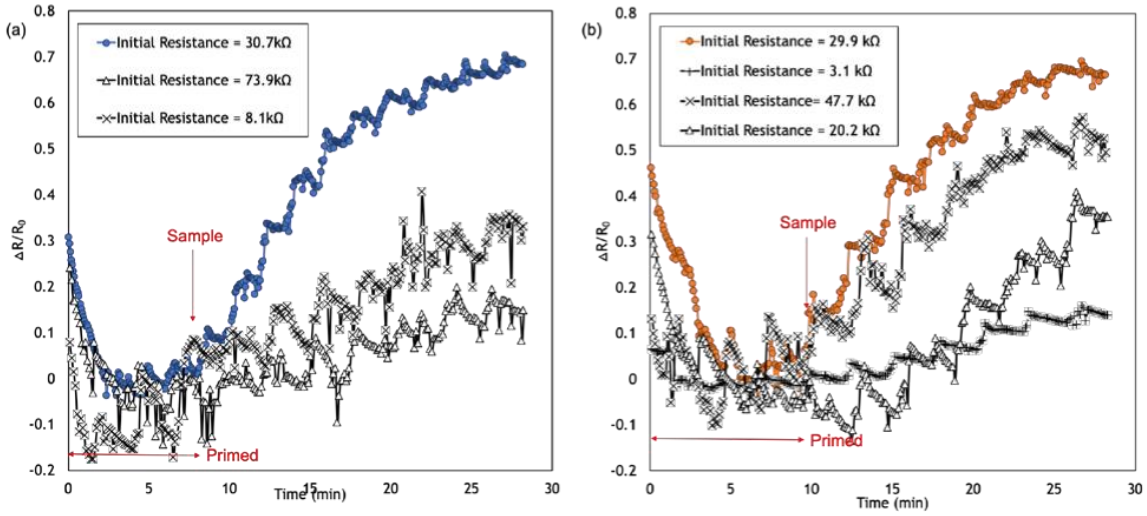

Figure 4.8 Real-time monitoring of the increasing resistance during the sensing process. Both (a) anti-HSA and (b) anti-HIgG chemiresistive sensors were prepared with various SWCNTs network densities and consequently various initial resistances. Initial resistance referred to Ri after PCA/SWCNTs were inkjet-printed and dried at 25 ˚C and relative humidity of ~ 30%.

4.4.3 Optimization of Sensing Environment and Controls

Results in **Figure 4.9** exemplify that the ambient humidity was unable to stabilize the responses. At first, adsorption of water in 10 mM PB to the dry CR led to a considerable increase in the resistance since the water molecules were electron- donating and thus n-doped the p-typed SWCNTs[29]. Upon adding a sample of HSA/PB, the resistance increased further, but followed by a steep decrease to near the starting resistance instead of a plateau (**Figure 4.9**). We attributed this phenomenon to the dynamic equilibrium of water adsorption due to sample additions and desorption due to water evaporation, which was vital to the steady readings of the electrical responses. Thus, to eliminate the impact of evaporation, we implemented a PB priming step to create a locally saturated liquid environment before analyte additions and maintained a full RH during the whole sensing process. With full humidity maintained during storage, SWCNTs were eventually counter-doped by n-doping water molecules to be n-typed semiconductors[29]. As a consequence, we observed an additional decrease in resistance in the first 4 min, as shown in **Figure 4.10a** and **Figure 4.10c**. In this sensing platform, two additions of 20 μL PB made the sensor baseline readings stable and any subsequent changes in resistance were results of affinity binding events instead of the variation of moisture level during the sensing process. Another benefit of priming was to reduce sudden sensor distortion due to paper fiber swelling from the absorption of a water-based liquid sample[30]. The target proteins, however, at the sensing pH, were possibly behaving as an electron acceptor and repelled the electron carriers in the semiconducting SWCNTs[31–33]. Thus, upon the exposure to the negatively charged analyte, the n-type SWCNTs CR were exhibiting increases in the resistance.

Positive and negative controls demonstrated the selectivity of the biosensors. The positive control experiments with SWCNTs blocked with tween-20 (without antibodies) that were exposed to PB (blank), 15 μM HSA, and 15 μM HIgG produced low responses of 2.17%, 3.28%, and 3.64%, respectively (**Figure 4.11**). This established the effectiveness of tween-20 blocking process in preventing non-specific adsorption of analytes to SWCNTs. Similarly, negative control experiments in which biosensors functionalized with anti-HSA and anti-HIgG were exposed to 20 μL of PB (blank) showed significantly smaller responses (< 5%) compared to their targeted analytes (**Figure 4.12**). This corroborated that the high responses were indeed from the antigen-antibody binding.

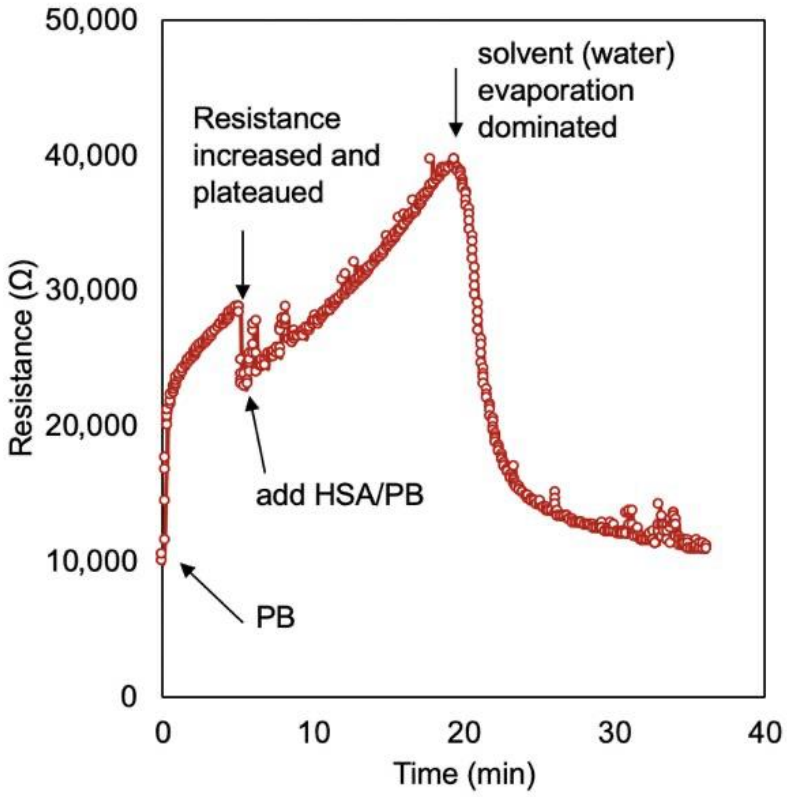

Figure 4.9 An example of how the ambient environment affect the response reading of the chemiresistive biosensor.

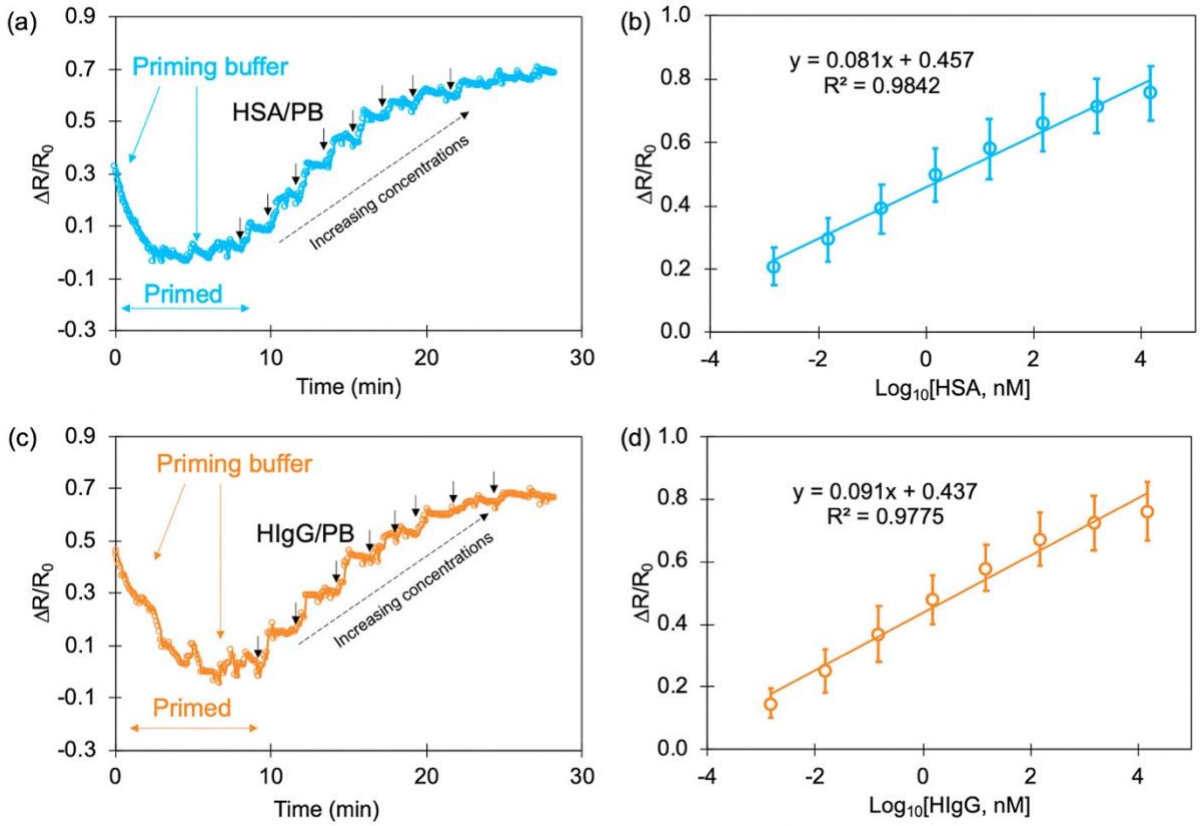

Figure 4.10 Real-time monitoring of the changes in resistance during the priming process and sensing process for additions of 20 µL samples prepared in PB and their corresponding calibration curves. (a) Real- time monitoring of the sensing process for the detections of HSA/PB (pH 7.4). (b) Calibration curve for the detection of HSA/PB with a linear regression $y = 0.081\text{Log}_{10}[\text{HSA}] + 0.457$ with $R^2 = 0.9842$. (c) Real-time monitoring of the sensing process for the detections of HIgG/PB (pH 7.4) (d) Calibration curve for the detection of HIgG/PB with a linear regression $y = 0.091\text{Log}_{10}[\text{HIgG}] + 0.437$ with $R^2 = 0.9775$. Each data point is average of 6 sensors. Error bars represent ±1 standard deviation.

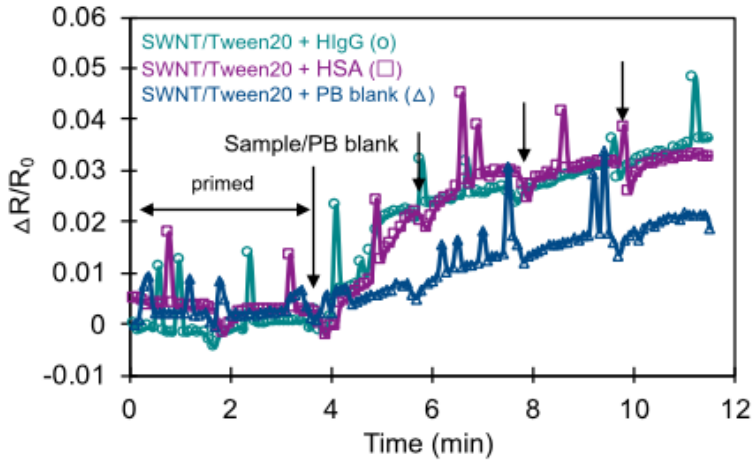

Figure 4.11 Positive control experiments of comparison between the responses from non-functionalized SWCNTs chemiresistors with protein and PB blank samples.

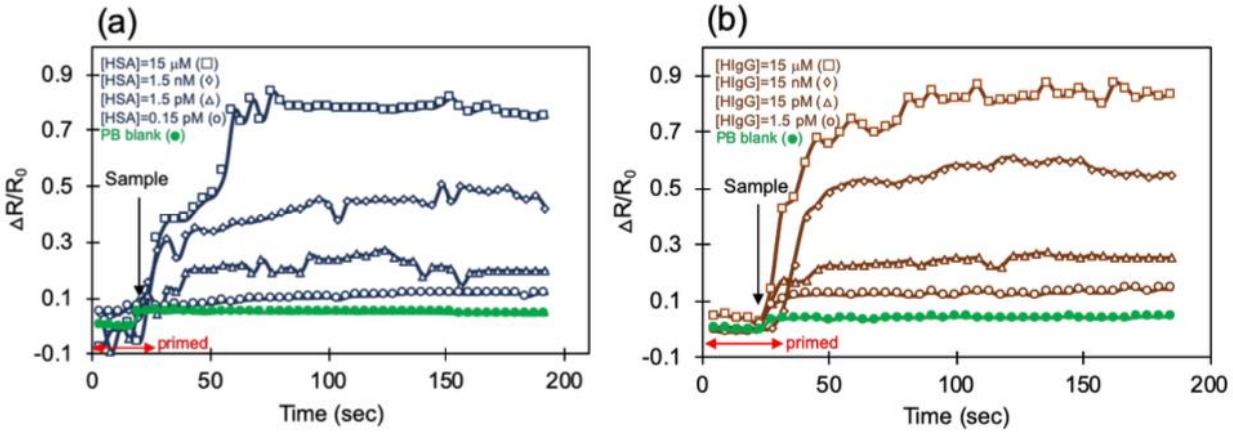

Figure 4.12 Negative control experiments. Individual biosensors functionalized with anti-HSA and anti-HIgG were exposed to 20 μL of PB (blank) showed significantly smaller responses (< 5%) compared to their targeted analytes (20 μL samples). (a) Comparison between the responses from HSA sensing and blank control (negative control). (b) Comparison between the responses from HIgG sensing and blank control (negative control).

4.4.4 Sensitivity and Limit of Detection

Figure 4.10a and **Figure 4.10c** show dynamic responses of the sensor arrays to each target protein from 0.15 pM to 15 μM in PB. After priming, as new samples (20 μL) of higher concentrations of the target proteins were added (4 μL per channel), the CR

resistances increased and reached higher plateaus quickly for higher concentrations. **Figure 4.10b** and **Figure 4.10d** show the calibration plots of plateau responses as a function of antigen concentrations in PB. The sensors responded linearly to both analytes be- tween 1.5 pM and 15 μM, which included the biologically meaningful range for potential urine analysis[34,35]. The sensitivities (slope of the calibrations) were 0.081 per Log_{10}[nM of HSA] and 0.091 per Log_{10}[nM of HIgG]. The lowest detectable con- centration for HSA and HIgG in PB estimated by S/N = 3 were 1.5 pM, which was comparable or better than the reported to-date for these proteins in terms of both the linear ranges and detection limits (**Table 4.1**). Furthermore, as evidenced by a low residual standard deviation (RSD) of 11.2% and 12.2% for responses from 6 sensors each of HSA and HIgG at 15 μM, respectively, the sensors had excellent precision. The high sensitivity of SWCNTs network FET/CR based biosensors fabricated on non-porous substrates have been well documented, and the physics behind it explained in detail[22]. However, the sensitivities observed in this work for the SWCNTs network CR on paper substrate are markedly superior. We ascribed the ultrahigh sensitivity of the present paper-based CR arrays to the porous paper substrate that promotes 1) improved connectivity of SWCNTs due to firm adhesion of individual SWCNTs in porous and rough paper surface compared to uniform surface of Si/SiO_2 or glass solid substrate[29]; and 2) weaker counter-ion screening, consequently higher sensor response, from concave corners that are preferably formed/promoted when SWCNTs lie on cellulose fibers compared to flat solid substrate[36]. Also contributing to the high sensitivity can be the high loading of antibodies for effective capture of antigens that was the result of large loading of –COOH groups from the attached PCA on SWCNTs[11].

Method	Analyte	Linear range	Detection limit	Ref.
Optical/Immunochemical	HSA	0.11 μM – 2.25 μM	0.11 μM	[37]
Field effect transistor	HSA	100 pM – 100 nM	0.28 nM	[38]
Colorimetric & fluorometric	HSA	0 – 1 μM	2.98 pM	[39]
Fluorescence	HSA	0 – 1.5 μM	92 nM	[40]
Chemiresistor	HSA	1.5 pM – 15 μM	1.5 pM	*This work*
Field-effect transistor	HIgG	8 nM – 56 nM	3.2 nM	[41]
Field-effect transistor	HIgG	7 fM – 0.7 pM	7 fM	[42]
Electro-chemiluminescence	HIgG	67 pM – 6.7 μM	14 pM	[43]
Amperometry	HIgG	13.3 pM – 0.67 nM	11.3 pM	[44]
Luminescence	HIgG	52 fM – 1.67 pM	4.3 fM	[45]
Chemiresistor	HIgG	1.5 pM – 15 μM	1.5 pM	*This work*

Table 4.1 Comparisons of detection limit and linear range between this work and those recently reported relevant biosensors for the detections of HSA and HIgG.

4.4.5 Specificity and Stability

To test the specificity of the sensing channels, crosstalk controls were examined by checking the electrical responses when the sensor encounters the wrong analyte (i.e., anti-HSA/SWCNTs with HIgG/PB and anti-HIgG/SWCNTs with HSA/PB). As shown in **Figure 4.13a**, the sensors with the wrong target only resulted in 13.4% and 11.1% increase in the electrical responses, respectively, for anti-HSA/SWCNTs sensor with 15 μM HIgG and anti-HIgG/SWCNTs with 15 μM HSA, which were minimal compared to the positive sensing responses of 86.2% and 88.8%, respectively, for 15 μM of HIgG/PB and HSA/PB. Therefore, the extra wax barriers successfully prevented cross-contamination of the two antibodies during the functionalization and lead to the high specificities between different sensing channels. However, the crosstalk did give rise to 2- to 3-fold larger responses (10

– 15%) than the other controls (< 5%). We attributed this to the drift of the SWCNTs CRs over the ~ 40 min sensing period, and the quality of the commercial antibodies that were potentially not perfectly purified to ensure absolute specificity and thus resulted in higher responses in the crosstalk controls.

Storage stability (i.e., shelf life) is of great significance to maintaining the quality and robustness of the diagnostic devices. Thus, batches of the fully integrated paper-based CR array were prepared and stored for varying durations under full humidity at room temperature or 4 ˚C. Sensors were tested on day 7, 14, and 21. The sensitivities were calculated in the same manner as previously described and were normalized against the sensitivities at day 0. As shown in **Figure 4.13b**, at 4 ˚C the sensors retained nearly 100% sensitivity for three weeks. On the other hand, when stored at room temperature, there was a 11.2% and 22.0% drop in sensitivity after 3-weeks for anti-HSA/SWCNTs sensors and anti-HIgG/SWCNTs sensors, respectively. These results demonstrated good overall stability of antibodies conjugation and SWCNTs transducers.

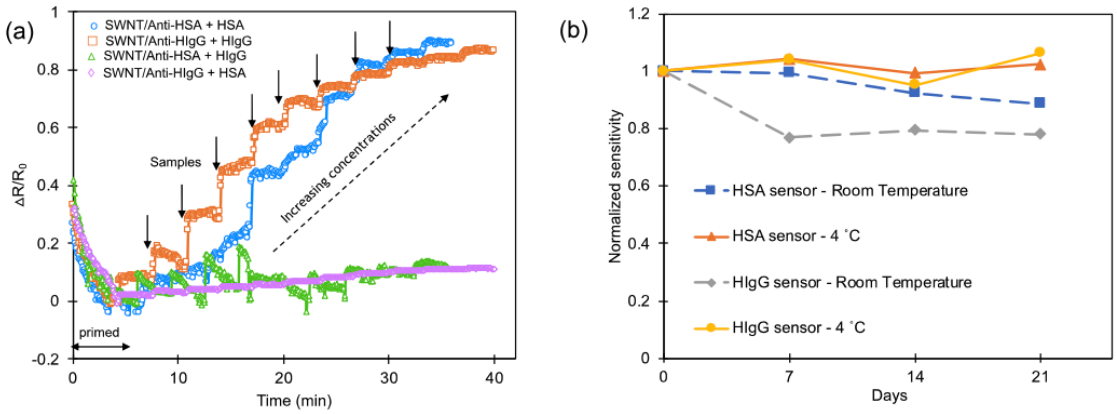

Figure 4.13 Real-time monitoring of the changes in resistance for sample sensing and controls. (a) Comparison between the responses from HSA and HIgG sensing and the crosstalk controls. (b) Normalized sensitivity of the sensor array stored at room temperature or 4 ˚C.

4.4.6 Application of Sensors to Samples in Biological Matrices

Detection of proteins as disease biomarkers in body fluids is routinely performed in healthcare. To demonstrate the potential of the described paper-based CR biosensor arrays, we applied the sensors to detect HSA and HIgG in human body fluids such as urine, saliva, serum, and whole blood. We used an artificial urine (AU) matrix to simulate the real-life sensing environment[46]. Since the AU contained a lot of salts and had high ionic strength, which minimized the Debye length, PB washes were necessary to recover the responses of the responses of SWCNTs CR from the affinity binding of antigen-antibody interaction. After PB priming, 20 μL AU spiked with the target proteins were added to individual sensors. As shown in **Figure 4.14a** and **Figure 4.14b**, the responses for both targets were reduced compared to the PB samples due to the high ionic strength of the AU matrix at about 1.18 M, resulting in small Debye length[36,47,48]. After the first wash passing through the CRs, some responses were recovered, and the second and third wash recovered the responses further, reaching steady levels comparable to those in PB samples. The possible mechanism was that the washes diluted the local AU matrix and removed the salts to the absorbing pad, making a local environment with low ionic strength close to 24 mM (the ionic strength of PB), and a larger Debye length to overturn the charge screening and recover the responses[48]. The insets in **Figure 4.14a** and **Figure 4.14b** show that detection of HSA and HIgG in AU after implementing three washings of 30 μL each were in excellent agreement with the responses in PB, indicating the minimal matrix effects left after the washing with PB.

Saliva is a non-invasively collected body fluid sample and contains many important biomarkers[49,50]. To administer a test of biomarkers in a salivary matrix, we spiked HSA and HIgG into the artificial saliva (AS) to simulate the salivary matrix[51]. A similar sensing protocol with PB washes for the AU sample was employed. Although the mucin in AS matrix increased fluid viscosity, there was no obvious discrepancy of the flow rate and fluid delivery time to those of PB and AU samples. As shown in **Figure 4.14c** and **Figure 4.14d**, controls exhibited minimal responses compared to the detection of salivary HSA and HIgG, which gave linear regression of $y = 0.084\text{Log}_{10}[\text{HSA, nM}] + 0.291$ with $R^2 = 0.9833$, and $y = 0.081\text{Log}_{10}[\text{HIgG, nM}] + 0.283$ with $R^2 = 0.9938$, respectively. With the washing steps, the sensitivities (slopes) to salivary HSA and HIgG were 100.12% and 88.67% to those in PB, respectively.

Furthermore, we tested the sensors with human serum and whole human blood from commercial sources (collected from healthy donors). As the concentrations of the target proteins in serum and blood largely exceeded the dynamic range of the sensor array, serum and blood were analyzed after diluting 10^7 times with PB. Column 3 in **Table 4.2** reports the concentrations of HSA and HIgG found in these diluted samples using the calibration plots in **Figure 4.10b** and **Figure 4.10d**. The detailed calculations were shown in **Table 4.3** and as below: As listed in the **Table 4.2**, human serum and blood were diluted 10^7 times with 10 mM PB (pH 7.4), and sensors were exposed to two rounds of samples. Firstly, the buffer primed sensor array was exposed to the serum or blood that were diluted 10^7 times, and we recorded the first-round responses as $[R_1\text{-}R_0]/R_0$, where R_0 was the PB primed resistance and R_1 was the stable resistance after the first-round sample addition. Then a

concentration of HSA or HIgG was back-calculated based on the calibration curve in **Figures 4.10b** and **Figure 4.10d** and was denoted as C_1. Based on C_1, HSA and HIgG were spiked to the 10^7-diluted serum or blood to a new concentration of HSA or HIgG that was denoted as C_2. C_2 was particularly chosen to be five times higher than C_1 (i.e., $C_2 = 5 \times C_1$) in order to see a relatively large gain in the responses due to the second-round samples. Secondly, the second-round samples with spiked concentrations of HSA and HIgG at C_2 were added to the same batch of sensor array, and the second-round responses were recorded as $[R_2-R_0]/R_0$, where R_0 was still the PB primed resistance and R_2 was the stable resistance after the second-round sample addition. As seen in **Table 4.3**, the anti-HSA/SWCNTs sensor and anti-HIgG/SWCNTs sensors gained 16 - 17% and 24 - 25% more increase than the first-round average responses in the resistance when exposed to the second round of samples, respectively. Next, based on the average responses to the second-round samples, another concentration of HSA or HIgG was back-calculated by the calibration curves in **Figure 4.10b** and **Figure 4.10d** and was denoted as C_3 and listed in **Table 4.3**. Assuming the concentrations of the targets in the two rounds of samples (C_1 and C_2) were within the dynamic range of the sensor array, the back-calculated concentrations (C_1 and C_3) should ideally be 5 times different. Thus, the concentration ratios (percent recovery) of C_3 and C_1 were determined as the value of $100\% \times [C_3/(5 \times C_1)]$, where 5 is the multiplier for the spiking. As listed in the last column in **Table 4.3**. We achieved 90 ± 10% of all concentration spiking, which indicated the sensor reliability to the diluted real human serum and blood samples. The concentrations of HSA in the two rounds of samples (diluted and spiked samples) calculated by the calibration equation with dilution factor considered

were 33.6 mg/mL and 30.4 mg/mL in human serum, and 44.7 mg/mL and 48.2 mg/mL in human blood, respectively. The concentrations of HIgG in the two rounds of samples (diluted and spiked samples) calculated by the calibration equation with dilution factor considered were 13.6 mg/mL and 12.9 mg/mL in human serum, and 16.2 mg/mL and 15.2 mg/mL in human blood, respectively. These values fell within the typical normal ranges of HSA and HIgG in human serum or blood of 36 - 51 mg/mL and 7.7 - 15.9 mg/mL, respectively[52–54]. These were justifiable results since the serum and blood used in this research were from healthy donors with normal health conditions.

Subsequently, we spiked the diluted samples with known concentrations of HSA and HIgG (**Table 4.2**, column 4), analyzed with the same sensor arrays and determined the percent recovery (**Table 4.2**, last column). As shown in the table, the recoveries (i.e., agreement) ranged from 90% to 108% (average of 96.75 ± 7.8%). These high recoveries, i.e., accuracy of the sensors, were achieved without buffer washes since the serum and blood were diluted 10 million-fold in PB thus diluting the concentration of salts and minimizing the non-specific adsorption from blood cells and other proteins. These results showed the wide applicability of the integration of the SWCNTs-based chemiresistive biosensors with the paper-based microfluidics to both simple PB and complex matrices of artificial urine, saliva, human serum, and human blood.

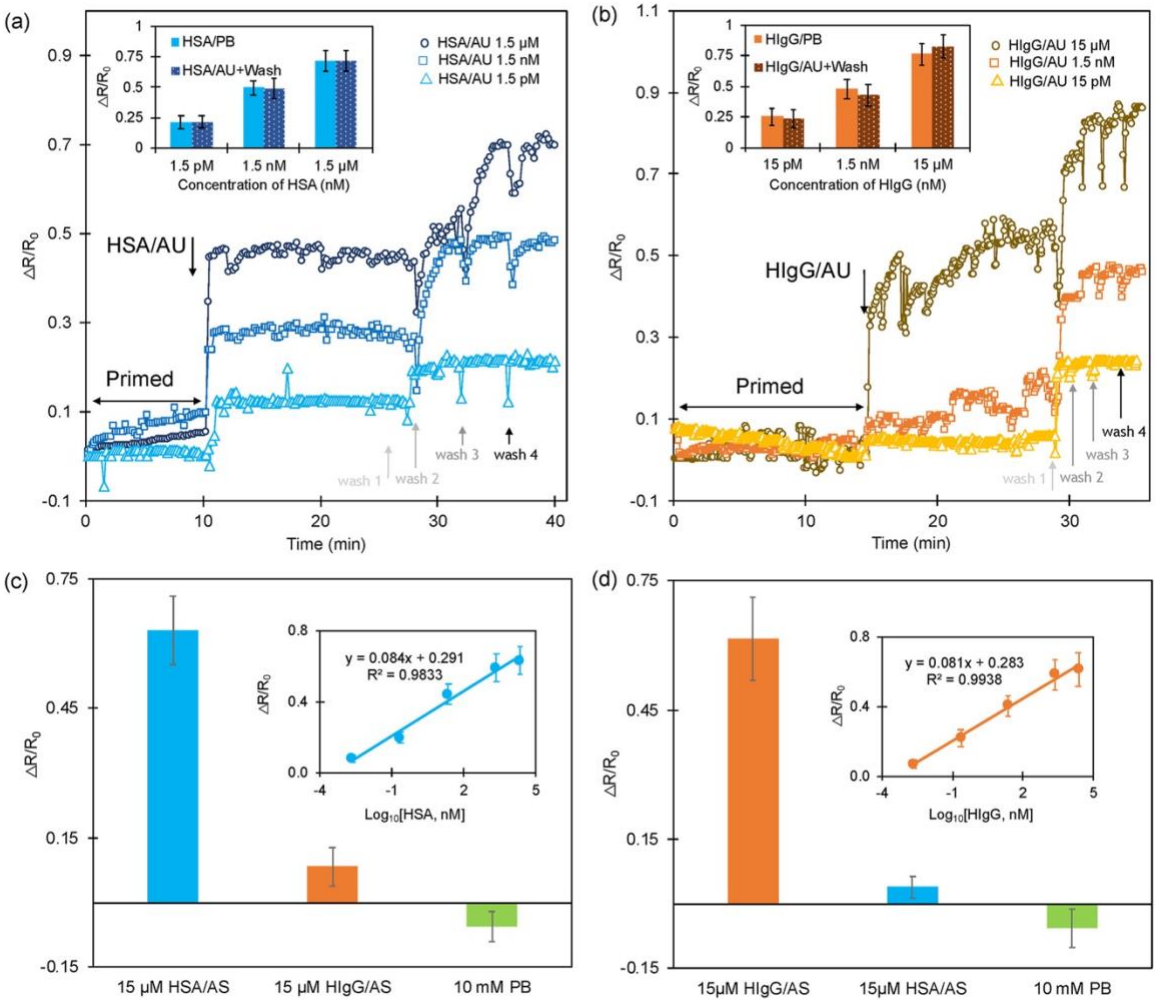

Figure 4.14 Sensing responses from samples (20 µL) in complex matrices. Real-time monitoring of the detection of (a) HSA and (b) HIgG spiked in an AU matrix (pH 7.4) with full humidity at room temperature. 30 µL of each 10 mM PB wash diluted the local matrix and recovered the electrical responses. Comparison of responses from (c) anti-HSA functionalized sensors and (d) anti-HIgG functionalized sensors to 15 µM HSA and 15 µM HIgG spiked in an AS sample after washing with 10 mM PB and controls. Inset figures show comparison of responses for (a) HSA and (b) HIgG in AU after washing and PB, calibration plots of (c) anti-HSA functionalized sensors for HSA and (d) anti-HIgG functionalized sensors for HIgG detection in AS after washing. Each data point is average of 6 sensors. Error bars represent ±1 standard deviation.

Sensor	Sample [a]	Found (μg/mL)	Added [b] (μg/mL)	Detected after adding (μg/mL)	Recovery (%)
Anti-HSA/SWCNTs	Human serum	3.36	13.44	15.2	90.5
Anti-HSA/SWCNTs	Human blood	4.47	17.88	24.1	107.8
Anti-HIgG/SWCNTs	Human serum	1.35	5.40	6.46	95.7
Anti-HIgG/SWCNTs	Human blood	1.62	6.48	7.58	93.6

Table 4.2 A table summary of the sensor responses to the diluted and spiked samples of human serum and human blood.

Sensor	Sample	Average Sensor response (N=5)	Conc. from calibration (mg/mL)	Average response gain after spiking	Conc. ratio (C_3/C_1)	Conc. recovery ($100\% \times C_3/[5 \times C_1]$)
Anti-HSA/SWCNTs	Human serum[(a)]	$(R_1-R_0)/R_0$ = 0.344±0.0380	C_1 = 3.36×10^{-6}	16 %	4.52	90 %
	Human serum[(b)]	$(R_2-R_0)/R_0$ = 0.399±0.0379	C_3 = 1.52×10^{-5}			
	Human Blood[(a)]	$(R_1-R_0)/R_0$ = 0.355±0.0338	C_1 = 4.47×10^{-6}	17 %	5.39	108 %
	Human Blood[(b)]	$(R_2-R_0)/R_0$ = 0.416±0.0359	C_3 = 2.41×10^{-5}			
Anti-HIgG/SWCNTs	Human serum[(a)]	$(R_1-R_0)/R_0$ = 0.248±0.0284	C_1 = 1.35×10^{-6}	25 %	4.77	95 %
	Human serum[(b)]	$(R_2-R_0)/R_0$ = 0.310±0.0302	C_3 = 6.46×10^{-6}			
	Human Blood[(a)]	$(R_1-R_0)/R_0$ = 0.255±0.0266	C_1 = 1.62×10^{-6}	24 %	4.69	94 %
	Human Blood[(b)]	$(R_2-R_0)/R_0$ = 0.317±0.0311	C_3 = 7.58×10^{-6}			

Table 4.3 A table summary of the sensor responses to the diluted and spiked samples of human serum and human blood. (a) Human serum or human blood diluted 10^7 times with 10 mM PB, pH 7.4. (b) Human serum or blood diluted 10^7 times with 10 mM PB, pH 7.4, and spiked with target analyte protein (HSA and HIgG) to C_2.

4.4.7 Origami Devices with Easy Assembly

Despite the easy assembly required, the critical alignment of the hydrophilic pathways and the secure adhesion between the tapes and layers are vital for the paper-based microfluidic transport. Misalignment between paper-sections and the lack of solid lamination can lead to unequal sample splitting and thereby unreliable electrical signals and inaccurate results. The use of origami techniques to make 3D devices from a single paper sheet as an alternative to stacking multiple layers has been reported[55,56]. Therefore, to further standardize the fabrication and reduce hand assembly errors, we designed a wax-patterned origami device that demonstrated the same idea of employing extra wax barriers and paper bridges (**Figure 4.15a**). The origami was composed of three layers: (1) top layer for sample-splitting and paper-bridging, (2) middle layer with CR biosensor arrays for multiplexed detections and (3) bottom layer with sufficient absorbing capability. Unlike the manually assembled ones, origami devices benefited from the precise trimming by CO_2 laser cutting that helped facile alignment of the three layers thereby reducing the human labor and error (**Figure 4.15b**). **Figure 4.15c** shows that the dynamic responses for PB priming and sensing of the target proteins in the origami device were comparable to the previous layer-by-layer assembled paper-based microfluidic label-free CR biosensing arrays. The primed CRs exhibited large increases in resistance upon addition of target analytes and low responses in the blank control. The origami devices provided a cost-effective and practical method to integrate both the well-controlled paper-based microfluidics and highly sensitive and selective chemiresistive biosensor array into one for label-free multiplexed detection of important biomarkers.

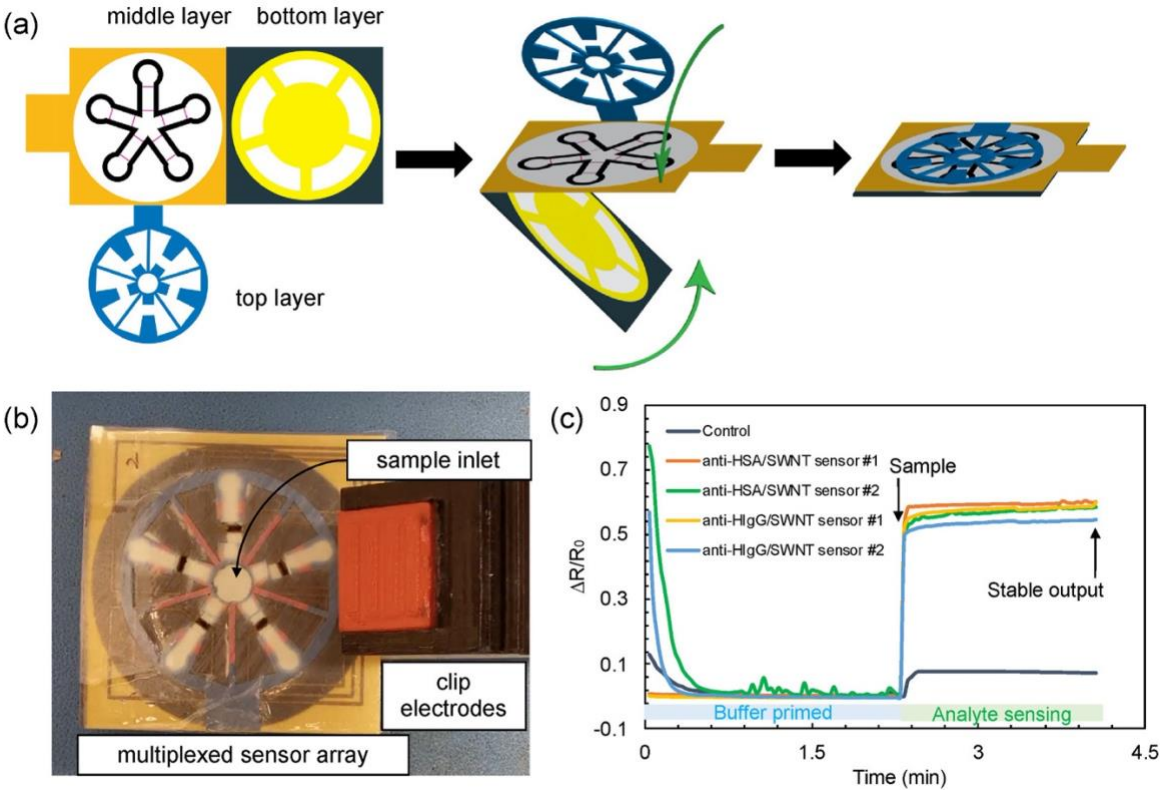

Figure 4.15 Fabrication and sensing protocol of the origami device. (a) Assembly of the three-layered origami device. (b) Image of the origami device with clip electrodes attached. (c) The processed electrical output of the origami device for 15 nM each of HSA and HIgG in PB.

4.5 Conclusions

We developed an affordable and practical paper-based sensing platform for rapid multiplexed label-free detections of relevant bio- markers by employing antibody conjugated SWCNTs CRs with the top- down integration of paper-bridging microfluidics. With the use of extra wax barriers and paper bridges, the fully assembled devices, both manual and origami assembled, successfully split one sample into equal aliquots and transferred into individual sensing channels with negligible crosstalk. With optimal percolation density of the inkjet-printed SWCNTs network, we immobilized anti-HSA and anti-HIgG antibodies on multiple CRs for a demonstration of detections of multiple

biomarkers in a single microliter-size sample. The device showed high sensitivity, specificity, and stability for the detection of the target analytes. In complex sample matrices including artificial urine and saliva, and diluted human serum and blood, efficient buffer washes successfully overcame the reduction in signals due to shortened Debye length in highly ionic or viscous solutions. Furthermore, precise and undemanding origami design was employed to achieve simple fabrications of the biosensor array towards mature and practical assembly of the described diagnostic device. The reported biosensing platform is expected to promote the future development and adoption of FET/CRs on paper substrates in not only the resource-limited diagnostic applications such as ASSURED devices, but also other sensing scenarios, including but not limited to, on-site environmental monitoring, rapid detection of pathogens, and quick examinations of forensic samples.

4.6 References

1. Smith, S., Korvink, J. G., Mager, D. & Land, K. The potential of paper-based diagnostics to meet the ASSURED criteria. *RSC Adv.* **8**, 34012–34034 (2018).

2. Yager, P. *et al.* Microfluidic diagnostic technologies for global public health. *Nature* **442**, 412 (2006).

3. Gao, Y. *et al.* Wearable microfluidic diaphragm pressure sensor for health and tactile touch monitoring. *Adv. Mater.* **29**, 1701985 (2017).

4. Vengasandra, S., Cai, Y., Grewell, D., Shinar, J. & Shinar, R. Polypropylene CD-organic light-emitting diode biosensing platform. *Lab Chip* **10**, 1051–1056 (2010).

5. Wongkaew, N., He, P., Kurth, V., Surareungchai, W. & Baeumner, A. J. Multi-channel PMMA microfluidic biosensor with integrated IDUAs for electrochemical detection. *Anal. Bioanal. Chem.* **405**, 5965–5974 (2013).

6. Li, J., Wu, Q. & Wu, J. Synthesis of nanoparticles via solvothermal and hydrothermal methods. *Handb. Nanoparticles* 1–28 (2015).

7. Wu, J. *et al.* Inkjet-printed microelectrodes on PDMS as biosensors for functionalized microfluidic systems. *Lab Chip* **15**, 690–695 (2015).

8. Choi, J. R. *et al.* An integrated paper-based sample-to-answer biosensor for nucleic acid testing at the point of care. *Lab Chip* **16**, 611–621 (2016).

9. Fava, E. L. *et al.* Electrochemical paper-based microfluidic device for high throughput multiplexed analysis. *Talanta* **203**, 280–286 (2019).

10. Li, B. *et al.* Quantum dot-based molecularly imprinted polymers on three-dimensional origami paper microfluidic chip for fluorescence detection of phycocyanin. *ACS sensors* **2**, 243–250 (2017).

11. Shen, Y., Tran, T.-T., Modha, S., Tsutsui, H. & Mulchandani, A. A paper-based chemiresistive biosensor employing single-walled carbon nanotubes for low-cost, point-of-care detection. *Biosens. Bioelectron.* **130**, 367–373 (2019).

12. Cheng, C. *et al.* Paper-based ELISA. *Angew. Chemie Int. Ed.* **49**, 4771–4774 (2010).

13. Cinti, S., Minotti, C., Moscone, D., Palleschi, G. & Arduini, F. Fully integrated ready-to-use paper-based electrochemical biosensor to detect nerve agents. *Biosens. Bioelectron.* **93**, 46–51 (2017).

14. Lamas-Ardisana, P. J., Martínez-Paredes, G., Añorga, L. & Grande, H. J. Glucose biosensor based on disposable electrochemical paper-based transducers fully fabricated by screen-printing. *Biosens. Bioelectron.* **109**, 8–12 (2018).

15. Martinez, A. W., Phillips, S. T., Butte, M. J. & Whitesides, G. M. Patterned paper as a platform for inexpensive, low-volume, portable bioassays. *Angew. Chemie Int. Ed.* **46**, 1318–1320 (2007).

16. Sun, X. *et al.* Rotational paper-based electrochemiluminescence immunodevices for sensitive and multiplexed detection of cancer biomarkers. *Anal. Chim. Acta* **1007**, 33–39 (2018).

17. Wang, Y. *et al.* Electrochemical integrated paper-based immunosensor modified with multi-walled carbon nanotubes nanocomposites for point-of-care testing of 17β-estradiol. *Biosens. Bioelectron.* **107**, 47–53 (2018).

18. Ge, L., Wang, S., Song, X., Ge, S. & Yu, J. 3D origami-based multifunction-integrated immunodevice: Low-cost and multiplexed sandwich chemiluminescence immunoassay on microfluidic paper-based analytical device. *Lab Chip* **12**, 3150–3158 (2012).

19. Hu, J. *et al.* Advances in paper-based point-of-care diagnostics. *Biosens. Bioelectron.* **54**, 585–597 (2014).

20. Mettakoonpitak, J. *et al.* Electrochemistry on paper-based analytical devices: a review. *Electroanalysis* **28**, 1420–1436 (2016).

21. Mulchandani, A. & Myung, N. V. Conducting polymer nanowires-based label-free biosensors. *Curr. Opin. Biotechnol.* **22**, 502–508 (2011).

22. Tran, T.-T. & Mulchandani, A. Carbon nanotubes and graphene nano field-effect transistor-based biosensors. *TrAC Trends Anal. Chem.* **79**, 222–232 (2016).

23. Syedmoradi, L. *et al.* Point of care testing: The impact of nanotechnology. *Biosens. Bioelectron.* **87**, 373–387 (2017).

24. Yang, N., Chen, X., Ren, T., Zhang, P. & Yang, D. Carbon nanotube based biosensors. *Sensors Actuators B Chem.* **207**, 690–715 (2015).

25. Wan, Y. *et al.* Carbon nanotube-based ultrasensitive multiplexing electrochemical immunosensor for cancer biomarkers. *Biosens. Bioelectron.* **30**, 93–99 (2011).

26. Xia, Y., Si, J. & Li, Z. Fabrication techniques for microfluidic paper-based analytical devices and their applications for biological testing: A review. *Biosens. Bioelectron.* **77**, 774–789 (2016).

27. Hu, L., Hecht, D. S. & Grüner, G. Percolation in transparent and conducting carbon nanotube networks. *Nano Lett.* **4**, 2513–2517 (2004).

28. Kong, J. *et al.* Nanotube molecular wires as chemical sensors. *Science (80-.).* **287**, 622–625 (2000).

29. Han, J.-W., Kim, B., Li, J. & Meyyappan, M. Carbon nanotube based humidity sensor on cellulose paper. *J. Phys. Chem. C* **116**, 22094–22097 (2012).

30. Carstens, F., Gamelas, J. A. F. & Schabel, S. Engineering microfluidic papers: determination of fibre source and paper sheet properties and their influence on capillary-driven fluid flow. *Cellulose* **24**, 295–309 (2017).

31. Ingrosso, C. *et al.* Surface chemical functionalization of single walled carbon nanotubes with a bacteriorhodopsin mutant. *Nanoscale* **4**, 6434–6441 (2012).

32. Liu, H., Liu, Y. & Zhu, D. Chemical doping of graphene. *J. Mater. Chem.* **21**, 3335–3345 (2011).

33. Zhou, C., Kong, J., Yenilmez, E. & Dai, H. Modulated chemical doping of individual carbon nanotubes. *Science (80-.).* **290**, 1552–1555 (2000).

34. Attar, A. M. *et al.* Electrochemical Quantification of Glycated and Non-glycated Human Serum Albumin in Synthetic Urine. *ACS Appl. Mater. Interfaces* **11**, 4757–4765 (2019).

35. Turner, M. W., Johansson, S. G. O., Barratt, T. M. & Bennich, H. Studies on the levels of immunoglobulins in normal human urine with particular reference to IgE. *Int. Arch. Allergy Immunol.* **37**, 409–417 (1970).

36. Shoorideh, K. & Chui, C. O. On the origin of enhanced sensitivity in nanoscale FET-based biosensors. *Proc. Natl. Acad. Sci.* **111**, 5111–5116 (2014).

37. Food & Administration, D. 510 (k) substantial equivalence determination decision summary assay and instrument combination template. *Food Drug Adm. Rockville, MD. http//www. accessdata. fda. gov/cdrh_docs/reviews K* **130914**, (2008).

38. Kim, B. & Kim, T. H. Determination of human serum albumin using a single-walled carbon nanotube-FET modified with bromocresol green. *Microchim. Acta* **183**, 1513–1518 (2016).

39. Liao, C. *et al.* A specific and biocompatible fluorescent sensor based on the hybrid of GFP chromophore and peptide for HSA detection. *Biosens. Bioelectron.* **86**, 489–495 (2016).

40. Li, J. *et al.* A dual functional fluorescent sensor for human serum albumin and chitosan. *Sensors Actuators B Chem.* **243**, 831–837 (2017).

41. Cid, C. C., Riu, J., Maroto, A. & Rius, F. X. Carbon nanotube field effect transistors for the fast and selective detection of human immunoglobulin G. *Analyst* **133**, 1005–1008 (2008).

42. Kim, J. P., Lee, B. Y., Hong, S. & Sim, S. J. Ultrasensitive carbon nanotube-based biosensors using antibody-binding fragments. *Anal. Biochem.* **381**, 193–198 (2008).

43. Liu, Q. *et al.* Electrochemiluminescent biosensor with DNA link for selective detection of human IgG based on steric hindrance. *Talanta* **194**, 745–751 (2019).

44. Thunkhamrak, C., Reanpang, P., Ounnunkad, K. & Jakmunee, J. Sequential injection system with amperometric immunosensor for sensitive determination of human immunoglobulin G. *Talanta* **171**, 53–60 (2017).

45. Chen, N., Guo, W., Lin, Z., Wei, Q. & Chen, G. Label-free sensitive luminescence biosensor for immunoglobulin G based on Ag6Au6 ethisterone cluster-estrogen receptor α aggregation and graphene. *Talanta* **185**, 243–248 (2018).

46. Brooks, T. & Keevil, C. W. A simple artificial urine for the growth of urinary pathogens. *Lett. Appl. Microbiol.* **24**, 203–206 (1997).

47. Chu, C.-H. *et al.* Beyond the Debye length in high ionic strength solution: direct protein detection with field-effect transistors (FETs) in human serum. *Sci. Rep.* **7**, 5256 (2017).

48. Kaisti, M. Detection principles of biological and chemical FET sensors. *Biosens. Bioelectron.* **98**, 437–448 (2017).

49. Khan, M. S. *et al.* Electrochemical-digital immunosensor with enhanced sensitivity for detecting human salivary glucocorticoid hormone. *Analyst* **144**, 1448–1457 (2019).

50. Tlili, C., Cella, L. N., Myung, N. V, Shetty, V. & Mulchandani, A. Single-walled carbon nanotube chemoresistive label-free immunosensor for salivary stress biomarkers. *Analyst* **135**, 2637–2642 (2010).

51. Tlili, C., Myung, N. V., Shetty, V. & Mulchandani, A. Label-free, chemiresistor immunosensor for stress biomarker cortisol in saliva. *Biosens. Bioelectron.* **26**, 4382–4386 (2011).

52. Gonzalez-Quintela, A. *et al.* Serum levels of immunoglobulins (IgG, IgA, IgM) in a general adult population and their relationship with alcohol consumption, smoking and common metabolic abnormalities. *Clin. Exp. Immunol.* **151**, 42–50 (2008).

53. Peters Jr, T. *All about albumin: biochemistry, genetics, and medical applications*. (Academic press, 1995).

54. Quinlan, G. J., Martin, G. S. & Evans, T. W. Albumin: biochemical properties and therapeutic potential. *Hepatology* **41**, 1211–1219 (2005).

55. Arduini, F. *et al.* Origami multiple paper-based electrochemical biosensors for pesticide detection. *Biosens. Bioelectron.* **126**, 346–354 (2019).

56. Ding, J., Li, B., Chen, L. & Qin, W. A Three-Dimensional Origami Paper-Based Device for Potentiometric Biosensing. *Angew. Chemie Int. Ed.* **55**, 13033–13037 (2016).

Chapter 5. Development of Paper-Based Ultrasensitive Single-Walled Carbon Nanotubes-Based Chemiresistive Biosensors for Detection of Micro RNAs

5.1 Abstract

Micro RNAs (miRNAs) of 19 to 23 nucleotides has been identified as important biomarkers for many diseases such as cancers. Here, we report an ultrasensitive, highly specific, label-free, and nucleic acid amplification technology (NAAT) -free detection of miRNAs using the inkjet-printed single-walled carbon nanotubes (SWNTs) field-effect transistor (FET) biosensors based on the low-cost and portable paper-based substrate. By the precise inkjet printing, SWNTs ink were deposited in the paper-based hydrophilic patterns to percolate and form the semiconductor networks in paper matrix. The SWNTs were then functionalized with the probe miRNA to hybridize with the target sequences and gave the first electrical response. Then the miRNA duplexes were recognized by the Carnation Italian ringspot virus p19 protein (p19) in a size-dependent manner, giving the amplified electrical signals as the second response. The two-step incubation process confirmed the miRNA duplex formation at the SWNTs surface and amplified the electrical responses by about two folds. As a demonstration, we detected the miRNA-122a, a promising biomarker for the diagnosis of early-stage hepatocellular carcinoma (HCC) in various sample matrices, including phosphate buffers, human serum, and synthetic saliva. We achieved the lowest dateable at 0.1 aM over a wide dynamic range of 0.1 aM to 1 fM, which showed its potential for fast, simple, low-cost, and point-of-care detection of miRNAs for early cancer diagnosis.

5.2 Introduction

Micro RNA (miRNA), a class of small non-coding RNAs of about 22 nucleotides, has been discovered for more than two decades[1]. miRNAs are a series of promising molecules that regulate the gene expressions in the post-transcriptional stage via the interactions with the target message RNAs (mRNAs)[2–4]. Recent studies have revealed the relations between the miRNA levels and a variety of diseases, such as infectious diseases and cancers[3,5–11]. Therefore, the miRNA expression profile can be used as the diagnostic biomarkers[8,12–14].

However, highly sensitive, specific, accurate, and affordable detection of miRNAs at point-of-care and resource-limiting settings is particularly challenging due to their ultralow concentrations in cell, short length with various melting temperatures, and similar sequences to the other members in the miRNA family. Therefore, highly sensitive and specific detection methods need to be developed to accurately measure the miRNA levels in the biological samples. The current methods to detect miRNAs rely on the Northern blot[14–16], RT-PCR[17–21], in situ hybridization (ISH)[22,23], microarray[15,24], and next-generation sequencing (NGS)[25]. These methods have their unique advantages and disadvantages for point-of-care detection. For example, NB is easy to perform but requires radio-labeling; RT-PCR is sensitive but requires thermocyclers for nucleic acid amplification technology (NAATs) and can be expensive and time-consuming for low-resource settings. Overall, the long assay time, low throughput, the requirement of relatively larger amount of the miRNA material, and centralized laboratory infrastructures of the traditional methods limit their use for the affordable, rapid, and accurate point-of-care detection of miRNAs.

To enable the fast detection of miRNAs at ~22 nt in biological samples at clinically relevant level (attomolar) in cell or serum without NAATs, we fabricated the SWNTs FET biosensor with the Carnation Italian ringspot virus p19 protein (p19). Firstly, using the SWNTs semiconductor is beneficial for improving the sensitivity of FET biosensors because SWNTs with high surface areas expose their single-layer surface atoms to the environment, which resulted in large electrical modulations due to the small electrical changes at the nanotube surface. Multiple mechanisms have been studied and the electrostatic gating effect and the Schottky barrier effect are verified as the primary mechanisms in FET biosensors[26]. Electrostatic gating occurs when the charged species absorb and dope on the bulk SWNTs to introduce a modulation of the number of charge carriers in the semiconductors. Schottky barrier effect occurs when the charged molecules absorb at the contact region between the metal contacts and the SWNTs, where the metal work function is modulated and the current between the nanotube and metal contacts is affected. Therefore, SWNTs FET biosensors yield electrical signals upon the affinity binding of charged biomolecules and introduced the conductance/resistance change in the FET sensing channels[27]. Secondly, p19 is a 19 kDa protein obtained from the Carnation Italian ringspot virus that can bind specifically to RNA duplex in a size-dependent and sequence-independent manner[28,29]. The p19 shows the highest binding affinity to 21-23 nt RNA duplex and progressively weaker affinity to shorter or longer miRNA duplexes[30,31]. Therefore, p19 is a very useful binding agent to recognize the miRNA duplexes at proper length with about 22 base pairs.

Previously, our group has reported a ultrasensitive p19-functionalized SWNTs FET biosensor for detecting miRNA-122a, a potential biomarker for hepatocellular carcinoma (HCC) diagnosis, on the silicon chip using the SWNTs FETs[14]. The previous FETs were able to detect miRNA-122a with high sensitivity from 1 aM to 10 fM with a limit of detection (LOD) at 1 aM, and high selectivity against other non-complementary RNAs. However, the fabrication of the biosensor on the silicon wafer relied on the use of lithographic patterning/etching, clean-room infrastructures, bulky instruments, large volumes of organics, and costly silicon wafers. These add up the cost and make it expensive in resource-limited situations. Furthermore, the biosensors fabricated on silicon wafer substrate were not easily disposable and were usually buried in the landfill, which could aggravate the environmental burdens[32,33].

Thus, to develop more affordable diagnostic biosensors, World Health Organization has proposed the ASSURED criteria for developing the diagnostic tests to be affordable, sensitive, specific, user-friendly, rapid and robust, user-friendly, equipment-free, and deliverable to end-users[34]. Therefore, to enable the biosensors meeting the ASSURED criteria, emerging paper-based biosensors are promising with notable advantages: (1) low-cost, (2) easy to fabricate, (3) light weight and portable, (4) minimum instrument requirements, and (5) biocompatible and biodegradable[35–37]. In addition, the porous paper substrate has increased surface area for the percolation of SWNTs network, forming more concave corners of the percolated SWNTs to confer higher sensitivity[38–41]. On the other hand, paper-based biosensors can be fabricated at lower cost by many non-lithographic printing methods, such as microcontact printing, screen printing, flexographic

printing, and inkjet printing[42–46]. Among all, the non-contact drop-on-demand piezoelectric inkjet printing stands out due to its distinctive advantages, such as low-cost, mass fabrication, and rapid fabrication[40,45,47–50].

Herein, this work focused on fabricating the highly sensitive SWNTs FET biosensors in a more cost-effective way of printing that eliminated the use of clean-room setups and related consumables. We utilized the chemiresistor configuration (i.e., FET without the gate electrode) to modulate the device conductance with the same mechanisms in the traditional FETs, such as electrostatic gating effect and Schottky Barrier effect[26]. Chemiresistors output the simple I_D-V_S measurements and channel resistances as the electrical signals. The extent of the changes in the conductance/resistance can be correlated with the number of binding biomolecules and therefore the analyte concentrations. We utilized the drop-on-demand inkjet printing technology to deposit the pyrene carboxylic acid (PCA)-functionalized SWNTs (PCA/SWNTs) ink[51] on the low-cost paper-based substrate with wax-patterned hydrophilic channels. The precise inkjet printing deposited the PCA/SWNTs ink on the paper to form the nanotube network with appropriate network density. To enable the sensitive and specific detection of miRNA-122a, probe RNAs (complementary to miRNA-122a) were immobilized on PCA/SWNTs through the amide bond formation between the carboxylic acid from the PCA molecules and the primary amine groups from the probe RNA. Since the miRNAs are very small molecules and are present at attomolar in biological samples, we need to amplify the electrical responses. We utilized the two-step incubations of the miRNA sample and then the p19 solution. After the sample incubation, the target miRNA-122a binds to the probe RNA and introduced the

first electrical response. Then the second incubation of the p19 allowed the recognition of the miRNA duplex by the p19, which introduced another increase in the electrical response. In this way, we amplified the electrical signal by about two folds for a wide concentration range of miRNA-122a from 0.1 aM to 1 fM. The paper-based chemiresistive biosensors achieved the lowest detectable concentration at 0.1 aM without any NAATs in only two hours. The performances of the optimized paper-based SWNTs biosensor were comparable to our previously reported FET biosensor on silicon chips[14], showing its great potential for early diagnosis of HCC at point-of-care.

5.3 Materials and Methods

5.3.1 Materials

The materials used include the following: Paper substrate (Whatman Grade 1 chromatography paper). Silver ink (JS-A191, NCC nano LLC). SWNTs (P3 grade, Carbon Solutions Inc). 1-Pyrene carboxylic acid (PCA) (P1687, TCI America). (1-Ethyl-3-(3-dimethylaminopropyl) carbodiimide hydrochloride) (EDC) (E7750, Sigma-Aldrich). N-hydroxysuccinimide (NHS) (24500, Thermo Fisher Scientific). Sodium phosphate (monobasic monohydrate) (AC207805000, Thermo Fisher Scientific). Sodium phosphate (dibasic anhydrous) (sx0720-1, Millipore Sigma). Ethanolamine (411000, Sigma-Aldrich). Tween-20 (1706531, BioRad). Dimethylformamide (DMF) (GEN002007, Thermo Fisher Scientific). Milli-Q (Milli-Q IQ 7000 system). miRNAs were purchased from IDT: miRNA-122a (5′-pUGG AGU GUG ACA AUG GUG UUU G-3′), probe RNA (5′-pAAC ACC AUU GUC ACA CUC CAU A-NH2-3′), and miRNA-32 (5′-pUAU UGC ACA

UUA CUA AGU UGC A-3′). Human serum was obtained from Sigma-Aldrich (H4522). Saliva was synthesized according to the reported formulation[52], which consisted of 0.6 g/L of sodium phosphate dibasic, 0.6 g/L of anhydrous calcium chloride, 0.4 g/L of potassium chloride, 0.4 g/L of sodium chloride, 4 g/L of mucin and 4 g/L of urea dissolved in DI water with pH adjusted to 7.4.

5.3.2 Inkjet Printing and Wax Printing

Silver nanoparticle ink and the PCA/SWNTs ink were all printed using the piezoelectric inkjet printer (DMP-2831, Fujifilm) with the 10 pL cartridges (DMC-11610). The silver source-drain electrodes were designed as the interdigitated electrodes with the finger spacing of ~ 86 μm. Silver leads were baked at 150 ˚C for 2 hours to be highly conductive (less than 1 Ω per square). PCA (0.5 mg/mL) and SWNTs (1 mg/mL) were dispersed in DMF and stirred for overnight and centrifuged (10 min @ 5000 rpm) to obtain the supernatant ink. The PCA/SWNTs ink was printed 3 to 4 layers to obtain a SWNTs network with a printed dry resistance of 17.3 ± 4.4 kΩ. Wax printing was conducted by the wax printer (ColorQube 8580DN, Xerox). The wax pattern can be melted at 170 ˚C for 5 min to penetrate into the paper matrix and formed the hydrophobic barriers. A second wax printing without melting was applied on the back side of the paper to form a solid wax layer.

5.3.3 Functionalization of Paper-Based Biosensor

The PCA/SWNTs were functionalized with the probe miRNA by firstly incubating the PCA/SWNTs with EDC and NHS both at 20 mg/mL in 0.1 M MES (pH 5.5) for 30 min to activate the carboxylic groups. The washing process was conducted on a vacuum filtration glass frit, with washing buffer (10 mM phosphate buffer at pH 7.4, denoted as PB thereafter) drop-casted on the paper-based biosensors and transported vertically through the sensors under vacuum force. After washing with PB, the sensors were incubated with the probe miRNA at 1 μM in PB for overnight. Then after PB wash, the sensors were incubated with 0.1 M ethanolamine and 0.1 wt% Tween 20 in PB each for 30 min to quench the unreacted chemical moieties and block the bare sites on SWNTs to prevent the non-specific adsorption, respectively, followed by through washing with PB.

5.3.4 Sensing Protocol and Electrical Measurements

Samples spiked with target miRNAs (miRNA-122a), non-target miRNAs (miRNA-32), samples without spiked RNAs (PB blank, serum blank, and saliva blank) were incubated with the biosensors for a certain length of time (15 min to 2 hours) at controlled temperature (25 ˚C or 37 ˚C). The sample matrices were 10 mM PB (pH 7.4), human serum, and synthetic saliva (pH 7.4). Each biosensor was incubated with samples and washed thoroughly with PB immediately before electrical measurement to maintain the maximum humidity. Then the biosensors were then incubated with the p19 protein (1000 U/mL in PB) at 25 ˚C for 1 hour and washed thoroughly with PB immediately before the second immediate electrical measurement. All electrical measurements were conducted using the

Keithley source meter (model 2636) with a source-drain voltage from -0.1 V to 0.1 V and the resistance was obtained.

5.4 Results and Discussions

5.4.1 Paper-Based Hydrophilic Pattern Base

We firstly patterned the paper substrate with silver electrical leads for the convenient measurement of the resistance of the semiconductor biosensors. Since paper is a porous substrate, it requires several layers of inkjet printing of the silver nanoparticle ink and heat annealing to achieve the highly conductive silver leads. Thus, the inkjet printing of silver was optimized by printing 5 layers. They provided a negligible resistance with a low sheet resistance of less than 1 Ω per square after annealing. Therefore, the resistance measurement was regarded as the resistance from the biosensor instead of the silver leads.

Next, to accommodate the liquid samples during the incubations, paper substrate was patterned with wax barriers to form the hydrophobic confinement (e.g., hydrophilic channels). As shown in **Figure 5.1**, The pattern had the following features: (1) The 5-petal shaped hydrophilic channel was able to equally distribute the liquid to the five biosensors. (2) There was a bulged circular area for each sensor to accommodate more solution during the incubation. In addition, the bulged area allowed more space for the printing pattern alignment of silver leads, PCA/SWNTs, and wax pattern. (3) Each channel end was left hydrophilic for bulk liquid removal via the vertical vacuum filtration. Further, it can be used as a vertical liquid transportation portal when integrated with timed microfluidics. (4) A second wax printing was applied to the backside of the paper without melting. The solid

wax layer served as a hydrophobic wax seal to prevent liquid migration due to gravity. Moreover, the wax seal strengthened the mechanical toughness of the paper-based devices.

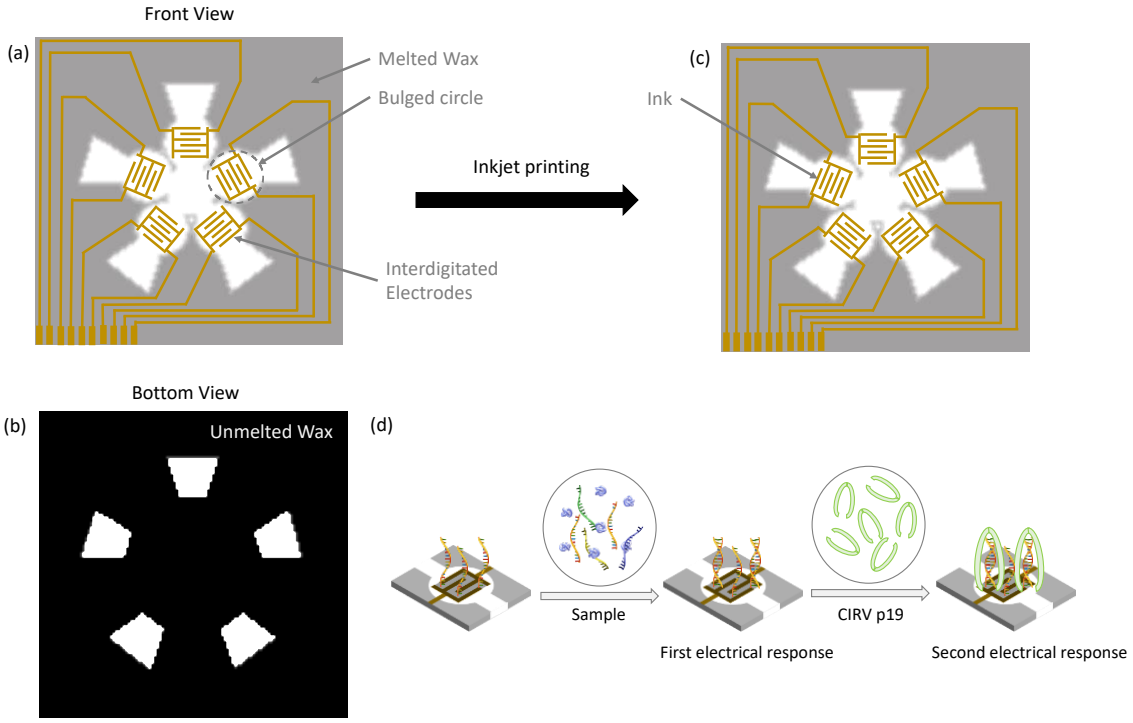

Figure 5.1. Illustration paper-based biosensor fabrication and sensing protocol. (a) Front view of the paper-based biosensor pattern before inkjet printing of PCA/SWNTs. (b) Bottom view of the paper-based biosensor pattern. (c) Front view of the paper-based biosensor after inkjet printing of PCA/SWNTs. (d) Illustration of the two-step incubation sensing protocol for the paper-based biosensor to detect miRNA-122a with amplified signals by using p19.

5.4.2 Inkjet Printing of PCA/SWNTs and Fabrication of Biosensor

The inkjet printing process of the PCA/SWNTs was critical in controlling the network density formed in the paper-based substrate. The ink droplets were created by the piezoelectric inkjet printer DMP-2831 and were deposited on the porous paper, where the nanotubes with large length-to-diameter ratios percolated into the paper matrix and formed a semi-3D network. Since the SWNTs used in this study was a mixture of semiconducting SWNTs (~ 67%) and metallic SWNTs (~ 33%), the density of the nanotube network should

be in between the two extremes cases of too sparse or too dense networks. When the network is too sparse, the electronic pathways are sparse and result in a very low current density and thus an unstable reading of the ultrahigh resistance[40,53]. In this study, we found the sparse network by 1 layer printing showed very high resistance in millions of Ωs (data not shown). In addition, the sparse network does not provide sufficient bioconjugation sites and therefore insufficient binding sites for the hybridization of the target miRNAs. On the other hand, when the network is too dense, the metallic SWNTs form metallic connections and their emitting sites reach to a level close to that of a flat metal plate[40,53], which short-circuits the semiconducting SWNTs. Hence, the bio-recognition events would not be transduced through the electrical resistance change. As a result, the sensitivity would be poor for the two extreme cases. Thus, we fabricated the sensors with a medium network density that showed a dry resistance at about 17.3 ± 4.4 kΩ after inkjet printing of 3 to 4 layers of PCA/SWNTs ink. After the EDS/NHS activation, probe miRNAs functionalization, and the quenching and blocking process, the wet resistance increased to 58.5 ± 2.44 kΩ, 62.3 ± 9.75 kΩ, and 75.7 ± 19.9 kΩ, respectively, which indicated the successful functionalizations of the biosensors.

5.4.3 Optimization of Sensing Protocol

We evaluated and optimized the biosensing performance using the two-step incubations to amplify the electrical responses. The first step was the incubation of the miRNA sample. The p-typed SWNTs network at dry condition was primed with the aqueous sample matrix was believed to be counter-doped by the adsorption of the n-doping

water molecules in the buffer[38,40,54–56]. The target sequences, if present, hybridized with the probe RNA near the surface of the SWNTs (**Figure 5.1**). Since the target miRNAs carried additional negative charges through its phosphate backbone[2,57], they possibly behaved as electron acceptors and repelled the electron carriers in the semiconducting channels[40,54–56]. As a result, increases in the resistance were observed and they were normalized as the relative change in the resistance as the electrical responses, i.e., the signals as $\Delta R/R_0$, where R_0 was the resistance before sample incubation and ΔR was the resistance change after incubations.

Next, the SWNTs biosensors were incubated with the p19 solution at 1000 U/mL at 25 ˚C for 1h (**Figure 5.1**). The p19 tightly binds to the miRNA duplex at a length of ~ 22 nt and therefore was able to recognize the miRNA duplex on the SWNTs surface. After washing and removing excessive p19 molecules, the resistance further increased due to the additional negative charge of the bound p19 proteins. Furthermore, the binding of the p19 to the miRNA duplex might also introduced the disruption of the SWNT network continuity due to the larger size of the p19 protein compared to the miRNAs, and thus increased the resistance[58,59]. As a result, higher electrical responses were seen as an amplifier for the miRNA recognition by about two folds (**Figure 5.2**).

To achieve the highest sensitivity for the paper-based biosensor, the temperature and time for the miRNA sample incubation were optimized. miRNA-122a in PB with increasing concentrations from 0.1 aM to 1 fM was incubated with the FET biosensors at 25 ˚C or 37 ˚C for 1 hour. The responses were showed in **Figure 5.2**. At 25 ˚C, miRNA-122a incubation without p19 showed a sensitivity of 7.83% per decade, while at 37 ˚C the

sensitivity raised by ~33% to 10.42% per decade. This increase in the signal and sensitivity can be attributed to the effect of higher temperature on the nucleic acid hybridization. At elevated temperature of 37 ˚C, the uncoiling of the nucleic acid strands lead to the higher accessibility between the probe and the target sequences, which resulted in an improved hybridization efficiency[14,60]. Furthermore, the elevated temperature also benefited the mass transportation (diffusion) during the 1-hour incubation and contributed to a higher hybridization efficiency. Moreover, the increased responses in the first incubation with miRNA-122a samples were confirmed by the increased signals after the second incubation step with p19 protein. As shown in **Figure 5.2**, at 25 ˚C, with the p19 binding to the miRNA duplexes, the electrical responses increased by about two folds and showed a sensitivity of 27.13% per decade. At 37 ˚C, the sensitivity of the p19-binded responses also increased by about 2 folds and showed a sensitivity of 35.32% per decade, which was ~ 30% higher than that at 25 ˚C, agreeing with the ~ 33% increase in the sensitivity to only the miRNA samples. Thus, 37 ˚C was selected as the incubation temperature for the miRNA samples (first incubation) to achieve the highest electrical responses, while the 1-hour incubation of the p19 protein (second incubation) was maintained at 25 ˚C.

The optimum incubation time for the miRNA samples at 37 ˚C was also investigated. With various incubation time from 15 min to 2 hours, the concentration of miRNA-122a was fixed at 1 aM to investigate the effect of incubation time on the responses. As shown in **Figure 5.3**, the responses from the incubations of the miRNA-122a increased with respect to increasing incubation time. After the second incubation with the p19, the responses further increased by about two folds to amplify the electrical signals. The

electrical responses reached a plateau after the 1-hour incubation of the miRNA samples with or without p19, which was ascribed to the limited hybridization sites being saturated on the biosensor. Therefore, the optimum incubation condition was selected as the 1-hour incubation of the miRNA samples at 37 ˚C, followed by 1-hour p19 incubation at 25 ˚C. Under the optimized condition, we obtained the calibration curve for the detection of miRNA-122a in PB, as shown in **Figure 5.2b**. The biosensor was responsive for a wide dynamic range from 0.1 aM to 1 fM with a lowest detectable at 0.1 aM without NAATs, which was comparable to the dynamic range and detection limit from our previous study on silicon-based FET biosensor[14].

Moreover, negative controls were conducted on the paper-based biosensor to study the specificity. Firstly, the biosensors were incubated with PB as the blank (without miRNA) at 37 ˚C for 1 hour, then incubated with the p19 for another hour at 25 ˚C. The biosensors showed negligible responses for both incubation steps (0.47% for PB and 8.31% for PB and p19). This confirmed that the non-specific adsorption of p19 on SWNTs was negligible and was not the cause for the amplified electrical responses. The specificity of the paper-based biosensor was evaluated by incubating with the non-complementary miRNA (miRNA-32 at 1 fM in PB) and p19. The responses were compared to the miRNA-122a samples at 1 fM in PB and p19. As shown in **Figure 5.4**, even after the p19 incubation, the miRNA-32 in PB only introduced low changes in the resistance at 7.39%. On the other hand, the target sequences miRNA-122a at 1 fM gave a high response of 179.1% change in resistance after the p19 incubation. This confirmed the high specificity of the biosensor

due to the specific hybridization between the probe RNA and the target RNA, in addition to the length-dependent binding of the p19 to the miRNA duplexes.

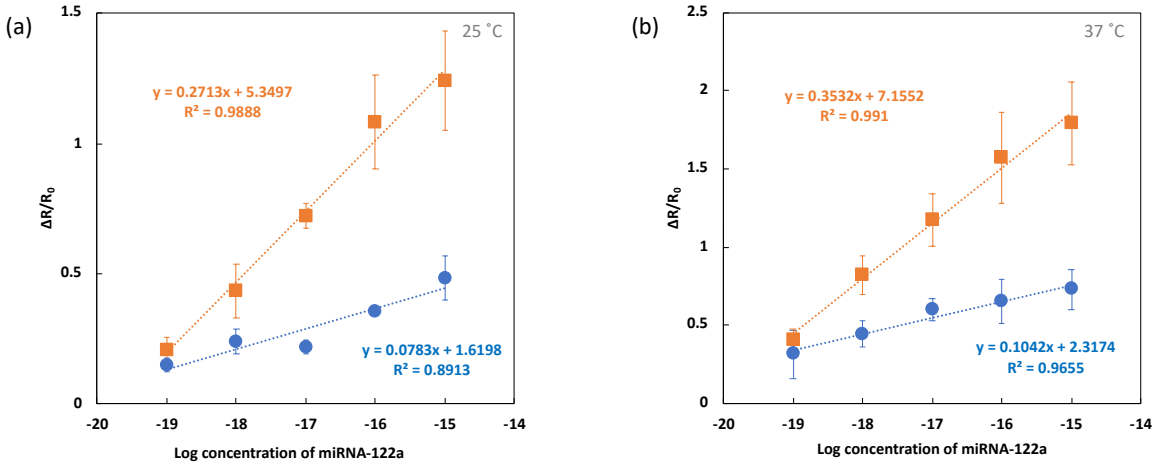

Figure 5.2 Electrical responses from the two-step incubation protocol. miRNA-122a in PB sample incubations (blue circles) for 1 hour at different temperatures of (a) 25 ˚C and (b) 37 ˚C, followed by the p19 incubation (orange squares) for 1 hour at 25 ˚C. Data and error bars represent the average ± SD over 4 individual sensors.

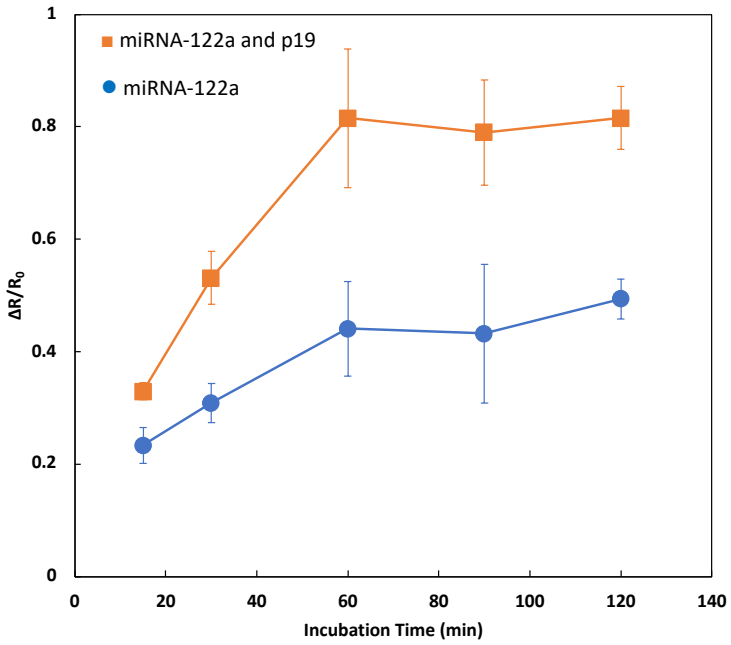

Figure 5.3 Two-step responses from the 37 ˚C incubations of miRNA-122a in PB samples (1 aM, blue circles) with various incubation time from 15 min to 2 hours, and the following incubations of the p19 for 1 hour at 25 ˚C (orange squares). Data and error bars represent the average ± SD over 4 individual sensors.

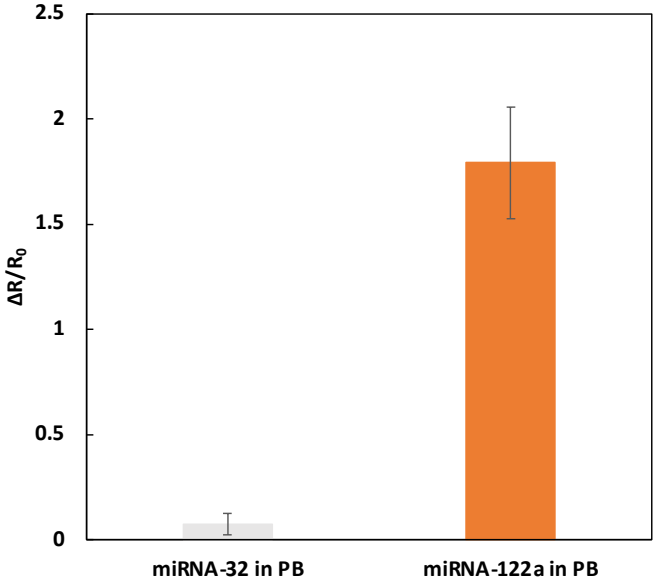

Figure 5.4 Paper-based biosensor specificity. Responses shows the different electrical resistance changes from incubations of miRNA-32 (1 fM in PB) or miRNA-122a (1 fM in PB) for 1 hour at 37 ˚C, followed by the p19 incubations for 1 hour at 25 ˚C. Data and error bars represent the average ± SD over 4 individual sensors.

5.4.4 Detection of Micro RNA-122a in Complicated Matrices

To explore the prospective application of the paper-based biosensor in clinical use, we tested the paper-based biosensor with the human serum and synthetic saliva samples spiked with the target sequences (miRNA-122a) or the non-target sequences (miRNA-32). Following the optimum sensing conditions of the two-step incubations, the electrical responses from human serum samples and synthetic saliva samples were shown in **Figure 5.5** and **Figure 5.6**, respectively. Firstly, we tested the biosensors with the serum samples not spiked with miRNAs. The serum matrix, after the p19 incubation, introduced a ~ 13% higher response (21.67%) than the PB blank with p19 incubation (8.31%). The ~ 13% higher response was also seen in the serum spiked with miRNA-32 after the p19 incubation at 19.14%, while the miRNA-32 in PB introduced only 7.39% response after the p19 incubation. Moreover, for the serum samples spiked with miRNA-122a, the parallelly higher responses were observed for all the concentrations (**Figure 5.5b**). Therefore, the ~13% higher responses were therefore attributed to the serum matrix for two possible reasons: (1) the serum was obtained from a healthy donor that naturally contained a certain level of miRNA-122a that was consistently detected by our biosensors[5,12]; (2) the miscellaneous components in the serum matrix might introduce some non-specific adsorption and thus a consistent increase in the electrical responses. Nevertheless, the increase in the background did not affect the sensitivity of the biosensor. As seen in **Figure 5.5b**, the sensitivity to the miRNA-122a spiked in serum was 9.47% per decade, which was 91% of the sensitivity of the sensitivity in PB samples; the sensitivity after the p19 incubation was 34.07% per decade, which was 96% of the sensitivity in PB matrix. These

results suggested the comparable performance of the paper-based biosensor for the serum samples, which showed its great potential in early diagnosis for cancers, such as HCC.

Unlike the serum samples, saliva is a non-invasive sample that can be easily collected and can be a great sample source for the point-of-care tests. To show the potential of the paper-based biosensor with the non-invasive samples, the synthetic saliva samples spiked with miRNA-122a or miRNA-32 were tested. With the p19 incubation, the synthetic saliva spiked with the non-target miRNA-32 at 1 fM introduced a similar background response (9.57%) compared to the PB blank (8.31%) as well as PB spiked with miRNA-32 at 1 fM (7.29%), which was negligible compared to the saliva spiked with the 1 fM miRNA-122a after p19 incubation (193.8%) (**Figure 5.6a**). The results showed great specificity to the target miRNA-122a in the salivary matrix. Furthermore, as shown in **Figure 5.6b**, the biosensor incubated with the saliva samples spiked with increasing concentrations of miRNA-122a were showing comparable sensitivity of 10.27% per decade, which was 98.5% of the sensitivity in PB. After the second incubation with the p19 protein, the electrical responses were amplified by about two folds and the sensitivity was 31.8% per decade, which was 90% of the sensitivity in PB. These results confirmed the great potential of the paper-based biosensor in the diagnostic application of detecting miRNAs in non-invasive saliva samples.

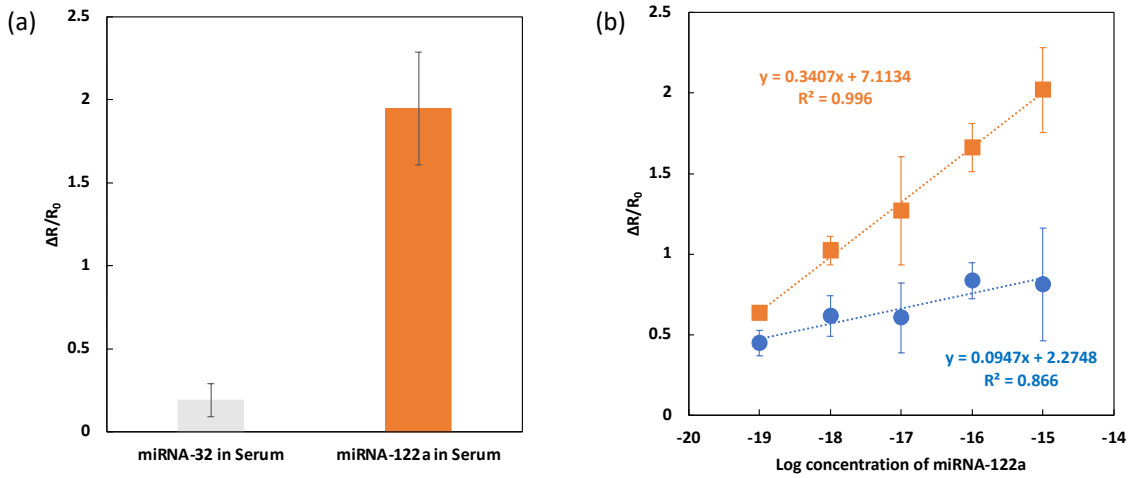

Figure 5.5 Responses from the serum samples. (a) Paper-based biosensor specificity to the two-step incubations of serum samples spiked with miRNA-32 (1 fM) or miRNA-122a (1 fM) for 1 hour at 37 ˚C, followed by the p19 incubation for 1 hour at 25 ˚C. (b) Responses from the serum samples spiked with miRNA-122a (blue circles) for 1 hour at 37 ˚C, and after the p19 incubations (orange squares) for 1 hour at 25 ˚C. Data and error bars represent the average ± SD over 4 individual sensors.

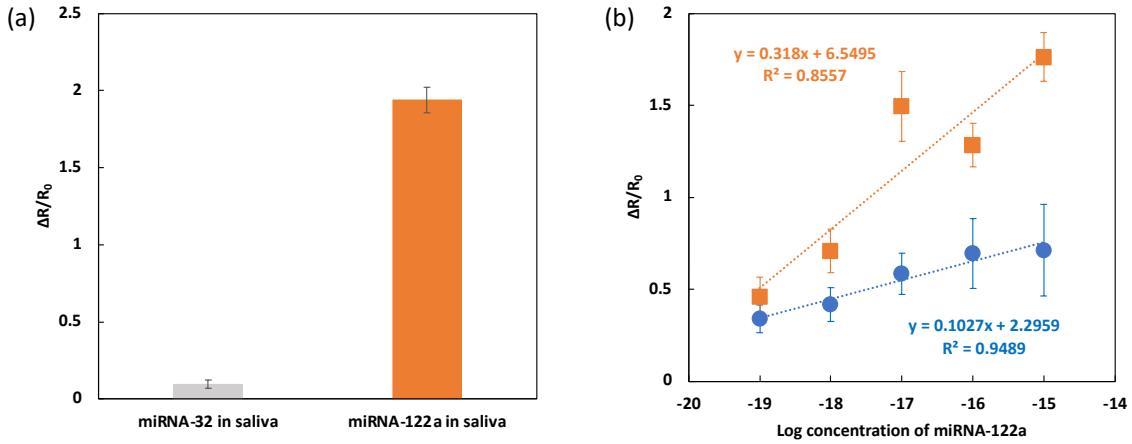

Figure 5.6 Responses from the synthetic saliva samples. (a) Paper-based biosensor specificity to the incubation of synthetic saliva samples spiked with miRNA-32 (1 fM) and miRNA-122a (1 fM) for 1h at 37 ˚C, followed by the p19 incubation for 1 hour for 25 ˚C. (b) Responses from the synthetic saliva samples spiked with miRNA-122a (blue circles) for 1 hour at 37 ˚C, and after the p19 incubations (orange squares) for 1 hour at 25 ˚C. Data and error bars represent the average ± SD over 4 individual sensors.

5.5 Conclusions

In conclusion, we developed a facile and affordable method to fabricate the paper-based FET/chemiresistor biosensor for the sensitive, specific, and quick detection of miRNA-122a at attomolar level for potential point-of-care diagnosis of HCC. The paper substrate was inkjet-printed with silver leads and wax prints to accommodate the SWNTs networks. The SWNTs were firstly functionalized with PCA molecules and inkjet-printed to form a carbon nanotube network in paper matrix. The immobilization of the probe RNAs made the paper-based biosensor highly sensitive and specific to the target sequences. Under the optimized incubation time and temperature for the miRNA samples (first incubation), we observed a high dependence between the electrical response and the miRNA-122a concentration. The electrical responses were further amplified by about two folds upon the incubation with the CIRV p19 protein, which specifically recognized the 22-bp long RNA duplexes (second incubation). A wide dynamic range of miRNA-122a from 0.1 aM to 1 fM and a lowest detectable at 0.1 aM in PB were achieved. This low detection limit was achieved without NAATs and was well below the levels of interest for biomedical diagnostics even with dilutions. The methodology developed in this report showed its potential to be integrated with fully developed microfluidics and portable electronics to further improve the sensing procedure for point-of-care use.

5.6 References

1. Lee, R. C., Feinbaum, R. L. & Ambros, V. The C. elegans heterochronic gene lin-4 encodes small RNAs with antisense complementarity to lin-14. *Cell* **75**, 843–854 (1993).

2. Cadoni, E., Manicardi, A. & Madder, A. PNA-based microRNA detection methodologies. *Molecules* **25**, 1296 (2020).

3. Tribolet, L. *et al.* MicroRNA biomarkers for infectious diseases: From basic research to biosensing. *Front. Microbiol.* **11**, (2020).

4. Wang, Q. *et al.* Briefing in family characteristics of microRNAs and their applications in cancer research. *Biochim. Biophys. Acta (BBA)-Proteins Proteomics* **1844**, 191–197 (2014).

5. Gramantieri, L. *et al.* Cyclin G1 is a target of miR-122a, a microRNA frequently down-regulated in human hepatocellular carcinoma. *Cancer Res.* **67**, 6092–6099 (2007).

6. Hayes, J., Peruzzi, P. P. & Lawler, S. MicroRNAs in cancer: biomarkers, functions and therapy. *Trends Mol. Med.* **20**, 460–469 (2014).

7. Jeffrey, S. S. Cancer biomarker profiling with microRNAs. *Nat. Biotechnol.* **26**, 400–401 (2008).

8. Lu, J. *et al.* MicroRNA expression profiles classify human cancers. *Nature* **435**, 834–838 (2005).

9. Ojha, R., Nandani, R., Pandey, R. K., Mishra, A. & Prajapati, V. K. Emerging role of circulating microRNA in the diagnosis of human infectious diseases. *J. Cell. Physiol.* **234**, 1030–1043 (2019).

10. Verma, P., Pandey, R. K., Prajapati, P. & Prajapati, V. K. Circulating microRNAs: potential and emerging biomarkers for diagnosis of human infectious diseases. *Front. Microbiol.* **7**, 1274 (2016).

11. Xue, X., Zhao, Y., Wang, X., Qin, L. & Hu, R. Development and validation of serum exosomal microRNAs as diagnostic and prognostic biomarkers for hepatocellular carcinoma. *J. Cell. Biochem.* **120**, 135–142 (2019).

12. Luo, J. *et al.* Circulating microRNA-122a as a diagnostic marker for hepatocellular carcinoma. *Onco. Targets. Ther.* **6**, 577 (2013).

13. Peng, C. *et al.* Circulating microRNAs for the diagnosis of hepatocellular carcinoma. *Dig. Liver Dis.* **51**, 621–631 (2019).

14. Ramnani, P., Gao, Y., Ozsoz, M. & Mulchandani, A. Electronic detection of microRNA at attomolar level with high specificity. *Anal. Chem.* **85**, 8061–8064 (2013).

15. Dave, V. P. *et al.* MicroRNA amplification and detection technologies: opportunities and challenges for point of care diagnostics. *Lab. Investig.* **99**, 452–469 (2019).

16. Várallyay, E., Burgyán, J. & Havelda, Z. MicroRNA detection by northern blotting using locked nucleic acid probes. *Nat. Protoc.* **3**, 190 (2008).

17. Androvic, P., Valihrach, L., Elling, J., Sjoback, R. & Kubista, M. Two-tailed RT-qPCR: a novel method for highly accurate miRNA quantification. *Nucleic Acids Res.* **45**, e144–e144 (2017).

18. Chen, C. *et al.* Real-time quantification of microRNAs by stem–loop RT–PCR. *Nucleic Acids Res.* **33**, e179–e179 (2005).

19. Huang, T. *et al.* Quantification of mature microRNAs using pincer probes and real-time PCR amplification. *PLoS One* **10**, e0120160 (2015).

20. Mei, Q. *et al.* A facile and specific assay for quantifying microRNA by an optimized RT-qPCR approach. *PLoS One* **7**, e46890 (2012).

21. Shi, R. & Chiang, V. L. Facile means for quantifying microRNA expression by real-time PCR. *Biotechniques* **39**, 519–525 (2005).

22. Hanna, J. A. *et al.* Quantitative analysis of microRNAs in tissue microarrays by in situ hybridization. *Biotechniques* **52**, 235–245 (2012).

23. Nelson, P. T. *et al.* RAKE and LNA-ISH reveal microRNA expression and localization in archival human brain. *Rna* **12**, 187–191 (2006).

24. Yin, J. Q., Zhao, R. C. & Morris, K. V. Profiling microRNA expression with microarrays. *Trends Biotechnol.* **26**, 70–76 (2008).

25. Moldovan, L. *et al.* Methodological challenges in utilizing mi RNA s as circulating biomarkers. *J. Cell. Mol. Med.* **18**, 371–390 (2014).

26. Heller, I. *et al.* Identifying the mechanism of biosensing with carbon nanotube transistors. *Nano Lett.* **8**, 591–595 (2008).

27. Tran, T.-T. & Mulchandani, A. Carbon nanotubes and graphene nano field-effect transistor-based biosensors. *TrAC Trends Anal. Chem.* **79**, 222–232 (2016).

28. Nasheri, N. *et al.* An enzyme-linked assay for the rapid quantification of microRNAs based on the viral suppressor of RNA silencing protein p19. *Anal. Biochem.* **412**, 165–172 (2011).

29. Vargason, J. M., Szittya, G., Burgyán, J. & Hall, T. M. T. Size selective recognition of siRNA by an RNA silencing suppressor. *Cell* **115**, 799–811 (2003).

30. Kilic, T., Topkaya, S. N. & Ozsoz, M. A new insight into electrochemical microRNA detection: a molecular caliper, p19 protein. *Biosens. Bioelectron.* **48**, 165–171 (2013).

31. Torrente-Rodríguez, R. M. *et al.* Direct determination of miR-21 in total RNA extracted from breast cancer samples using magnetosensing platforms and the p19 viral protein as detector bioreceptor. *Electroanalysis* **26**, 2080–2087 (2014).

32. Deng, R., Chang, N. L., Ouyang, Z. & Chong, C. M. A techno-economic review of silicon photovoltaic module recycling. *Renew. Sustain. Energy Rev.* **109**, 532–550 (2019).

33. Kiddee, P., Pradhan, J. K., Mandal, S., Biswas, J. K. & Sarkar, B. An overview of treatment technologies of E-waste. *Handb. Electron. Waste Manag.* 1–18 (2020).

34. Land, K. J., Boeras, D. I., Chen, X.-S., Ramsay, A. R. & Peeling, R. W. REASSURED diagnostics to inform disease control strategies, strengthen health systems and improve patient outcomes. *Nat. Microbiol.* **4**, 46–54 (2019).

35. Ge, X. *et al.* Nanomaterial-enhanced paper-based biosensors. *TrAC Trends Anal. Chem.* **58**, 31–39 (2014).

36. Lee, V. B. C., Mohd-Naim, N. F., Tamiya, E. & Ahmed, M. U. Trends in paper-based electrochemical biosensors: from design to application. *Anal. Sci.* **34**, 7–18 (2018).

37. Mahato, K., Srivastava, A. & Chandra, P. Paper based diagnostics for personalized health care: emerging technologies and commercial aspects. *Biosens. Bioelectron.* **96**, 246–259 (2017).

38. Han, J.-W., Kim, B., Li, J. & Meyyappan, M. Carbon nanotube based humidity sensor on cellulose paper. *J. Phys. Chem. C* **116**, 22094–22097 (2012).

39. Sarfraz, J., Tobjork, D., Osterbacka, R. & Linden, M. Low-cost hydrogen sulfide gas sensor on paper substrates: fabrication and demonstration. *IEEE Sens. J.* **12**, 1973–1978 (2011).

40. Shen, Y., Modha, S., Tsutsui, H. & Mulchandani, A. An origami electrical biosensor for multiplexed analyte detection in body fluids. *Biosens. Bioelectron.* **171**, 112721 (2021).

41. Shoorideh, K. & Chui, C. O. On the origin of enhanced sensitivity in nanoscale FET-based biosensors. *Proc. Natl. Acad. Sci.* **111**, 5111–5116 (2014).

42. Dilfer, S., Hoffmann, R. C. & Dörsam, E. Characteristics of flexographic printed indium–zinc-oxide thin films as an active semiconductor layer in thin film field-effect transistors. *Appl. Surf. Sci.* **320**, 634–642 (2014).

43. Hambsch, M. *et al.* Uniformity of fully gravure printed organic field-effect transistors. *Mater. Sci. Eng. B* **170**, 93–98 (2010).

44. Härting, M., Zhang, J., Gamota, D. R. & Britton, D. T. Fully printed silicon field effect transistors. *Appl. Phys. Lett.* **94**, 193509 (2009).

45. Hossain, R. F. & Kaul, A. B. Inkjet-printed MoS2-based field-effect transistors with graphene and hexagonal boron nitride inks. *J. Vac. Sci. Technol. B, Nanotechnol. Microelectron. Mater. Process. Meas. Phenom.* **38**, 42206 (2020).

46. Mehlich, J., Miyata, Y., Shinohara, H. & Ravoo, B. J. Fabrication of a Carbon-Nanotube-Based Field-Effect Transistor by Microcontact Printing. *Small* **8**, 2258–2263 (2012).

47. Fang, X. *et al.* Patterning Liquid Crystalline Organic Semiconductors via Inkjet Printing for High-Performance Transistor Arrays and Circuits. *Adv. Funct. Mater.* 2100237 (2021).

48. Jiang, Z. *et al.* All-inkjet-printed MoS 2 field-effect transistors on paper for low-cost and flexible electronics. *Appl. Nanosci.* **10**, 3649–3658 (2020).

49. Lim, S. *et al.* Inkjet-printed reduced graphene oxide/poly (vinyl alcohol) composite electrodes for flexible transparent organic field-effect transistors. *J. Phys. Chem. C* **116**, 7520–7525 (2012).

50. Medina-Sánchez, M., Martínez-Domingo, C., Ramon, E. & Merkoçi, A. An Inkjet-Printed Field-Effect Transistor for Label-Free Biosensing. *Adv. Funct. Mater.* **24**, 6291–6302 (2014).

51. Shen, Y., Tran, T.-T., Modha, S., Tsutsui, H. & Mulchandani, A. A paper-based chemiresistive biosensor employing single-walled carbon nanotubes for low-cost, point-of-care detection. *Biosens. Bioelectron.* **130**, 367–373 (2019).

52. Wordofa, D. N., Ramnani, P., Tran, T. T. & Mulchandani, A. An oligonucleotide-functionalized carbon nanotube chemiresistor for sensitive detection of mercury in saliva. *Analyst* **141**, 2756–2760 (2016).

53. Xu, T. *et al.* Reduced graphene oxide/carbon nanotube hybrid fibers with narrowly distributed mesopores for flexible supercapacitors with high volumetric capacitances and satisfactory durability. *Carbon N. Y.* **152**, 134–143 (2019).

54. Ingrosso, C. *et al.* Surface chemical functionalization of single walled carbon nanotubes with a bacteriorhodopsin mutant. *Nanoscale* **4**, 6434–6441 (2012).

55. Liu, H., Liu, Y. & Zhu, D. Chemical doping of graphene. *J. Mater. Chem.* **21**, 3335–3345 (2011).

56. Zhou, C., Kong, J., Yenilmez, E. & Dai, H. Modulated chemical doping of individual carbon nanotubes. *Science (80-.).* **290**, 1552–1555 (2000).

57. Liu, L., Wei, Y., Jiao, S., Zhu, S. & Liu, X. A novel label-free strategy for the ultrasensitive miRNA-182 detection based on MoS2/Ti3C2 nanohybrids. *Biosens. Bioelectron.* **137**, 45–51 (2019).

58. Bruck, H. A., Yang, M., Kostov, Y. & Rasooly, A. Electrical percolation based biosensors. *Methods* **63**, 282–289 (2013).

59. Yang, M., Sun, S., Bruck, H. A., Kostov, Y. & Rasooly, A. Electrical percolation-based biosensor for real-time direct detection of staphylococcal enterotoxin B (SEB). *Biosens. Bioelectron.* **25**, 2573–2578 (2010).

60. Wallace, R. B. *et al.* Hybridization of synthetic oligodeoxyribonucleotides to Φ X 174 DNA: the effect of single base pair mismatch. *Nucleic Acids Res.* **6**, 3543–3558 (1979).

Chapter 6. Conclusions

6.1 Summary

The goal of this research was to develop the affordable paper-based microfluidic chemiresistive biosensor employing SWCNTs for the label-free, sensitive, and specific detection of important disease biomarkers, including human serum albumin, human immunoglobin G, and micro RNAs. To develop the chemiresistor (field-effect transistor eliminating the gate electrode) biosensors on paper, facile vacuum filtration, inkjet printer, and wax printing was preferred to pattern the chemiresistor biosensor arrays on paper. To reach the goal, SWCNTs were firstly modified with PCA molecules to prepare the PCA/SWCNTs ink for the controlled deposition on paper. Vacuum filtration deposition and inkjet printing deposition were optimized to fabricate the chemiresistors on paper with proper network density that delivered maximum sensitivity for the biosensors. Secondly, this research developed paper-based microfluidics by a facile wax printing method with vertical and lateral microflows to deliver the reagents of buffers and samples for the biosensing process. With optimized parameters, the biosensors were able to detect diseases biomarkers at low levels in various sample matrices, including buffers, artificial urine, artificial saliva, human serum, and human blood. The low-cost, sensitive, specific paper-based chemiresistive biosensors were also fully assembled to enable the user-friendly operations, which potentially meets the ASSURED criteria for diagnostic devices in resource-limited settings.

6.2 Suggestions for Future Work

While the paper-based microfluidic chemiresistive biosensors are promising for potential rapid diagnosis in resource-limited setting, there are many future efforts to improve the developed biosensors. One important improvement can be the higher complexity of the paper-based microfluidics that can reduce the manual addition of samples and buffers. Fluid pockets containing buffers may be integrated with the paper-based biosensors to eliminate the buffer addition steps. Also, portable devices for measuring the electrical responses and analyzing the digital data can be investigated and integrated to output a final read-out for the end-users. Moreover, more complicated valve and timed fluid delivery in paper-based microfluidics can increase the level of automation and further make the device effortless for the end-users. Another improvement can be the replacement of the SWCNTs used in this research with higher semiconducting properties, such as purified semiconducting SWCNTs. In addition, there is a variety of other paper and fibrous substrates readily available for future paper-based FET and chemiresistive biosensors. Various pore sizes or retention time of various fibrous materials would render the biosensors with more microfluidic manipulations. Lastly, large-scale fabrication process should be optimized and stabilize for less intra- and inter- batch variation and consistent device quality.